Calibration and Design of the E and B EXperiment (EBEX) Cryogenic Receiver

A THESIS
SUBMITTED TO THE FACULTY OF THE GRADUATE SCHOOL
OF THE UNIVERSITY OF MINNESOTA
BY

Kyle Thomas Zilic

IN PARTIAL FULFILLMENT OF THE REQUIREMENTS
FOR THE DEGREE OF
Doctor of Philosophy

Professor Shaul Hanany

August, 2014

Acknowledgements

I first want to express my thanks to my advisor and mentor in experimentation through the years, Shaul Hanany. All good experimental practices I have are from him and without him I would be a "nicer" person.

None of the work I've done, data I've analyzed, things I've designed, built, tested, broke, fixed, and experimentation I've done would have possible without the concerted effort of the University of Minnesota Observational Cosmology group. Without my fellow graduate students – Chaoyun Bao, Clay Hogan-Chin, Hannes Hubmayr, Jeff Klein, Michael Milligan, Dan Polsgrove, Kate Raach, and Ilan Sagiv, – our dutiful undergraduate students – Alex, Bob, Craig, Dave, Geach, Vanessa,– and our fearless post-doc leader, Asad Aboobaker, our experiment would have crumbled and my sanity surely with it.

I would also like to acknowledge the fine work from everyone else in the EBEX collaboration and I would especially mention the Herculean efforts from everyone in the Nevis 2008, Fort Sumner 2009, Palestine 2011, Palestine 2012, and Antarctica 2012 campaigns. Hopefully this is the Final Countdown...

Dedication

This is dedicated to the individuals that, without whom, I wouldn't be here:

To Bill Jameson, who first inspired my love of physics and taught me more than just science.

To my mother, whose constant encouragement and steadfast support never let me falter.

To my wife, Maretta, who endures my presence and suffers my absence with great grace and, for whom, I am guided everyday to be better than I am.

Abstract

I discuss the design, construction, and calibration of the E & B EXperiment (EBEX), a balloon-borne telescope designed to measure the B-mode polarization anisotropy of the cosmic microwave background (CMB). EBEX observes the sky with 8 arcmin resolution in three frequency bands centered on 150, 250, and 410 GHz, with over 1,500 detectors. Polarimetry is performed through use of a continuously rotating achromatic half-wave plate with fixed wire-grid polarizer. The experiment was designed to detect the gravitational-lensed B-mode signal and detect or set an upper limit for the inflationary B-mode signal. In this thesis, I describe the design and structure of various subsystems of the EBEX receiver and predict their experimental performance. Several calibrating instrumental response experiments are described and the results reported and compared to predictions. A brief review of the 2012-2013 long duration balloon (LDB) flight from McMurdo Station, Antarctica, is provided and a summary of the receiver performance during flight characterized.

Contents

List of Tables

List of Figures

Chapter 1

Cosmology and the Science of the Microwave Background

The cosmic microwave background (CMB) offers a rare glimpse into the early Universe and allows observations testing physics shortly after the Big Bang. With the discovery of the CMB by Penzias and Wilson [33] in 1964, the Big Bang theory of the origin of the universe gained major acceptance within the scientific community while experiments such as COBE [28], MAXIMA [38], WMAP [4], and Planck [35] allowed measurements of cosmological parameters to extraordinary precision.

The field of cosmology has limited sources of experimentation and observation due to the existence of only one observable universe as well as the contamination of cosmology signals by local foreground sources and signal processing. This causes most cosmology signals to be difficult to observe and obtain useful information from. While not free from cosmologically local phenomena and foregrounds, the CMB offers such as wealth of information due to the source of the radiation, the epoch of its creation, and breadth of the parameters coupled to the signal that makes it such a important observation and truly unique within the field of cosmology.

1.1   CMB Genesis

Three minutes after the Big Bang, the universe consisted of a fluid of baryons, electrons, and photons held in thermal equilibrium by the processes of Thomson scattering and
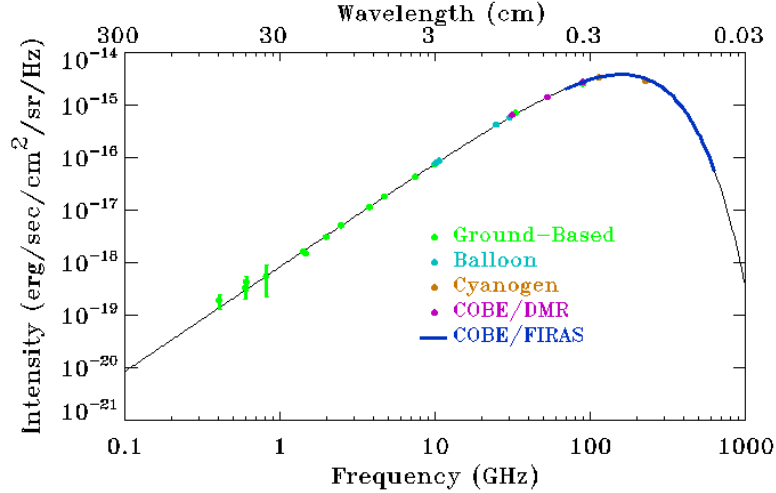
Figure 1.1: CMB intensity versus frequency spectrum from FIRAS[14].

Coulomb interaction. These thermal photons filled the volume of the universe and were in complete equilibrium and, as such, produced a blackbody radiation distribution with a characteristic temperature defined by the Planck function,

$$I\left(\nu, T\right) = \frac{2h\nu^3}{c^2} \frac{1}{e^{\frac{h\nu}{kT}} - 1} \tag{1.1}$$

Due to the expansion of the universe, the wavelengths of the photons that filled the universe stretched and the characteristic temperature of the radiation decreased with the redshift, z. About 300,000 years after the Big Bang, there were not enough photons at sufficient energy to keep the baryons and electrons ionized and neutral hydrogen was formed, this event is referred to as recombination. With no charged particles to Thomson scatter off of, the photons no longer interacted with matter and the universe was transparent to the blackbody radiation, which then traveled in a straight path until we observe it today, 13.8 Gyr after the Big Bang.

The blackbody radiation can now be measured at a temperature of 2.7 K, with a blackbody peak within the microwave regime. One of the most remarkable aspects of the CMB is its extreme homogeneity over the observable sky, with non-relative motion

anisotropies only observed at the 10^{-5} level or lower.

1.2   CMB Anisotropies

Although the CMB is uniform to 10^{-5}, the anisotropies in the CMB encode an incredible amount of information since the source of the anisotropies is coupled to various key parameters of the early universe. To quantify the distribution of the temperature fluctuations across the sky, the fluctuations are decomposed into spherical harmonics,

$$\Theta_{\ell m} = \int d\hat{n} Y_{\ell m}^{\star}(\hat{n})\Theta(\hat{n}) \tag{1.2}$$

where $\Theta(\hat{n})$ is the measured temperature fluctuations as a function of direction on the sky. The power spectrum is then characterized by C_{ℓ},

$$\langle \Theta_{\ell m}^{\star}\Theta_{\ell'm'} \rangle = \delta_{\ell\ell'}\delta_{mm'}C_{\ell} \tag{1.3}$$

and is typically reported as,

$$\Delta_T \equiv \sqrt{\frac{\ell(\ell+1)}{2\pi}C_{\ell}} \tag{1.4}$$

in units of μK. At large ℓ (small θ), ℓ can be considered to follow the relation $\ell \sim \frac{1}{\theta}$. When a fit to the power spectrum is then applied to data, cosmological parameters can be estimated to good precision.

1.3   CMB Polarization

The polarization anisotropies of the CMB, while more difficult to detect, offer a complimentary data set to the temperature anisotropies. The ability to measure the polarization signal from the CMB gives us the ability to break some observational degeneracies in the temperature spectrum, as well as probing the physics of the anisotropies and the sources of them more directly. One of the most interesting aspects of the CMB polarization anisotropy signal is the ability to measure a by-product of an inflationary epoch in the early universe and thus give supporting evidence for this theory.

The polarization of light from the CMB is generated by the Thomson scattering of a quadrupolar pattern of hot and cold photons off of electrons toward the observer. This produces a net linear polarization in the CMB that is produced by two perturbation sources. The net linear polarization can be quantified by the Stokes vector,

$$\boldsymbol{S} = \begin{pmatrix} I \\ Q \\ U \\ V \end{pmatrix} \tag{1.5}$$

with intensity I and circular polarization V, which will be ignored.

We will define $Q > 0$ as the up/down polarization state, $Q < 0$ as the left/right polarization state, and $\pm U$ as a 45° rotation of the $\pm Q$ states.

1.3.1 Scalar Perturbations

The temperature fluctuations described in Section 1.2 were perturbations generated by density fluctuation and are scalar perturbations. These density fluctuations produce gradients in electron velocities towards over-dense regions, which in turn produce a quadrupolar temperature field as viewed from an electron frame of reference. If a scalar perturbation is decomposed into plane waves, the net linear polarization produced from these quadrupolar temperature fields is either parallel or perpendicular to $\vec{k}$ of the plane wave, independent of the projection of $\vec{k}$ due to viewing angle.

1.3.2 Tensor Perturbations

Tensor fluctuations are transverse-traceless perturbations to the space-time metric, examples of which are gravitational waves. The orthogonal stretch and contraction produced by tensor fluctuations also generate a quadrupolar temperature field and a net linear polarization from Thomson scattering. Tensor fluctuations can be decomposed into plane waves with two states, $h_+, h_\times$, and the polarization direction generated by each is orthogonal to $\vec{k}$, however, viewing angle can produce polarization direction that is neither parallel nor perpendicular to $\vec{k}$ due to projection. The h_+ state projected along a horizontal axis will produce only Q polarization and the $h_\times$ will produce only U polarization, but projection of either along two axes will mix $h_+ \leftrightarrow h_\times$ and produce both Q and U states.

1.3.3 Polarization patterns

The Q-field and U-field polarizations discussed above work well to describe a single plane wave mode, however, with a superposition of multiple modes that would describe the real polarization in the sky, a more global characterization must be discussed. The commonly accepted way of describing the polarization pattern is with the scalar fields *E-mode* and *B-mode*.

An E-mode has a global property of having (-1^{ℓ}) parity under a $\hat{n} \rightarrow -\hat{n}$ transformation, while a B-mode has a $(-1^{\ell+1})$ parity under the same transformation. Locally, an E-mode has a vanishing spin-2 curl component and a B-mode has a vanishing spin-2 divergence component, and get their names as an analog to the electric and magnetic fields. Scalar perturbations produce a pure E-mode pattern, while tensor perturbations produces a mix of E-mode and B-mode patterns. With this global characterization, E and B-modes on different scales can then be quantified in a similar way to temperature perturbations and a power spectrum can be produced.

The importance of a B-mode signal in the CMB would be to prove the existence of gravitational waves within the early universe, a proposed effect of an inflation period after the Big Bang. Since the energy of the gravitational waves is embedded within the B-mode signal and is coupled to the energy scale of inflation, one finds that,

$$V_{\star}^{1/4}/m_{Pl} = 1.2 \left\langle (C_2^T)^2 \right\rangle^{1/4} = 3.0 \times 10^{-3} r^{1/4} \tag{1.6}$$

where $V_{\star}$ is the energy scale of inflation, m_{Pl} is the Planck mass, C_2^T is the quadrupolar amplitude of the tensor perturbation, and r is the ratio of tensor to scalar quadrupolar amplitude, from [24]. Thus, a measurement of the tensor perturbation from a B-mode signal would both give evidence of an inflationary period and provide the characteristic energy of the event.

An alternate source of an observed B-mode signal could also be the distortion of a strictly E-mode pattern by the CMB photons passing by matter densities and being gravitationally lensed. This contaminant, called the lensing B-mode or scalar B-mode since it is produced by scalar perturbations, is proposed to exist regardless of the existence of a tensor perturbation B-mode signal. The scalar B-mode signal was first detected by SPTPol [17] and further confirmation is pending.

The recent published detection of tensor B-modes from BICEP2[1] with $r = 0.20^{+0.07}_{-0.05}$ is a potential breakthrough in the study of inflationary cosmology, however, further detections are required to confirm the results and refine the measured B-mode amplitude.

Chapter 2

The E and B EXperiment

The E and B EXperiment (EBEX) is a balloon-borne CMB polarization anisotropy experiment with an engineering flight in New Mexico in June 2009 and a long duration science flight from Antarctica in December 2012 to January 2013. EBEX operates with three frequency bands (150, 250, and 410 GHz) in order to measure the CMB polarization signal as well as foreground signals, such as dust emission, that must be characterized and removed from the CMB. The EBEX telescope has 8 arcmin resolution and the planned observation region is a 350 deg^2 low-dust region, in particulr, looking in the multipole region of $20 < \ell < 1500$ with 1564 polarimetric detectors.

2.1   EBEX Science

The scientific goals of the EBEX experiment are five-fold:

1. To detect the tensor B-mode signal from an inflationary gravity wave background, or to set an upper bound that is a factor of 4 more restrictive than bounds prior to BICEP2 [1] and that would rule out an important class of inflationary models

2. To provide critical information about the polarization of Galactic foregrounds, particularly of dust emission, at a level of 0.1 μK

3. To confirm the signature of lensing of the polarization of the CMB measured by SPTPol [17], and demonstrate our ability to effectively separate it from the B-mode inflationary signature

4. To measure the E-mode CMB polarization signature to the cosmic variance limit
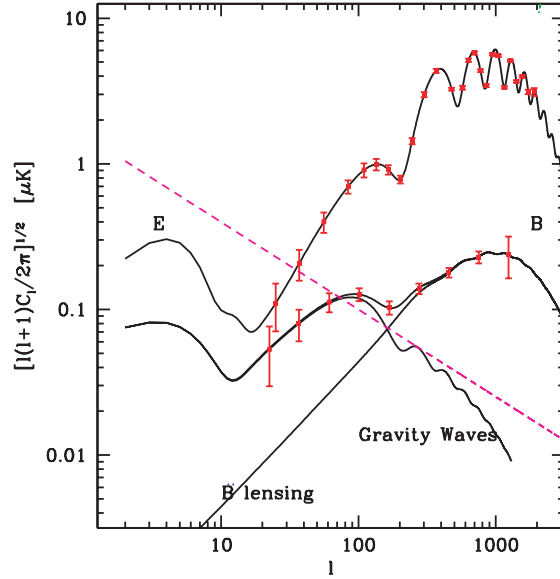
Figure 2.1: The expected 1σ determination of the E and B CMB polarization power spectra with EBEX after a long duration balloon flight (red points and error bars). The solid lines are theoretical models for E and B power spectra in a standard cosmology with $r = 0.05$. The B-mode spectra due to inflationary gravitational waves and due to lensing are shown both separately and combined. Galactic dust emission is also shown for the 150 GHz band and are based on results from WMAP [16].

up to $\ell = 1500$

5. To provide an important milestone in the implementation and testing of detector, detector readout, optics, and of techniques that are being considered for a future NASA CMB polarization satellite[5].

Figure 2.1 shows expected EBEX results after a long duration balloon flight with estimated error bars as well as showing the scalar B-mode contribution from gravitational lensing. The scalar B-mode would dominate the tensor B-mode signal for $\ell > 150$ assuming $r = 0.05$, but quickly become subdominant for $\ell < 100$, yielding a strong detection of the tensor B-mode signal.

Also shown in Figure 2.1 is the predicted foreground signal from dust emission as extrapolated from WMAP data. The dust signal will have to be well characterized at the higher frequency bands to measure a tensor B-mode signal for $r < 0.1$. Although observed by WMAP, there does not exist data to the precision required in the EBEX

(a) Payload model with outer frame.   (b) Rear view of outer frame.
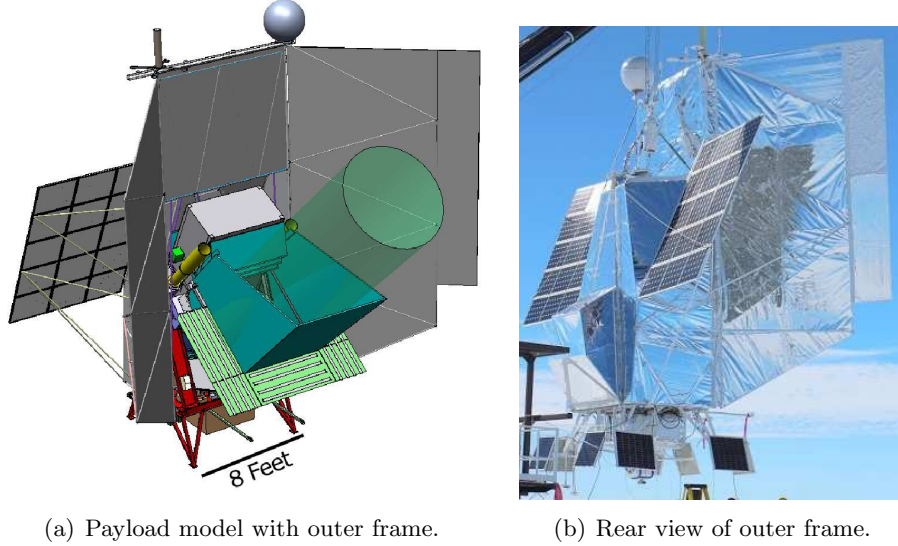
Figure 2.2: Model and picture of the EBEX outer frame. The base table (red), solar panels (black grid with gray), and baffling (gray) are shown in the model.

region of the sky, and very little data in the EBEX frequency range, so EBEX will produce new and valuable data on foreground emission necessary for further CMB study.

Additionally, a more precise measurement of the CMB E-mode signal will improve the accuracy of cosmological parameters such as the dark energy density, Ω_Λ, the total matter density, $\Omega_m h^2$, the baryonic matter density, $\Omega_b h^2$, the Hubble constant, and the the slope of the initial density perturbation spectrum compared to current values.

2.2   EBEX Payload

In order to attain the sensitivity required to measure the tensor B-mode signal to the level described above, the EBEX experiment utilizes a combination of traditional mm-wave balloon-borne technology as well as some technology new to the field.

The EBEX payload can be divided into two super-structures: the outer frame and the inner frame.

The central component of the outer frame is the payload base table, which houses the attitude control system (ACS) electronics, flight computers and data storage, reaction

(a) Inner frame model.

(b) Picture of the base table and inner frame structure.
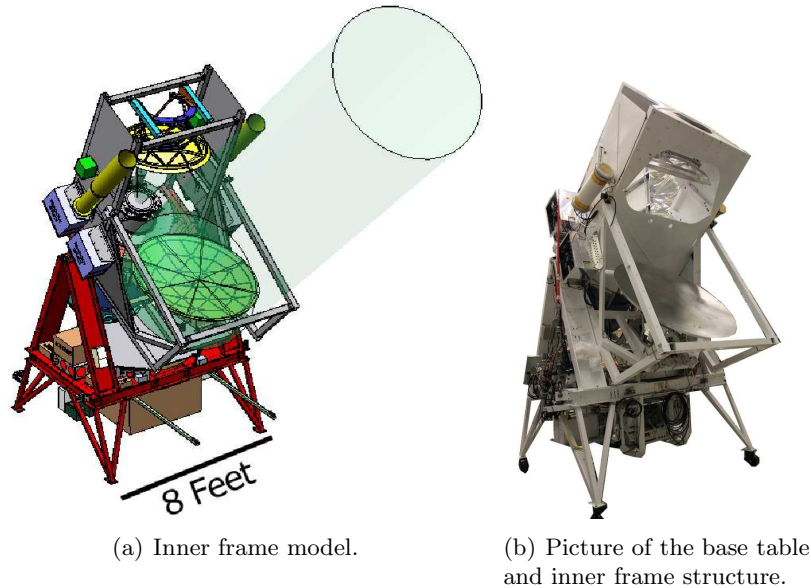
Figure 2.3: Model and picture of the EBEX inner frame. The base table (red), mirrors (yellow), and receiver (blue, mostly hidden) are shown.

wheel and batteries. The base table also has trunnion legs that support the inner frame, and the scientific instrumentation package (SIP) NASA flight electronics. The flight balloon is also tethered to the base table through the pivot motor and support cabling system. The combination of pivot motor operation and reaction wheel rotation gives controlled rotation of the outer frame in an azimuthal direction.

The outer frame also supports the satellite communication devices and baffling framework that shields the telescope from solar radiation during flight. To power the experiment, which uses less than 2 kW, the outer frame is the mounting point for the solar panel arrays used for in-flight power generation.

The inner frame is composed of the two telescope mirrors, cryogenic receiver with detector instrumentation, detector readout electronics, and several pointing-measuring devices. The inner frame is mounted from the trunnion legs of the outer frame, allowing rotational motion about the horizontal axis between the legs. This motion is controlled by a linear actuator that allows scanning of the inner frame in elevation angle.

The receiver contains optics that channel light to two focal planes where the detectors reside and data collected. The structure and operation of the receiver are discussed in

Chapters 3 and 4.

2.3   EBEX Pointing

The azimuthal and elevation angles of the telescope pointing are controlled by the pivot motor, reaction wheel, and elevation linear actuator and are readout and commanded through the ACS.

The ACS also reads out sensors used for pointing reconstruction. Two star cameras on the inner frame reconstruct pointing from comparing star-field images to known star catalog positions with an accuracy of <1 armin. Three orthogonally mounted gyroscopes are also used to determine position through integration of rotational rates measured with the devices. In addition, differential GPS receivers, a sun-position sensor, and magnetometers measuring the Earth's field are used to further refine pointing accuracy and have system redundancy.

Chapter 3

The EBEX Receiver: Structure

The EBEX receiver was designed in 2006 primarily by collaborators at Brown University and the University of Minnesota: Twin Cities, with the main design principle of increasing detector sensitivity with a minimum of weight. This was accomplished through three major design aspects: to allow for a large diameter, cold optics system to increase signal throughtput; a 2-3 week holdtime for liquid cryogens to maximize observation time for the cold, bolometric detector arrays; and an RF-clean environment for signal wiring to minimize excess noise. The receiver also was designed to house the achromatic half-wave plate (AHWP) and AHWP rotation mechanism utilized to make each bolometric detector an independent polarimeter, and readout system cold amplifiers. The receiver housing was constructed by Precision Cryogenics, Inc. and is primarily composed of aluminum 6061-T6 and G-10 fiberglass for mechanical support and thermal isolation.

The receiver system is divided into several sub-systems for development and testing purposes and were designed around the three aspects described above. The sub-systems are as follows: Thermal Shells, Double Window Mechanism, Optics Stack, AHWP, Optics Box, Focal Planes, Helium Refrigerators, and RF Towers.

3.1   Thermal Shells

The receiver is a vacuum-cavity cryogenic vessel with five thermal layers to optimize loads on liquid cryogens and achieve required temperatures for the detector, readout,

(a) EBEX receiver and instrument model cut-away.

(b) EBEX receiver shells model.
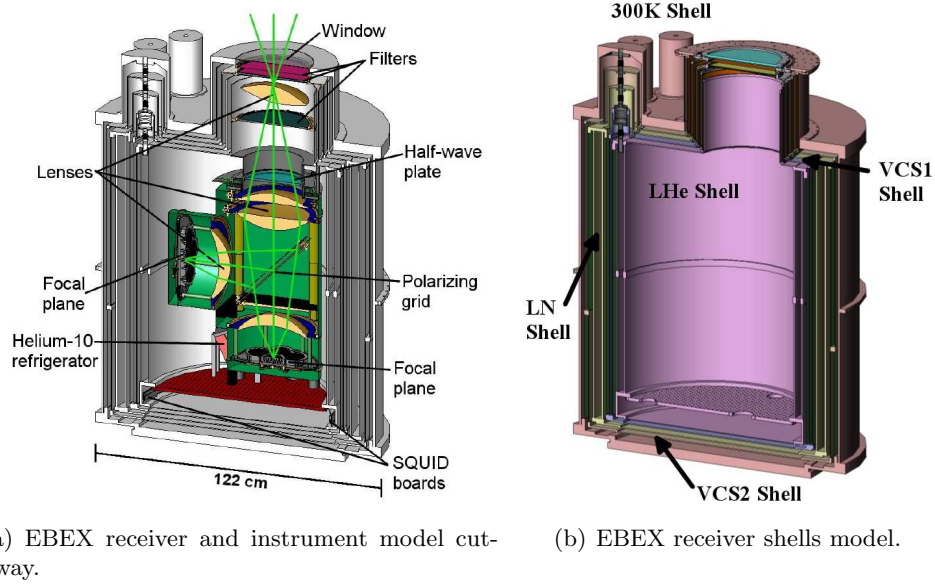
Figure 3.1: Diagram of the EBEX receiver internal structure.

and AHWP systems. The structure of these layers are described in Figure 3.1(b). The outermost thermal layer is called the 300K shell and provides the mechanical connection to other components of the experiment as well as being the vacuum shell for the receiver. It is primarily composed of a 7.9 mm thick, 1166 mm diameter, 1260 mm tall welded Al cylinder, a 38.1 mm thick light-weighted circular top plate, a 25.4 mm thick bottom ring, a 3 mm thick domed bottom lid, and a 273 mm tall cylindrical protrusion from the top plate called the optics stack. The 300K shell also encompasses the window and double window assemblies, AHWP rotation motor, and readout and housekeeping wiring vacuum feedthroughs. During laboratory operation, the 300K shell is at room-temperature, however, during flight operations, the reduced atmospheric temperature also potentially reduces the 300K shell temperature, see Section 4.1.

A 1 mm thick, 438 mm tall, 1120 mm diameter G-10 fiberglass cylinder connects from the bottom interior of the 300K shell to the middle of the next layer, called vapor-cooled shield 2 (VCS2). Structurally, the VCS2 shell is approximately a 1225 mm tall, 1.5 mm wall thickness, 1125 mm diameter cylinder with 3.2 mm thick top and 6.4 mm thick bottom circular plates, with a similar optics stack that is nested within the 300K shell optics stack. This layer is kept at a temperature of approximately 210 K by the cold

vapor that is evaporated from the liquid nitrogen layer using a copper heat exchanger in the boiloff path. The VCS2 shell is used for mechanical separation of other thermal layers and as a thermal intercept of components that extend from cooler layers to the 300K shell.

Another G-10 cylinder of 735 mm height, 1 mm thickness, and 1088 mm diameter then connects from the middle interior of the VCS2 shell to the top of the next layer, the LN shell. The LN shell is held at 77 K by a tank of liquid nitrogen (LN) and is approximately a 1186 mm tall, 1045 mm outer diameter, 953 mm inner diameter hollow toroid with a 3.2 mm thick top and 6.4 mm thick bottom circular plates. The LN shell can hold up to 130 L of LN and can be filled from ports that connect to the non-vacuum side of the 300K shell top plate. The tank cavity is connected only to the exterior environment through these ports and is isolated from the rest of the vacuum cavity of the receiver. During flight operations, the tank cavity is isolated from the exterior environment by absolute pressure valves to prevent excess boiling and cooling of the cryogens. The LN shell also acts as a 77 K thermal intercept and has an optics stack protrusion nested within the VCS2 optics stack that contains an array of thermal filters for reducing optical loading on cryogens, see Sections 3.3 and 4.4.

A 1137 mm tall, 1 mm thick, 926 mm diameter G-10 cylinder then connects from the top interior of the LN shell to the bottom of the next layer, vapor-cooled shield 1 (VCS1). The VCS1 shell is a 1153 mm tall, 1.5 mm wall thickness, 897 mm diameter cylinder with 3.2 mm thick top and 6.4 mm thick bottom circular plates, with an optical stack nested within the LN shell stack. VCS1 is kept at approximately 28 K by the cold vapor boiloff from the liquid helium layer with a similar heat exchanger as VCS2. VCS1 is the final thermal intercept before the LHe shell and separates the two liquid cryogen shells.

Between VCS1 and the innermost layer is the last G-10 cylinder, which is 1096 mm tall, 1 mm thick, and has a 870 mm diameter and extends from the bottom of VCS1 to the top of the LHe shell. The LHe shell is held at 4.2 K by a tank of liquid helium (LHe) and is approximately a 1000 mm tall, 831 mm outer diameter, 712 mm inner diameter hollow toroid with a 3.2 mm thick top and 1.6 mm thick bottom plates. The LHe tank can hold up to 130 L of LHe and has two fill ports on the exterior of the 300K shell top plate. The tank cavity is connected only to the exterior environment through these
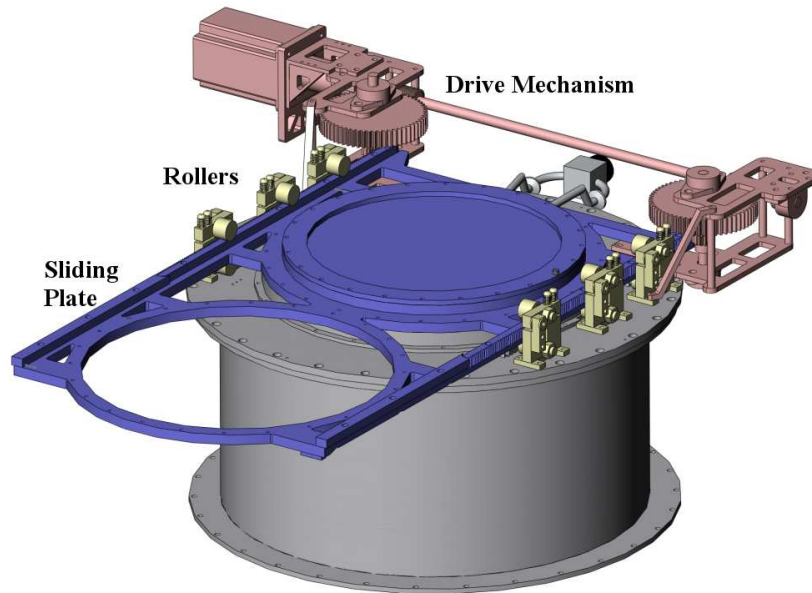
Figure 3.2: DWM design model with sliding plate (blue), drive mechanism (pink), and sliding plate rollers (yellow) highlighted.

ports and is isolated from the rest of the vacuum cavity of the receiver.

During ground testing, the amount of LHe in the tank is readout using a length of superconducting wire inserted into one of the fill ports of known normal resistance that is partially submerged in the LHe bath. The measured resistance of the wire encodes the superconducting length, and thus, the amount of LHe in the tank. During flight operations, this level sensor is removed and the tank cavity is isolated from the exterior environment by absolute pressure valves to prevent excess boiling and cooling of the cryogens. The LHe shell has an optics stack protrusion nested with the VCS1 stack that houses additional filters and the first cold optical element. The AHWP and rotation assembly are located at the top interior of the LHe shell and the bottom interior of the shell has a mounting point for an aluminum plate that the receiver instrumentation is mounted on and beneath which the detector readout cold amplifiers are mounted.

3.2 Double Window Mechanism

At the top of the 300K optics stack, an ultra-high molecular weight polyethylene (UHMWPE) disk acts as a mm-wave transparent window to separate the vacuum environment of the receiver interior from the external environment. The diameter of the window is set by the EBEX optical design, however, the thickness of the window is optimized for the two environments that the receiver experiences: the nominal lab testing environment and the flight data-taking environment. The need for the receiver window to operate in both these environments drove the design of a Double Window Mechanism (DWM).

3.2.1 Design

The design of the DWM is driven by three factors: the survivability of the window and elements underneath the window, the vacuum isolation of the receiver environment, and the mm-wave absorption and emission in the three EBEX frequency bands.

In the reverse light path view, with rays of light exiting the focal planes, progressing through the optical elements, and diverging as they head to the sky, the divergence of the rays exiting the last cold lens out of the receiver, the field lens, and the distance to the end of the optics stack sets the minimum diameter of the UHMWPE window. In order to minimize weight of the experiment, the distance from the field lens to the top of the optics stack is made sufficient to hold the various light filters with minimal margin to account for mechanical support and thermal contraction. This separation between the field lens and the top of the optic stack sets the minimum window diameter to accommodate the optical system to be 279 mm. A margin of 10 mm was added to the radius of the window, which is approximately 5 wavelengths at the smallest EBEX frequency band, to reduce diffraction effects in the optics. Several different materials were considered for the 300 mm open-aperture diameter window, including sapphire, Zotefoam, polypropylene, and UHMWPE. However due to fabrication limitations, potential vacuum-induced plastic expansion, and durability, UHMWPE was ultimately choosen. UHWMPE has the advantages of a CMB experiment history with the QUAD experiment[18], the ability to bond with certain epoxies such as Stycast 1266 and Epoxy 907 from Miller-Stephenson, availability of anti-reflective coating technology
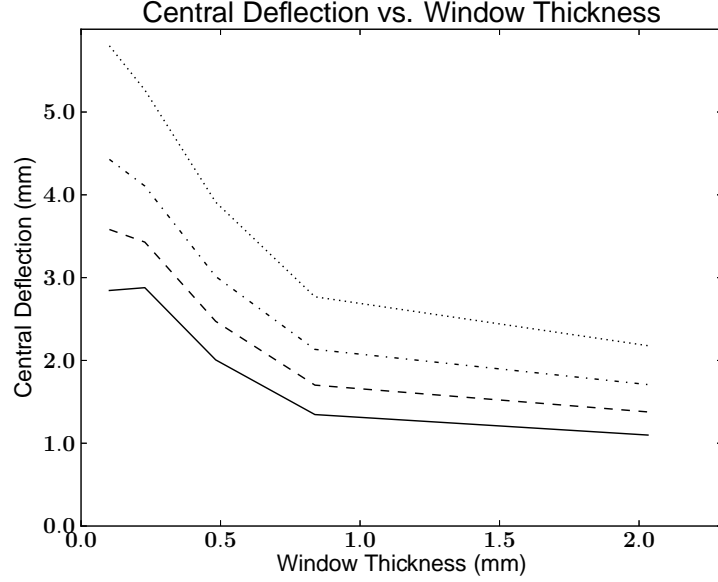
Figure 3.3: Central deflection versus thickness of window under 10 (dotted), 7 (dot-dash), 5 (dashed), and 4 torr (solid) pressure differential.

through collaborators at Cardiff University, and strong scratch and puncture resistance.

The relatively large diameter of the window presented a design problem as ground testing would produce a full atmosphere pressure differential across the window, causing a significant deflection in the material over a range of potential window thicknesses. Figure 3.3 shows measured central deflections of the EBEX window at various thicknesses. Deflections greater than 9.5 mm can potentially damage a thin polypropylene filter beneath the window as well as inducing a net linear polarization signal into the detectors due to the asymmetry of the optical system. This induced polarization signal is created prior to the AHWP and would be modulated similarly to signals from the sky and the strength of which would vary with light intensity incident on the window, however, the direction of polarization would be constant relative to the experimental coordinate system. A relatively thick window with thickness of 12.7 mm has a small enough deflection to ensure filter survival and minimal induced polarization signal but causes sky signal loss due to absorption. The absorption is approximately 0.6%, 1.3%, and 3.0% for 150, 250, and 410 GHz, respectively. This thick window also increases

detector loading from in-band emission from 4.29, 9.26, and 11.42 pW for no window to 5.31, 12.53, and 17.03 pW for 150, 250, and 410 GHz, respectively, in flight conditions. A thin window would be optimal for sky signal detection, with 0.05%, 0.1%, and 0.25% absorption and total detector loading of 4.37, 9.52, and 11.87 pW for 150, 250, and 410 GHz, respectively, but would suffer from large deflections and potential vacuum leakage or failure.

A hybrid solution was created to achieve minimal deflection and low signal absorption and detector loading. A 12.7 mm thick UHMWPE window (thick window) is placed above a 1.0 mm thick UHMWPE window (thin window) for ground operations, and is then moved out of the optical path for flight operations with the thin window remaining to ensure the receiver vacuum environment. An open aperture is left above the thin window when the thick window is removed. The predicted $\sim$10 torr pressure differential across this thin window during flight operations would produce a small deflection which is shown in Figure 3.3. The deflections in Figure 3.3 were measured by isolating the two vacuum cavities in a test setup without the rest of the receiver and, using a small hand-pump, reducing the pressure in the first cavity to produce the pressure differentials measured with a pressure gauge. The central deflection at the various pressure differentials was then measured with a caliper for several different thickness windows. This deflection is small enough to produce acceptable levels of induced polarization and does not damage the filter beneath the window. A mechanism was then designed to move the thick window out of the optical path, the DWM.

The DWM assembly was designed to interface to the existing optical stack top plate and was based on a double window mechanism flown by a previous balloon-borne experiment. The design was driven by four specifications: primary and secondary vacuum cavity integrity, reliable thick window movement and position encoding, low-mass, and flight-like environment survivability and operation.

The DWM utilizes two separate vacuum cavities to minimize deflection in the thin window during ground and flight conditions, these are shown in Figure 3.4. The primary vacuum cavity is the interior of the EBEX receiver which is under vacuum during all operations and exists beneath the thin window. Between the thin window and the thick window is the secondary vacuum cavity. This cavity must be under vacuum during ground operations to reduce thin window deflection, however, it will be exposed to the
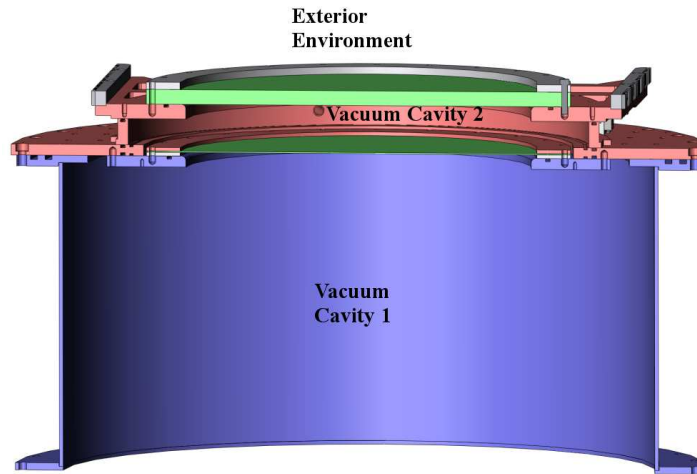
Figure 3.4: Dual vacuum cavity design of the DWM. The two cavities are connected with a valve (not shown) to equilibrate both cavities during initial evacuation. Thick and thin windows are shown in green.

local atmospheric environment during flight operations as the thick window is removed. The primary and secondary vacuum cavities are connected through a small inline valve that is open during ground operations and is closed prior to launch. This produces zero pressure differential across the thin window on the ground and approximately 10 torr differential in flight. Primary vacuum integrity is ensured by attaching the thin window to a flat aluminum ring with Epoxy 907 and then clamping the window and ring onto an o-ring on the mounting surface. This method of forming vacuum environments was flight tested in the MAXIMA and MAXIPOL experiments. The thick window is directly clamped onto an o-ring on its mounting surface for the secondary cavity.

Vacuum integrity of the primary and secondary cavities is also required for post-flight operations to avoid destruction of filters and sensitive electronics within the receiver during the termination of flight and the return of the experiment to surface atmospheric conditions. This necessitates that the movement mechanism for the thick window be able to re-establish vacuum integrity after removal of the thick window from the optical path. To achieve this, the thick window is mounted on an aluminum plate, the sliding plate, that is then clamped to an o-ring seal to form the secondary cavity between the windows. The sliding plate is able to move away from the optical path and return to
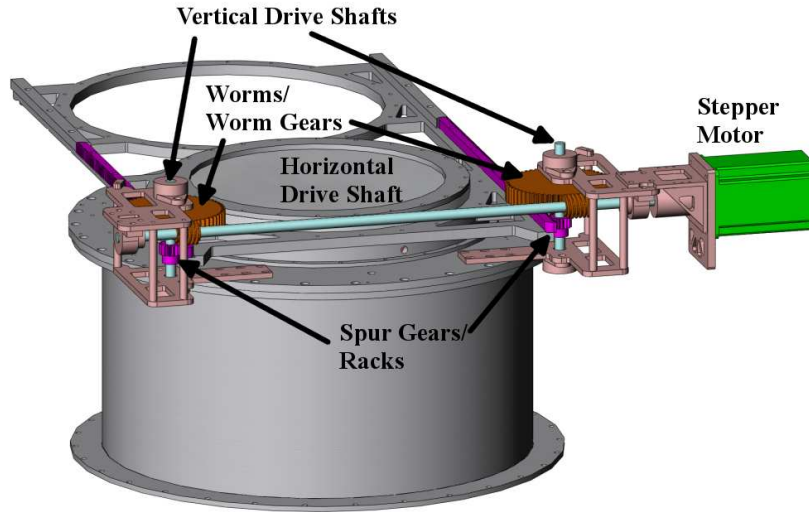
Figure 3.5: DWM drive mechanism model with stepper motor (green), drive shafts (blue), worm/worm gears (orange), and spur gear/racks (magenta).

this o-ring seal to reform the secondary cavity for the end of flight.

To form a proper o-ring seal for the secondary cavity, the sliding plate is shifted downward to compress the stationary o-ring by use of a series of grooves in the track the plate moves along. In order to assure that the o-ring remains stationary for all configurations of the thick window, even when it is moving, the o-ring is seated in a dovetail groove which sets the maximum compression of the o-ring to be 0.71 mm, or about 20% of the 3.53 mm diameter. Due to the movement of the sliding plate, a relative high hardness, A75, o-ring was chosen to resist abrasion and damage from rubbing. According to [32], this compression percentage and hardness requires a compressive force per length of the o-ring of 1.2 to 6.6 $\frac{N}{mm}$ for proper vacuum sealing. A value of 2.9 $\frac{N}{mm}$ was chosen to give a safety margin above the mimimum value, and with the 410 mm nominal diameter o-ring, gives a compressive force of 3700 N. In a ground configuration, a force of 13300 N is provided on this o-ring due to the pressure differential across the thick window, however, during flight conditions, atmospheric pressure provides only 180 N of force. To provide the required force during flight, 12 high-stiffness springs with spring constant 41.32 $\frac{N}{mm}$ are compressed 7.5 mm each, which then presses on the sliding plate and o-ring via rollers mounted above the sliding plate.

The sliding plate is guided in its movement by miniature track rollers both above and below the plate. The sliding plate is driven by a rack and spur gear system which is itself driven by a worm gear. A model of the DWM drive mechanism is shown in Figure 3.5. A gearing system is used due to its simplicity in design, compactness, and large output torque as well as having minimal low-temperature effects that would be experienced in flight-like conditions. The rack is oriented horizontally to eliminate rack/spur gear separation when the sliding plate is compressed downward onto the o-ring seal, and this forced two symmetric spur gear and worm/worm gear systems to be designed on either side of the sliding plate to ensure proper movement of the plate. It should be noted that one of the worm/worm gear systems is right-handed and the other is left-handed.

Both worms are driven the same horizontal drive shaft attached to a stepper motor due to the availability of stepper motor interface cards and software already used in EBEX and its high repeatability and reliability. The grooves in the sliding plate for compression of the o-ring are triangular and make an angle of $32.2°$ relative to the track face, which requires a force of 2300 N to move the rollers out of. Given the radius of the spur gears of 12.7 mm and the 60:1 worm/worm gear ratio, this requires a motor torque of 0.49 Nm. The stepper motor initially selected could output a maximum torque of about 1.5 Nm at low speeds, however, this was found to be marginal due to the power efficiency of the worm/worm gear system. Worm/worm gear efficiency depends on the coefficient of friction between the two surfaces as,

$$\text{Eff} = \frac{1 - \frac{p\mu}{2\pi r}}{1 + \frac{2\pi r\mu}{p}} \tag{3.1}$$

where $p = 2.12$ mm is the worm/worm gear pitch used and $r = 12.7$ mm is the worm effective radius. The kinetic coefficient of friction between the cast iron worm gear and steel worm is expected to be about 0.2 when unlubricated, which gives an efficiency of 12%. In order to decrease the friction between the components and protect the open gearing from oxidation, Dow Corning Molykote dry lubricant was applied which was expected to lower the coefficient of friction to between 0.02 and 0.06, and thus increasing the worm/worm gear efficiency to between 30% and 57% and the required motor torque to between 0.86 and 1.63 Nm. A stepper motor with maximum output torque of 3.88 Nm was chosen for the final design to give a roughly factor of two safety margin in the worst coefficient case.

The DWM is operated at low speeds, taking 3.3 minutes to move the 419 mm from the thick window to open aperture states. This is done to ensure reliability by operating the stepper motor in a high-torque regime; and since it is operated only two times during flight, it has a negligible effect on total observation time. To remotely monitor the position of the sliding plate along its travel, two limit switches are located at either end of the mechanism and are depressed when the sliding plate is in the thick window or open aperture positions. The state of these switches are continuously readout as analog voltages. For further discussion of non-detector electronics readout, see [41].

Light-weighted aluminum components were used extensively to minimize mass, as well as modification of all steel componenote to decrease mass. In total, the DWM has a weight of 48 lbs, including the windows, vacuum valve and bellows, and stepper motor. Military specification Buna-N o-rings rated to $-54°C$ were used for its thermal properties and abrasion durability.

3.2.2 Testing

After the design and initial assembly of the DWM, testing was performed to optimize the travel of the sliding plate and minimize the torque required for operation. This was performed with the assistance of an undergraduate researcher. The DWM was cycled between thick window and open aperture positions 10 times and the reformed vacuum sealed was checked for vacuum integrity. This test was performed multiple times to ensure the reliability of the travel of the sliding plate and return to resealing position. To test the DWM in flight-like conditions, the mechanism was tested twice in the Bemco environmental chamber at the Columbia Scientific Balloon Facilty in Palestine, TX in July 2011 and September 2012. The DWM was assembled with an absolute pressure gauge attached to the secondary vacuum cavity to monitor the integrity of the reseal, temperature monitors on several keys components of the DWM including the stepper motor, sliding plate, optical stack top plate, and general chamber temperature, and the position switches were readout. Chamber pressure was also readout throughout.

The DWM primary and secondary vacuum cavities were initially evacuated outside the chamber and the primary cavity was then isolated from the external environment and secondary cavity with valves. The DWM in this pre-flight-like state was placed in the chamber which was then evacuated of air. The chamber was then backfilled with dry
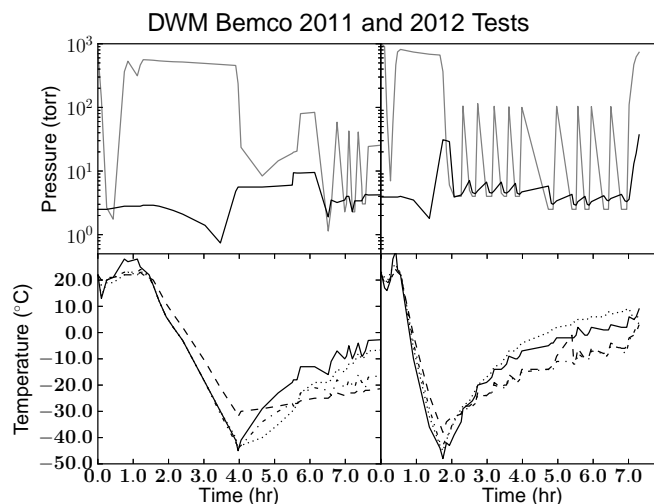
Figure 3.6: Pressure (top) and temperature (bottom) profiles for the DWM Bemco chamber testing in 2011 (left) and 2012 (right). Chamber (gray) and DWM cavity (black) pressures, and chamber (solid), top plate (dashed), sliding plate (dash-dot), and stepper motor controller (dotted) temperatures are shown. DWM cavity pressure rises below -40° C due to pressure gauge leakage.

N_2 gas to allow temperature manipulation of the chamber through convective means and cooled by pumping LN through the walls of the chamber. This cooled the chamber and DWM down to -45 and $-48°$C for the two tests, similar to temperatures that would be experienced during the initial accent of the EBEX payload through the tropopause. A rise in secondary cavity pressure was observed at these low temperature for both tests, and are attributed to operation of the Agilent ConvecTorr Pressure Gauge well below design specifications giving skewed pressure readings and possible internal leaks. Both affects stabilized above $-45°$C and increasing pressure of the secondary cavity was no longer observed.

The cavity and DWM were then allowed to warm up and the following cycle was tested 6 and 10 times for the two testing times, respectively: pump the chamber down to between 2 and 10 torr of pressure, move the sliding plate to the open aperture position, move the sliding plate to the thick window position, and backfill the chamber to ~ 100 torr with N_2 gas. The pressure and temperature data for the two testing periods are shown in Figure 3.6. The data shows that the secondary cavity pressure remains

relatively constant during the backfilling and pumping process, and the small increase in pressure observed for some of these cycles can be attributed to the temperature dependence of the pressure readout in the Agilent gauge. The position encoding using the limit switches was also successfully demonstrated during the first testing period, though a wiring fault during the second testing period eliminated limit switch readout.

This testing showed the reliability of the DWM assembly, including the drive mechanism, resealing scheme, temperature tolerance with the exception of the non-flight pressure gauge, and sliding plate position readout.

3.3   The Optics Stack

The optics stack is the cylindrical protrusion from the top of the EBEX receiver that acts as the mounting base for the DWM, houses the first cold lens, the field lens, and most of the thermal and optical filters for reducing loading on the various cryogenic stages. The stack was designed as a protrusion to account for the length of the EBEX optical system without having to make the receiver vessel larger and thus add weight to the payload.

The optics stack consists of open-topped cylindrical shells, called stacks, nested within each other with the bottoms of each shell connected to one of the thermal stages within the receiver. Each stack has several layers of multi-layer insulation, alternating layers of aluminized-mylar and plastic netting acting as thermal and electrical isolation, that reduce the effective emissivity of the surfaces of the shells exposed to a higher temperature stage. This reduces the absorption on the shell and thus the overall temperature of the thermal stage as a whole, see Section 4.1.4.

The dimensions of the optics stack were set by first fixing the optical system position within the receiver which fixes the field lens position within the optics stack, and then accounting for the quantity of required filters for reducing loading on the thermal stages of the receiver. In principle, the optics stack could have been extended and made taller, however, this would have required the window diameter to expand as the optical design diverges above the field lens. This expansion was limited by the size of window that could be placed in the Cardiff University oven used for applying the anti-reflection coating. A taller optics stack would also add weight to the experiment, and so a minimal optics

stack was preferred in the design. The minimal diameter of the optics stack was set by the diameter of the field lens within along with the various other stacks that must also be nested within the vacuum shell layer.

It should be noted that the optics stack is not coaxial with the overal receiver cyclindrical body due to the asymmetry of the optical system produced by the second focal plane. The heights of the stacks are 273, 300, 298, 302, and 293 mm and the diameters are 514, 457, 415, 375, and 336 for the 300K, VCS2, LN, VCS1, and LHe stacks and the axial offset between the receiver and optics stack is 146 mm.

3.3.1   Thermal Contraction

A major concern in the design of the optics stack was the potential for thermal shorting between the various temperature stages due to thermal contraction of the aluminum and G-10 that comprise the thermal shells. To account for this, a comprehensive analysis of the thermal contraction of each stage was performed. Data for the linear thermal expansion of the G-10 and the aluminum alloy used is taken from NIST Cryogenics Technologies Group [39]. The analysis consisted of three parts: calculating the vertical, along the axis of the cylindrical receiver, contraction of the aluminum, calculating the radial contraction of the aluminum, and calculating the vertical contraction of the G-10.

The first two aspect are relatively simple by measuring the temperatures each thermal stages reaches and using the data from [39]. The temperature and contraction amounts are shown in Table 3.1. Clearances between the separate stacks radially can also be calculated by using that same contraction data and the radii mentioned above. Due to the offset between the receiver and optics stack axis, the contraction between the side of the stacks nearest to the receiver axis, the 'near' side, differs from the side furthest from this axis, the 'far' side. This data is shown in shown in Table 3.2.

To calculate the contraction of the G-10, the largest unknown is the distribution of the temperature gradient along the G-10 cylinder that spans the different temperature stages. An average thermal contraction value over the temperature range between the stages on either end of the G-10 would be appropriate for a uniform temperature distribution along the length of the cylinder. To model the temperature distribution along the G-10 segments, it was first assumed that radiation would not provide a significant transfer of energy away from the G-10. While this assumption is weaker at higher

temperatures, two factors led to this assumption: higher temperatures would have correspondingly smaller thermal contractions and would not significantly impact the final contraction values, and the low emissivity environment inside the receiver would contribute to the immediate emission and absorption of radiation from the G-10 back onto the local G-10 resulting in very little heat transfer. With this assumption, the major avenue for heat transfer is heat conduction, described for a uniform geometry by,

$$P = \frac{A}{l} \int_{T_{\text{low}}}^{T_{\text{high}}} k(T)\,\mathrm{d}T \tag{3.2}$$

for a temperature gradient across material of cross-sectional area, A, length, l, and thermal conductivity, k, with ends at T_{low} and T_{high}. The total power conducted over the entire G-10 segment is the same as the power through any portion of the same segment if there is no other avenue for heat transfer, therefore,

$$\frac{l_{T_1 \to T_2}}{l_{T_{\text{low}} \to T_{\text{high}}}} \approx \frac{\int_{T_1}^{T_2} k(T)\,\mathrm{d}T}{\int_{T_{\text{low}}}^{T_{\text{high}}} k(T)\,\mathrm{d}T} \tag{3.3}$$

assuming there is only a small change in the cross-sectional area over the temperature ranges compared to any changes in the thermal conduction value. Thus the fractional size of the integrated thermal conduction over a small temperature range compared to the entire temperature range describes the fractional length of that smaller temperature range.

Stage	Temperature (K)	Al Contraction
300K	300	0.000%
VCS2	210	0.127%
LN	77	0.389%
VCS1	30	0.415%
LHe	4.2	0.415%

Table 3.1: EBEX receiver stage labels, operating temperatures, and aluminum thermal contractions.

With the temperature distribution along the G-10 segments now modeled, the thermal contraction can now be calculated for the G-10 isolation and then absolute movement of the receiver components as well. The absolute contraction amounts at the tops of the optics stack shells relative to the static 300K shell are shown in Table 3.2. Due to the fact that the G-10 cylinder isolating VCS1 from the LN stage is supported from the top of the receiver, the tops of the VCS1 and LHe stages get closer vertically due to the thermal contraction. The diminishing radii of the stacks also cause the separation of VCS1 and LHe stacks to shrink.

Stage	Vertical Contraction	Radial 'Near'	Radial 'Far'
300K	0.000	0.000	0.000
VCS2	1.511	0.127	0.499
LN	2.403	0.308	1.444
VCS1	4.435	0.243	1.454
LHe	2.380	0.158	1.367

Table 3.2: EBEX receiver stage vertical and radial thermal contractions at the tops of the optics stack shells. Contraction values shown are absolute movement of the component relative to the static 300K shell and are in millimeters.

These contraction values contributed to the filter design by limiting the number of components that could be placed in the optics stack before thermal shorting of elements would be expected. The values also contributed to the alignment scheme for the EBEX optical system described in 4.3 and the design of the radio-frequency (RF) shielding that occurs in the optics stack.

The optics stack contains the first scheme to separate the receiver vacuum cavities into two separate noise environments to minimize detector noise, see Section 4.2.1. This is achieved by using layers of 25 micron thick, stainless steel foil in a cylindrical shape. Stainless steel was chosen for it availability at small thicknesses, relative durability, and low electrical conductivity. Due to the thermal contraction of the stages that the stainless steel foil is attached to, robustness of the foil was deemed critical in its design to withstand any excess stress from the contraction. Additional length was

added to the lengths of the foil where necessary to avoid mechanical failure during thermal contraction, however, excess length was avoided to minimize the chance of the foil bowing and touching either thermal stage it spans between. The dimension of the stainless steel foil cylinders used for RF shielding are shown in Table 3.3.

Stage	Height	Radius
VCS2	308.6	244.3
LN	305.6	219.7
VCS1	308.1	199.1
LHe	301.5	179.2

Table 3.3: RF shielding stainless steel dimensions. The values are for the foil between the next warmer thermal stage and the stage listed and are in millimeters.

3.3.2 Filters

The optics stack contains the various filters in the EBEX receiver to reduce the loading on the cryogenic stages thermal radiation, mainly from frequencies above 1 THz. This radiation originates from the vacuum shell of the receiver itself, the rest of the EBEX payload operating at ambient temperature, the atmospheric emission, and from any object or source in the beam of the optical system. The effects of this radiation on the cryogenic performance of the receiver is discussed in Section 4.1.4. The effects of these filters on the EBEX receiver spectral response are discussed in Section 4.4.

The filters are divided into two categories: thermal and low-pass edge filters. The thermal filters are 10 micron thick polypropylene with a copper layer with geometry designed to reflect frequencies above a certain cutoff-frequency. These cutoff frequencies vary from 6 to 15 THz, primarily used to reject thermal radiation from warm objects. The low-pass edge (LPE) filters consist of multiple layers of copper on polypropylene with an anti-reflective porous-Teflon layer and are designed to reflect lower frequency radiation than the thermal filters. The LPE filters start defining the EBEX frequency bands and continue to reject more thermal radiation. The cutoff-frequencies of the LPE filters vary from 540 GHz to 750 GHz and are mounted at the LN and LHe thermal

stages. Multiple filters are necessary due to non-zero emissivity of these filters which causes them to absorb some amount of the incident radiation and warm which they then re-emit to the colder thermal stages. A 12.7 mm thick Teflon absorptive filter is also placed in the optics stack at the LN stage to absorb some of the thermal radiation and then conduct this power to the LN bath to reduce loading on the LHe stage.

During laboratory testing of the receiver, in order for nominal EBEX detectors to operate on the superconductive transistion edge, a neutral density filter (NDF) is placed in the optics stack immediately beneath the field lens. The NDF functions as an absorptive filter with specifically chosen thicknesses to absorb approximately 98% of incident power on the NDF in each of the three EBEX frequency bands. The NDF is a circular plate made of Eccosorb MF110 [11], that is divided into seven segments, a central segment and six radial segments, with varying thickness. Due to the placement of the NDF beneath the field stop of the optical system, these seven segments correspond to the seven wafer positions on the two focal planes. Further discussion of the effect of the NDF on the frequency response is in Section 4.4.

The NDF is mounted on the LHe stage of the receiver and operates at about 9 K during laboratory testing. This is higher than the bath temperature of 4.2 K due to the power absorbed in the material and thermal resistance between the mounting and the LHe tank. Even at this temperature, the NDF reduces the atmospheric load in the EBEX bands sufficiently to keep the detectors from saturating and losing responsivity, see Section 3.6. A diagram of the elements in the optics stack, and in the light path, is shown in Figure 3.7.

3.4   Half-Wave Plate

A half-wave plate (HWP) is an optical element that rotates the polarization angle of input linear polarized light about a certain crystal axis within the half-wave plate. The HWP is made of a birefringent material, sapphire in the case of EBEX, that has two distinct indeces of refraction in orthogonal directions, called the ordinary and extraordinary axes. The decomposition of the light along these axes into an ordinary wave and extraordinary shows that, due to the difference in indeces of refraction, the two waves experience a relative phase shift, called retardance, when passing through the material.
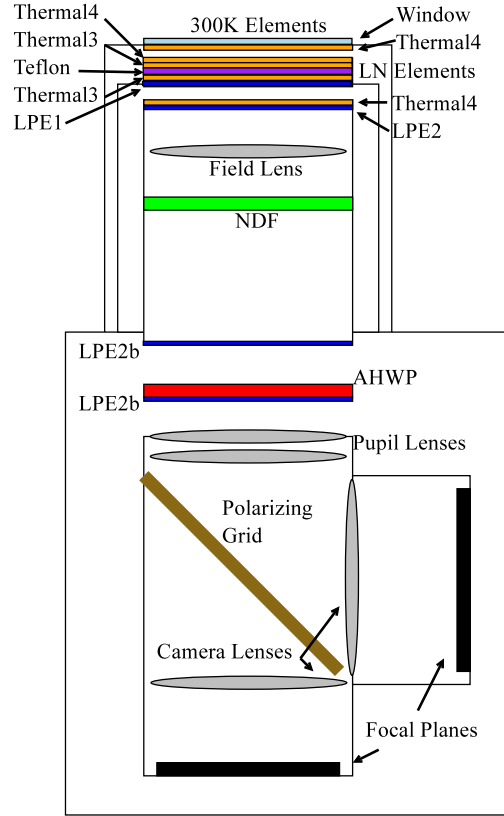
Figure 3.7: Final filter and other optical element positions for ground and flight configurations. The 300K, and LN mounted filters are specified, with the remaining elements mounted to the LHe stage, with thermal filters (orange), LPE filters (blue), Teflon filter (purple), and NDF (green, used only for ground testing).

For a half-wave plate, this retardance is tuned to be exactly 180° to reverse the output polarization of the extraordinary wave relative to the ordinary axis. The retardance is obtained by using a HWP of the correct thickness for the frequency of light incident on it, and is governed by,

$$\phi = \frac{2\pi \Delta n \nu L}{c} \tag{3.4}$$

for frequency ν, thickness L, and difference in indeces Δn.

This is often used in polarimetry to modulate the measured polarization state in order to discrimiate against contaminant and systematic effects. A HWP rotating at frequency f, will rotate a static input linear polarization at $2f$. This has the benefit of
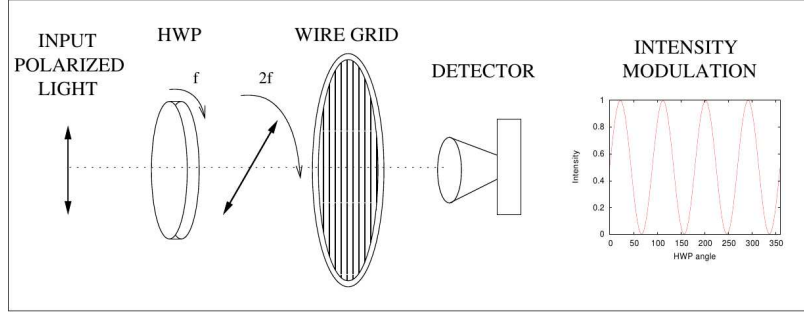
Figure 3.8: Rotating HWP modulation of output polarization angle, from [19].

shifting the input signal at $2f$, away from the first harmonic of any rotation-synchronous signals. The addition of a polarizing grid after the rotating HWP again shifts the modulation frequency of the input signal by another factor of 2, to frequency $4f$, due to the double-pointed arrow nature of polarization if the signal is measured by an intensity sensitive detector, such as a bolometer. This polarization modulation method is utilized by EBEX to convert each bolometer into an independent polarimeter once the position of the HWP is encoded.

In order to use a HWP for achromatic light and not just a single frequency, a stack of five cylindrical, 1.62 mm thick sapphire plates are used with relative shifts in the extraordinary axes. The relative shifts between the plates are tuned to obtain an overall phase shift for the five-stack of 180° over the three EBEX bands [29]. This five-stack is the achromatic half-wave plate (AHWP).

While the AHWP is optimized for linear polarization rotation over the range of all three frequency bands, the other properties of the AHWP, like output rotation phase and depolarization, vary with frequency. The output rotation phase, also called the frequency-dependent polarization rotation, is the relative rotation of the output linear polarization due to a varying effective ordinary axis of the AHWP with frequency and is critical to calibrate in order to obtain the absolute measured polarization angle of signals from the sky.

The degree of depolarization of the AHWP stems from deviations from ideal HWP behavior as a function of frequency and causes leakage from linear polarization states into intensity and circular polarization. In Stokes parameters, I, Q, U, and V, this
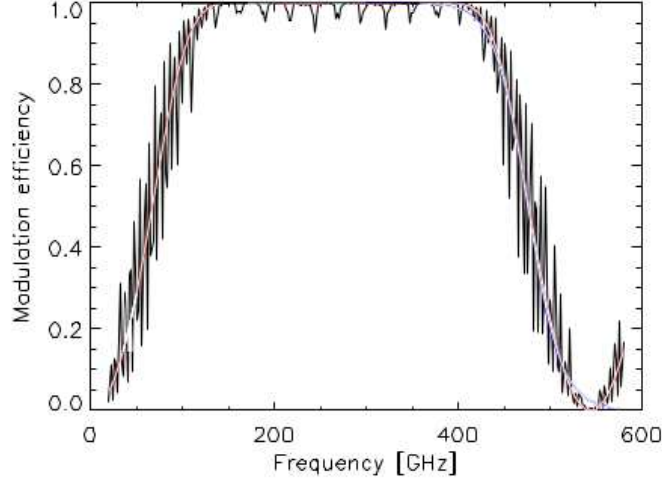
Figure 3.9: Simulated 5-stack AHWP PME versus incident frequency produced by T. Matsumura.

leads to $Q, U \rightarrow I, V$. This is predicted to be a small effect and is quantified by the polarization modulation efficiency (PME), a measure of the difference between maximum and minimum measured intensities, see Section 5.2. PME near unity indicates low depolarization and little $Q, U \rightarrow I, V$. A simulation of the predicted PME for the EBEX AHWP configuration is shown in Figure 3.9. This predicts a band-average PME $> 98\%$ for all three EBEX frequency bands.

The AHWP is situated beneath the optics stack in the EBEX receiver and is mounted in a rotor mechanism of a superconducting magnetic bearing (SMB). The bearing consists of a strong permanent ring magnet with rotationally-symmetric magnetic field suspended above a ring of Type-II superconducting ceramic tiles. The tiles, in effect, freeze the magnetic field from the permanent magnet inside the tiles and resist change in the field associated with non-rotational movement of the magnet. In EBEX, the permanent ring magnet is located in the rotor with the AHWP which is then free to rotate with very low resistence due to the lack of mechanical contact between the rotor and the rest of the rotation mechanism and negligible air-drag due to the vacuum environment. The rotor does experience some resistence to rotation due to non-uniformities in the magnetic field of the ring magnet causing hysteresis losses in the superconducting tiles

and eddy currents established in close metal components.

The rotor of the SMB is rotated at uniform speed using a belt made of a Kevlar weave coupled to a pulley driven by a brushless DC motor located outside the 300K shell of the receiver. A low thermal conductance drive shaft couples the DC motor to the drive pulley and is thermal attached to both the VCS1 and LHe stages to minimize conducted load on the LHe stage. Miniature circular ball-bearings support the drive pulley and a separate tensioner pulley, designed to provide a uniform tension on the Kevlar belt to minimize belt slippage.

The position of the SMB rotor is encoded by an optical chop encoder wheel with 200 slots and is measured relative to a double-wide slot of measured relative position to the AHWP ordinary axis. Cryogenic LEDs and photodiodes record the movement of the slots so that the absolute angle of the rotor can be reconstructed.

A system of Kevlar strings and springs coupled to grippers and a cryogenic stepper motor are used to grip the rotor assembly prior to the cooling of the superconducting tiles under their critical temperature. The position of these grippers, the temperature of various components in the SMB assembly, and the optical encoder signals are sent along with the gripper motor currents through cryogenic wiring that passes through the thermal shells of the receiver to a connector on the 300 K shell. The signals are then recorded.

Further discussion of the AHWP and SMB subsystems can be found in [23].

3.5   Optics Box

Below the AHWP subsystem is the first sub-Kelvin stage of the EBEX instrument. The optics box is the support structure for the remaining cold optical elements in the receiver, including the two pupil lenses, the polarizing grid mentioned in Section 3.4, and the two camera lenses, one for each of the two focal planes. The optics box is kept at temperatures between 950 mK and 1.1 K by the He8 adsorption refrigerator discussed in Section 3.8.

The optics box was designed to have minimum mass while still remaining rigid to keep deflection of the upper portions of the structure to less than 0.127 mm, the design specifications of the optical system. The receiver is rotated about a horizontal axis to

(a) Optics box model.

(b) Receiver instrument, photo by A. Aboobaker.
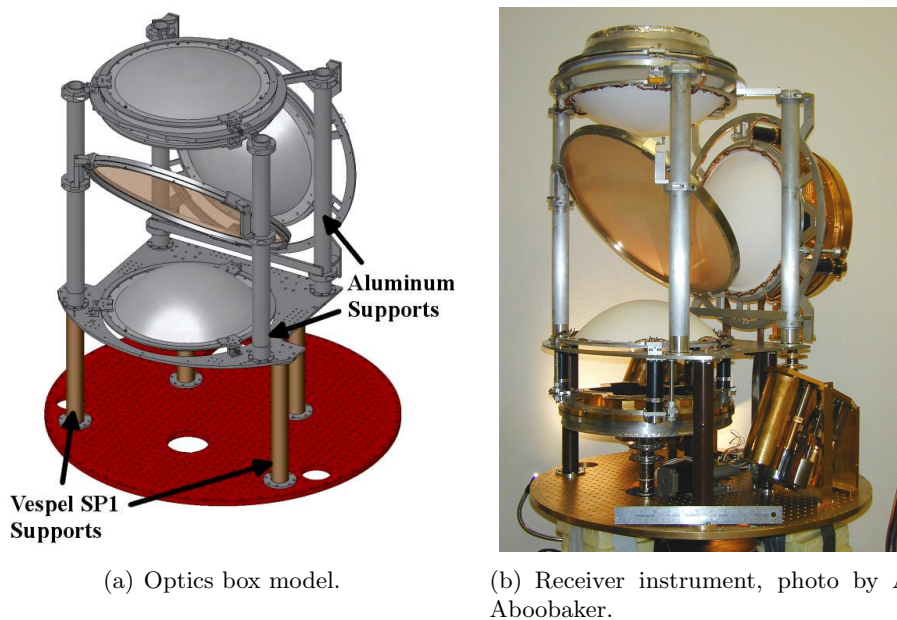
Figure 3.10: Receiver optics box model and construction.

scan in elevation during flight operations, so the optics box must keep rigid in both vertical and horizontal orientations. To accomplish this, four 3.2 mm thick, 38 mm outer diameter aluminum support tubes are mounted to the base plate of the optics box with a rigid ring connecting the tubes at the top of the structure, see Figure 3.10(a). A second vertical mounting ring is attached at the back of the optics box to allow for mounting of the second camera lens and focal plane. The polarizing grid is mounted at a 45° angle between the two focal planes to reflect one polarization state to the second focal plane and transmit the other to the first focal plane.

Besides the support structure for the cold optical elements, the optics box also has the mechanisms to align the individual elements to each other. These mechanisms consist of series of rounded-tip screws that allow adjustment of each element vertically from three points along the element's edge, providing two rotational and one translational degrees of freedom. Another set of three rounded-tip screws push the element horizontally from the same three points along the edge, providing the other two translational degrees of freedom. The third rotational degree, a rotation about the symmetry axis of the element, is not adjusted. See Section 4.3 for a further discussion of the alignment

of the optical system.

To improve the optical performance of the EBEX optical system, the inside of the optics box is coated in Bock black, a cryogenic millimeter-wave absorber that consists of STYCAST 2850 [9], 10 micron glass beads, and carbon black. The optics box has aluminum shielding to block errant light from entering the optical path that is plated with 0.127 micron thick gold on the outside surface to reduce absorptivity and hence reduce load on the sub-Kelvin stage.

The optics box also houses a "reverse" bolometer, called the stimulator, used for in-flight sensitivity calibration of the detectors in the focal planes. The stimulator receives a small, roughly 10 mA, current that warms the bolometer which then emits onto the back surface of the polarizing grid. Since the emission from the stimulator is unpolarized, one polarization state will illuminate each focal plane equally. By measuring the magnitude of the EBEX detectors' responses to the same stimulator "flash" over the course of a period of time, any change in responsivity can be tracked.

To thermally isolate the optics box from the 4.2 K cold plate base of the instrument, four 299 mm long, 3.59 mm thick, 38.1 mm outer diameter Vespel SP1 tubes support the optics box base plate. These tubes were designed to support the weight of the cold instrument as well as survive the launch and termination impacts from flight. To thermally isolate the colder sub-Kelvin thermal stages, two sets of three Vespel SP22 tubes 107.3 mm long, 0.635 mm thick, with 31.8 mm outer diameter support the two focal planes away from the optics box base plate and vertical mounting ring. An intermediate-temperature thermal intercept is placed in the middle of all of these tubes, 72.0 mm from the optics box base plate and vertical mounting ring.

These supports are designed to survive impacts of 10 g's vertically and 5 g's at a 45° angle, specifications set by NASA. The stresses in the Vespel legs under these loads was calculated by first finding the sectional moment of inertia, I, and the sectional modulus, Z,

$$I = \frac{\pi}{64}(D^4 - d^4) \tag{3.5a}$$

$$Z = \frac{2I}{D} \tag{3.5b}$$

where D and d are the outer and inner diameters of the legs, respectively. The maximum tensile and flexural stresses can then be calculated from formulae for load applied to

	Tensile		Flexural	
Section	**Stress**	**Strength**	**Stress**	**Strength**
SP1	2.37	72	0.00	83
SP22 (Long, H)	4.42	45	0.00	62
SP22 (Short, H)	4.42	45	0.00	62
SP22 (Long, V)	0.00	45	*20.83*	*62*
SP22 (Short, V)	0.00	45	10.21	62

Table 3.4: Tensile and flexural stresses and ultimate strengths for the Vespel SP1 legs, and the short and long sections of the Vespel SP22 legs for the H and V focal planes for an applied 10g vertical load. All values are in MPa with the limiting element and case italicized. Ultimate strengths for the materials from [6].

the end of structural beams with one end fixed and the other guided,

$$S_{\text{tensile}} = \frac{W}{A} \tag{3.6a}$$

$$S_{\text{flexural}} = \frac{W l^3}{12 E_{\text{flexural}} I} \tag{3.6b}$$

where W is the load applied, A is the cross-sectional area, l is the length, and E_{flexural} is the flexural modulus. The 1g load applied is one quarter of the weight of the optics box for the Vespel SP1 legs, and one third of the weight of the focal plane for the Vespel SP22 legs. The calculated loads and ultimate strengths are shown in Tables 3.4 and 3.5 and show a minimum safety factor of three between calculated load and ultimate strength. Despite this margin, the North American test flight demonstrated these legs were insufficient to survive actual flight termination impacts. As such, aluminum catches that support the colder sub-Kelvin thermal stages in the case of Vespel SP22 failure are also installed on the optics box.

The thermal conduction performance of these supports are discussed in Section 4.1.3.

	Tensile		Flexural	
Section	**Stress**	**Strength**	**Stress**	**Strength**
SP1	0.84	72	15.87	83
SP22 (Long, H)	1.56	45	7.36	62
SP22 (Short, H)	1.56	45	3.61	62
SP22 (Long, V)	1.56	45	7.36	62
SP22 (Short, V)	1.56	45	3.61	62

Table 3.5: Tensile and flexural stresses and strength for the Vespel SP1 legs, and the short and long sections of the Vespel SP22 legs for the H and V focal planes for an applied 5g load at a 45° angle. All values are in MPa. Ultimate strengths for the materials from [6].

3.6 Focal Planes

At the end of the EBEX optical system are the two focal planes where the telescope focuses the light from different directions in the sky onto a plane with each direction corresponding to a different position on the plane. The light is divided into two polarization states that are sent to the two focal planes by the polarizing grid mentioned in Section 3.5. The detector arrays are placed at these two focal planes to optimally couple to the light. Light that passes through the polarizing grid continues to the H focal plane, named due to the horizontal orientation of the plane, and light that reflects off the polarizing grid continues to the V focal plane, which is mounted vertically.

The structure of the focal planes is designed to support and protect the detector arrays as well as keep the detectors at an operational temperature. The focal planes are cooled by the coldest sub-Kelvin stage of the adsorption refrigerators, the ultrahead, discussed in Section 3.8, that keeps the H focal plane at 250 mK and the V focal plane at 270 mK.

Each focal plane consists largely of two 0.127 micron gold-plated aluminum pieces, a horn array and a waveguide array. The horn array is a 23 mm thick plate with 968 smooth-walled conical feedhorns that couple to individual detectors beneath them, and is designed to couple the Gaussian telescope beam to the focal planes. For ease of
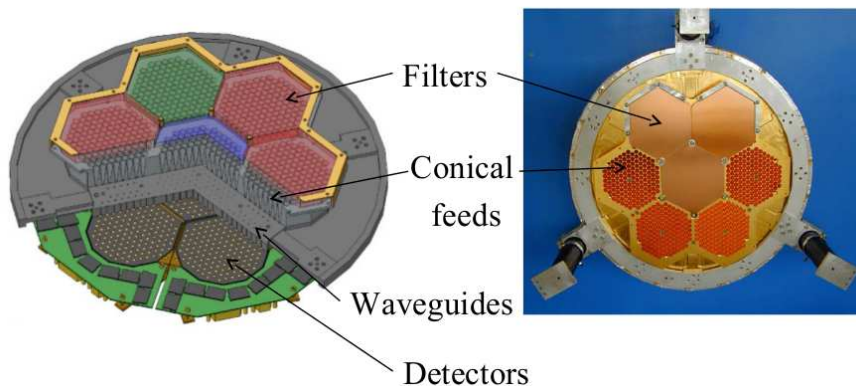
Figure 3.11: Focal plane structure, including the band-defining filters, horn and waveguide arrays, and detector wafers.

fabrication, the diameter of each cone is kept constant while the opening angle of the cone is dependent on the frequency band of the detector beneath the horn. Section 4.3 further discusses the performance of the horn arrays. The waveguide array is a 10 mm thick plate with 968 cylindrical waveguides immediately beneath the feedhorns and above the detector arrays. The primary purpose of the waveguide array is to define the low-frequency end of each frequency band as discussed in Section 4.4, while the array also acts as a large heatsink to regulate the temperature of the detectors.

Mounted on top of the horn arrays are seven sets of band-defining filters that set the high-frequency ends of the frequency bands as also discussed in Section 4.4. These filters are thicker versions of the LPE filters mentioned in Section 3.3.2. Due to the thermal contraction of the polypropylene substrate of the filters, BeCu springs are used to ensure proper placement of the filters on the horn arrays.

The back of each focal plane is enclosed with an aluminum shell to eliminate light contamination and establish an RF-clean environment for the detector arrays, as discussed in Section 4.2. To thermally couple the detectors to the ultrahead, a OFHC copper ring is placed between the waveguide array and aluminum shell with flanges that connected to each Invar plate. A separate flange extends outside the RF-clean environment that then couples to the ultrahead.
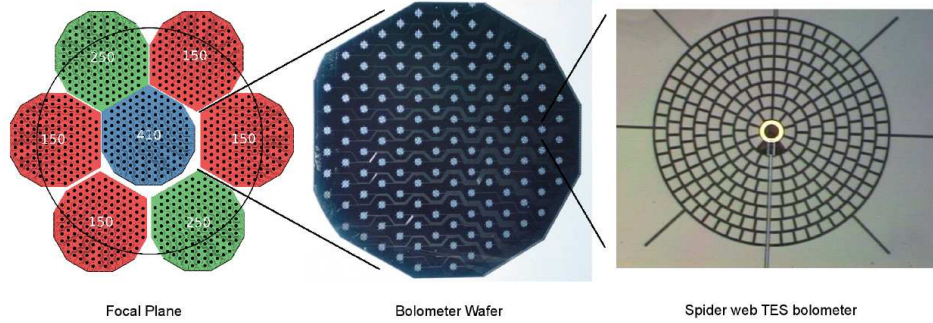
Figure 3.12: Depiction of the scaling from focal plane, 300 mm in diameter, to silicon wafer, 86 mm wide, to individual detector, 2.1 mm wide. The TES is the rectangular structure under the gold central ring in the right image. Images from UC Berkeley

Detectors

The detector arrays in the focal planes consist of transistion-edge sensors (TESs) thermally coupled to spider-web bolometers, Figure 3.12. The bolometer absorbs incident light and warms the TES located in the center of the spider-web. The TES is a titanium-aluminum bilayer superconductor with thicknesses tuned to achieve critical temperatures, T_c, with measured medium values of 486, 482, and 470 mK for the 150, 250, and 410 GHz detectors. The TESs have sharp transitions between a normal, Ohmic resistive regime and superconducting regime, Figure 3.13, and are radiatively and electrically heated to remain at a temperature on that transition to increase resistive response to temperature. The TESs are voltage-biased by the readout electronics so that the total incident on the TES,

$$P_{\text{total}} = P_{\text{rad}} + P_{\text{elect}} = \tilde{G}(T_{\text{det}} - T_{\text{bath}}) \tag{3.7}$$

is kept close to constant due to the increased resistance response of P_{rad} due to warming and the negative electrical power feedback with increasing resistance. The current through each detector then correlates to the changes in incident radiative power. The sensitivity of the detectors to radiative power also depends on the temperature difference between the detectors and bath temperature and the thermal conductance between the TES and bath.
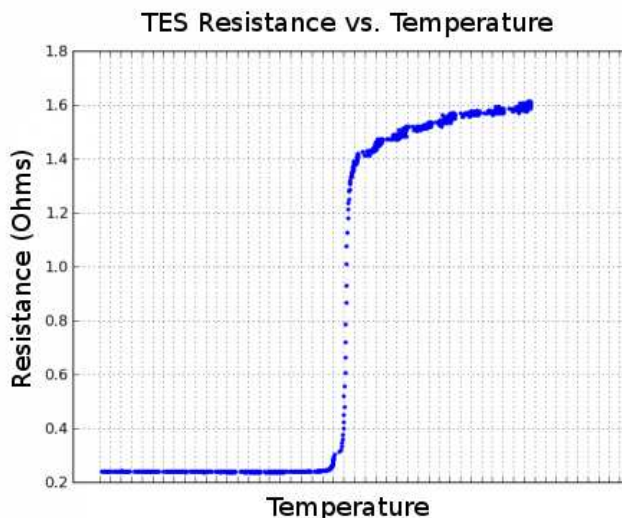
Figure 3.13: Example resistance versus temperature profile for EBEX TES.

The detector current values are readout through a digital frequency-domain multiplexing (DfMUX) scheme and electronics developed by McGill University. In order to reduce the total number of wires traveling to the coldest stage of the instrument, and thus the thermally conducted load, the multiplexing scheme is able to voltage-bias and readout the current from 16 detectors (x16 multiplexing) simultaneously through a single pair of wires. To accomplish this, the set of 16 detectors are given different resonance frequencies with series LC circuitry shown in Figure 3.14, and the readout electronics biases the detectors by application of a voltage "comb" at these frequencies. The original "comb" is cancelled, or nulled, by a similar voltage "comb" that is out of phase with the original, leaving only the change in current induced by light on the detectors. The changes in current are measured by superconducting quantum interference devices (SQUIDs) that also amplify the signals, which are then digitally converted and recorded.

The detectors themselves are fabricated by the University of California at Berkeley on silicon wafers with 141 detectors on each wafer. It should be noted that a focal plane with 7 wafers has 987 detectors, however, limitations in the horn and waveguide array construction limits the number of detector getting light from the sky to be 968. In addition, the detector readout scheme also limits the number of detectors that can
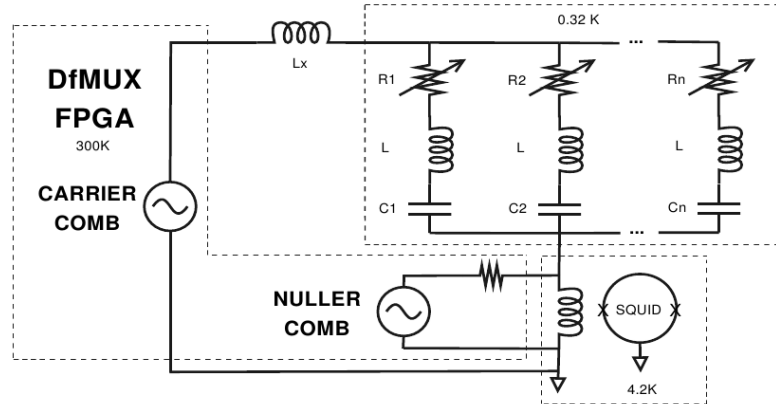
Figure 3.14: Simplified schematic of the DfMUX readout scheme. L_x represents any stray inductance in the circuitry, from [19].

be readout to be 896 for each focal plane, for a total of 1792 possible detectors that can be readout over both focal planes.

These wafers are fabricated to have the desired TES transistion temperature and bolometer thermal conductance as required for each frequency band as well as $\frac{\lambda}{4}$ metal backshorts to maximize absorption in the detectors. The detector wafers are mounted to the underside of the waveguide arrays with aluminum holders that also hold the circuit boards with the inductors and capacitors that set the frequency resonances of each detector in the multiplexing readout scheme. These LC boards are electrically connected to the detector wafers by aluminum wire-bonds and connect to the rest of the readout electronics through tinned-copper wiring terminating in a micro-D connector. The detector wafers are mounted with cryogenic grease on Invar plates to mimic the low thermal contraction of the silicon and minimize damage and movement of the wafers due to the contraction of the aluminum waveguide arrays. The Invar plates also help regulate the temperatures of the wafers due to their large relative specific heat.

(a) RF tower model with cutaway. (b) RF tower assembly in situ.
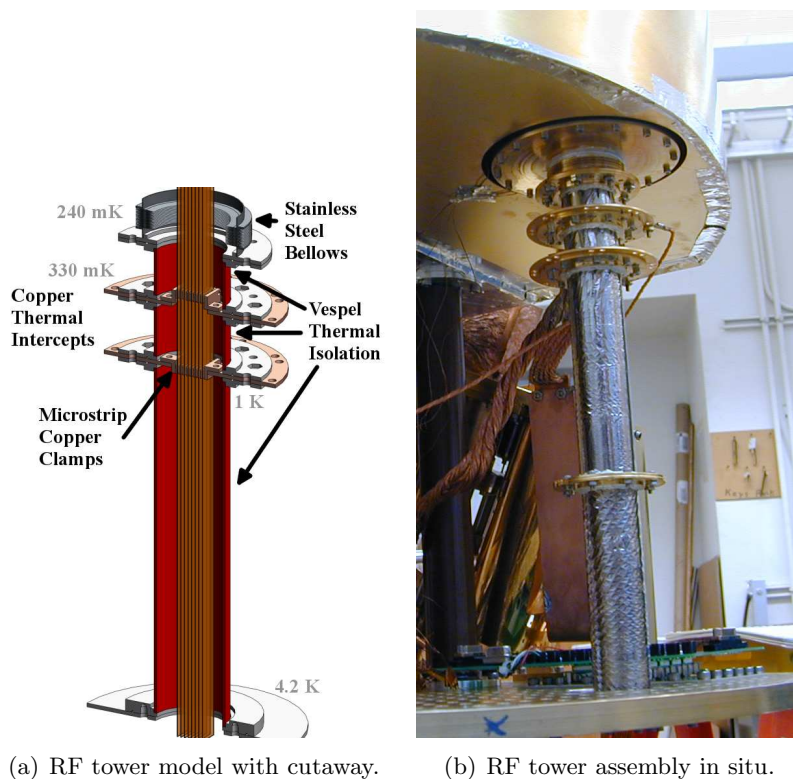
Figure 3.15: RF tower model with cutaway to show interior microstrip assemblies and in situ picture. The RF tower shown in situ is for the V focal plane and has additional length to reduce thermal conductive loading.

3.7 RF Towers

Between the focal planes and the cold plate of the instrument are two structures called the RF towers. The purpose of these structures is threefold: to facilitate the transmission of detected signals from the LC boards to the SQUID amplifiers beneath the cold plate, maintain the RF-clean environment inside the focal planes and in the SQUID cavity, and perform these two tasks between the 250 mK stage and the 4.2 K cold plate.

Each RF tower is comprised of six components, the first of which is a stainless steel bellows that attaches to the metal shell on that back of each focal plane. The bellows are necessary to make the mechanical connection between the focal plane and RF tower despite possible misalignment of the two structures due to machining tolerances on the various components that support each. The next three components of an RF tower
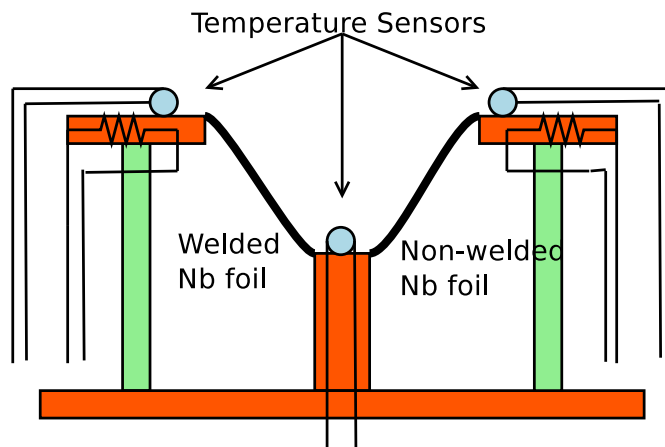
Figure 3.16: Setup for measuring the thermal conductivity of two strips of Nb foil, one welded and one not. The green components represent the G-10 thermal isolation and the orange represents copper components.

are three thermal isolation segments to optimize the loading on the sub-Kelvin stages, discussed in Section 4.1.3.

The RF-clean environment is maintained inside the RF tower by use of a continuous conductive layer around the exterior of the structure, including the thermal isolation segments, consisting of 99.9% purity 5 micron thick Niobium foil, provided by Smart Elements. In order to give the foil a cylindrical shape, the Niobium foil was spot welded along a vertical seam spanning the length of the RF towers. This change in structure of the Niobium foil prompted measurements of the electrical and thermal conductivities of the spot-welded foil pieces. Test pieces of the welded Niobium foil were slowly submerged in LHe and the temperature and resistance of the foil were measured. At close to 9 K, the pieces underwent a transistion and became superconducting, agreeing with the measured $T_C = 9.2$ K for Niobium.

The thermal conductivity was measured using two Niobium foil pieces, one welded and another not welded to act as a control, each with one end thermally isolated from a 4.2 K cold plate using G-10 rods, and the other end sunk to the cold plate. Silicon diode (SiD) temperature sensors on both ends of the foils were readout and small resistive heaters on the isolated stages were used to vary the isolated temperatures. A diagram of the experimental setup is shown in Figure 3.16. To obtain the thermal conductivity of
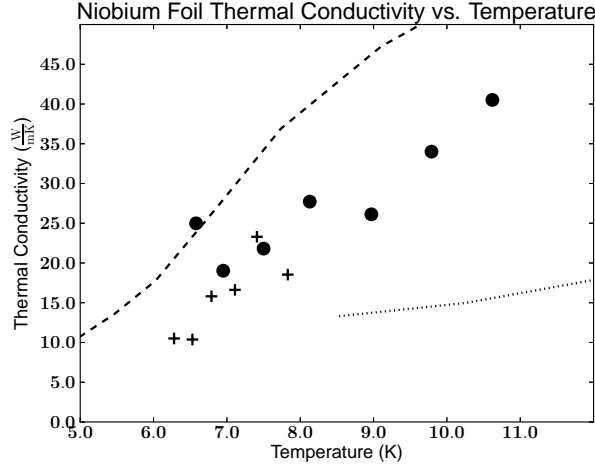
Figure 3.17: Measured thermal conductivity values for welded (•) and non-welded (+) Nb foil samples. Samples are reported by supplier as 99.9% Nb, with measured 99.9+% (dashed) and 99.99% (dotted) Nb foil thermal conductivity values from [15].

the Niobium foils, the conducted powers of the G-10 rods, and Manganin and phosphor bronze wiring to the temperature sensors and heaters, using conductivites from [39] and [25], were subtracted from the powers applied from the heater and SiD temperature sensor. This was performed over an isolated temperature range of 6.08 to 10.62 K, and the Nb conductivities from these measurements are shown in Figure 3.17. The welded foil conductivities agree with the non-welded foil conductivities and the power-law fit to the data gives $k_{\mathrm{Nb}}(T) = 0.290T^{2.1}$ $\frac{\mathrm{W}}{\mathrm{m\cdot K}}$. These conductivities are consistent with values of similar purity Nb reported in [15].

The fifth component is a small wiring assembly used to transmit signals from temperature sensors inside the focal plane. The final component of the RF towers are the wiring that transmit signals from the detector arrays. Both sets of wiring run through the interior of the stainless steel bellows and thermal isolation segment tubing, as shown in Figure 3.15.

The RF properties of the RF towers are discussed in Section 4.2.

3.7.1   Microstrips

To transmit signals electrically from LC boards to SQUID amplifiers, wiring assemblies called microstrips were designed and constructed. Operating on the transistion edge between Ohmic resistor and superconducting device, the TESs have a relatively small internal resistance of about 1 Ω at the beginning of the transistion to superconductor. In order to measure the changes in the resistance of the TESs, the rest of the readout pipeline prior to amplification requires superconducting wiring to avoid dominating the TES resistance with other stray resistances. The wiring in the microstrips consists of flattened NbTi wire with a critical temperature of 9.2 K, well above the temperature of the LHe stage in which it is mounted. NbTi also has relatively low thermal conductivity for a superconducting material which reduces the conductive load on the sub-Kelvin stages from the microstrips.

Since NbTi has a very low solderability, the flat NbTi wire is fabricated from 0.191 mm diameter NbTi wire that is copper-clad with total diameter of 0.305 mm, supplied by Supercon, Inc., and rolled flat to thickness of about 33 microns. The flattening of the wires was performed by the H Cross Company. Since the copper is significantly softer than the NbTi, the final cross-sectional dimensions of the NbTi are 762 by 33 microns as the copper migrates to the edges of the flattened material during the rolling process. The copper-cladding is removed from the entire length of the flattened wire except for the ends using a nitric acid wash. The copper-cladding on the ends remains to allow soldering of the wire to connectors.

The microstrips each consist of 8 pairs of flattened NbTi wire and, with the x16 multiplexing scheme used in the detector readout, each microstrip carries the signal from 128 detectors. To isolate the wires in each pair, a film of 7.6 or 12.7 micron thick Kapton HN is placed between all the pairs. The 12.7 micron film was used primarily for microstrips during the initial testing phases of the design, and the 7.6 micron film used for microstrips used in the EBEX instrument. The adjacent pairs have 940 micron spacing between them and are secured in their position by a layer of 64 micron thick Kapton HN tape with silicone adhesive. The overall construction is shown in Figure 3.18. This geometry is called a parallel-plate waveguide (PPW), however, due to initial convention, it will still be referred to as a microstrip. Details for the construction of the microstrips can be found in [36].

(a) Diagram of microstrip geometry.

(b) Image of copper-clad NbTi wire ends.

(c) Image of complete microstrip assembly.
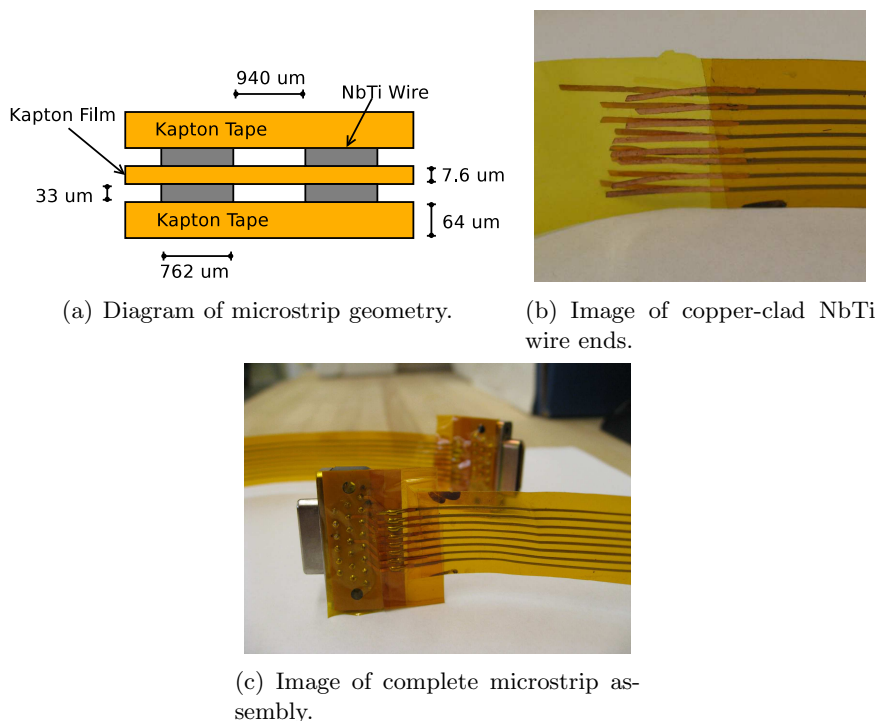
Figure 3.18: Design and steps in fabrication of the microstrip assemblies.

The ends of the flattened wires in each microstrip are soldered to small flexible circuit board attached to a micro-D connector on each end. The ends of the microstrip can then be mated to corresponding connectors from the LC boards and on the SQUID amplifier boards.

The geometry described above was chosen in the design of the microstrips due to the details of the digital frequency-domain multiplexing readout. Since signals for separate detectors are measured in the frequency-domain, stray inductance in the readout wiring can shift the resonance frequencies for detectors as well as reduce response due to the stray impedance in the wiring. To minimize the stray inductance, the PPW geometry was chosen over more traditional geometry such as twisted pair geometry, which has inductances on order $4 - 8 \frac{\text{nH}}{\text{cm}}$. Given the length of microstrips needs to be $700 - 950$ mm, this would give inductances as high as 760 nH, which is not negligible compared to the $13 - 22$ μH indutance values used in the LC circuitry for setting the detector resonances. For parallel, perfectly conducting wires of constant arbitrary geometry, the

capacitance and inductance per length are related as,

$$\mu\epsilon = \frac{L}{l}\frac{C}{l} \tag{3.8}$$

For PPW geometry, assuming small separation of the wires compared to their widths, the inductance per length is then,

$$\frac{L}{l} = \mu\epsilon\frac{h}{\epsilon w} = \mu\frac{h}{w} \tag{3.9}$$

for μ and ϵ of the medium between the wires which are separated by h and have width w. The relative permeability of Kapton HN is vary close to one and the relative permittivity is 3.5 [7], so the predicted inductance per length for the given geometries are 0.126 and 0.209 $\frac{nH}{cm}$ for the 7.6 and 12.7 micron films, respectively.

Capacitance measurements were made at room temperature of one of the microstrip assemblies prior to attachment of the flexible circuit boards using an SRS720 LCR meter. The capacitance was measured across the two flattened wires of each pair in the microstrip for 10 microstrip assemblies between June 2008 and March 2009 using the 12.7 micron film spacer. From the capacitance measurements and known lengths of the microstrip, the average inductance per length for each of these 10 microstrip assemblies can be calculated from Equation 3.8 and are shown in Table 3.6.

As the construction process of the microstrip assemblies improved, the inductance per length values decreased, however, the values are still a factor of 3 higher than the predicted 0.209 $\frac{nH}{cm}$. This can be partially attributed to an adhesive spray used in the construction process effectively increasing the separation between the wires in each pair beyond the 12.7 micro film thickness. The microstrips still showed a improvement in inductance compared to the twisted-pair geometry. Cold measurements of the stray inductance of detector circuits using the method described in [19] showed inductances per length of 0.58 $\frac{nH}{cm}$ for the microstrips, in good agreement with the warm measurements.

Given the empirical factor of 3 between the theoretical and measured values of the inductance, the EBEX instrument microstrips are expected to have inductances of 24.5 and 33.3 nH for the 700 and 950 mm microstrips, respectively. These values are suitably small compared to the resonance defining inductances to have a negligible affect on the resonance frequencies and detector response.

Microstrip Index	Inductance per length	Uncertainty
1	0.98	0.08
2	1.1	0.08
3	0.71	0.04
4	0.63	0.04
5	0.63	0.04
6	0.67	0.04
7	0.71	0.08
8	0.59	0.04
9	0.71	0.08
10	0.59	0.04

Table 3.6: Average inductance per length and uncertainty, in units of $\frac{\text{nH}}{\text{cm}}$ for 10 microstrip assemblies. Uncertainty is calculated from the standard deviation of the inductance per length measurements of the 8 pairs of wires in the microstrip.

3.7.2 Thermal Intercepts

In order to optimize the loads on the sub-Kelvin stages, two thermal intercepts are established inside the RF towers at intermediate temperatures between the 250 mK focal plane and the 4.2 K cold plate. These thermal intercepts use the He8 coldhead temperature of 900 mK and the He10 interhead temperature of 320 mK, discussed in 3.8, with the mentioned first thermal isolation segment spanning between the 250 mK and 320 mK intercept, the second segment spanning between 320 mK intercept and the 900 mK intercept, and the final segment spanning between the 900 mK intercept and 4.2 K. The thermal intercepts consist of copper annuli that are mounted between the isolation segments. These annuli protrude from the RF tower structure and are attached with copper strapping to the fridge heads.

In order to preserve the RF-clean environment inside the RF towers and thermally sink the microstrip and other wiring assemblies to the intercept temperatures, the copper annuli have inward flanges that attached to copper clamps that are compressed around

copper tabs glued to each microstrip assembly. This is shown in Figure 3.15. This thermal intercept scheme makes the assembly of an RF tower more complicated as it first requires the connection of a single thermal isolation segment with copper annulus. The wiring assemblies can then be clamped down to the annulus with the glued copper tabs and another isolation segment can be installed. The last copper annulus is then connected and attached to the wiring assemblies, and then the final thermal isolation segment can be installed with the bellows. The RF tower assembly can then be installed in the EBEX instrument.

3.8   Adsorption Refrigerators

In order to obtain sub-Kelvin temperature stages in the EBEX instrument, two closed-cycle pressurized Helium adsorption refrigerator are used. The adsorption refrigerators work on the principle of evaporative cooling to lower the temperature of liquid helium reservoirs below the 4.2 K boiling point of ^{4}He at atmospheric pressures. The two refrigerators were designed and constructed by Chase Research Cryogenics.

A single adsorption stage in a fridge consists of a liquid reservoir, condenser, activated charcoal "pump" with external heater, and gas-gap heatswitch between the charcoal pump and mainplate. The reservoir, pump chamber, and pipe between them compose a closed cavity filled with high-pressure Helium gas. The pipe between the reservoir and pump chamber is thermally connected to the mainplate of the fridge, which is strongly thermally sunk to the LHe bath to maintain a temperature close to 4.2 K for this condensing pipe. The gas-gap heatswitch is a smaller version of the above stage, except the gas inside the heatswitch is not at sufficient pressure to condense. Inside the gas-gap heatswitch is small charcoal pump with external heater attached and some amount of pressurized gas.

The various heaters involved in each stage of the fridges are controlled through an electronics board developed by the Weizmann Institute of Science. This board can apply either a high, about 90 mA, low, about 50 mA, or no current to the pump heaters and either a high, 0.25 mA, or no current to the heatswitch heaters. These current levels are hardware adjustable on the board itself.

A cycle of the stage described begins with the stage at a temperature of 4.2 K. At

this temperature, the helium gas inside the stage is largely adsorbed to the large surface area of the activated charcoal pump. The gas-gap heatswitch heater does not receive current and so the heatswitch pump is at 4.2 K and the gas inside the heatswitch is also adsorbed to the small heatswitch pump. In this state, the gas is not available to thermally couple the ends of the heatswitch, the mainplate and the main stage pump, thus thermally isolating the stage pump. This is described as the open stage of the heatswitch. The heatswitch is small to ensure only a small current, and thus small dissipated power, is required to keep it in this closed state.

The first step of a cycle away from this baseline state is to run current through the heater for the stage pump to warm it above 35 K, usually to 40 − 45 K, which causes the helium gas to desorb from the charcoal pump. This free helium gas then condenses on the length of pipe thermally connected to the mainplate, and pools in the reservoir portion of the stage.

When all the helium has condensed into the reservoir, the heater to the stage pump is turned off and the heater to the heatswitch pump is turned on by sending current through it. This desorbs the gas from the heatswitch pump inside the heatswitch cavity and thermally couples the mainplate to the stage pump. This is described as the closed stage of the heatswitch. This quickly cools the stage pump below 35 K, which begin to re-adsorb any helium gas that evaporates from the reservoir. This lowers the partial pressure inside the stage cavity and cools the liquid condensate. Any other components thermally connected to the reversoir will also begin to cool.

When the stage pump reachs 4.2 K, the reservoir reaches its minimum temperature and the stage is said to be in its "cold" state. In practice, the final reservoir temperature is governed by specifics of the fridge design and by the heat load present on the reservoir. The higher load on the reservoir, the higher the evaporation rate and the higher the partial pressure inside the stage, and thus a higher temperature in the reservoir. The holdtime of the reservoir is governed by the amount of liquid condensed inside the stage and the load on the reservoir.

The heat from the stage pump after the heatswitch is closed flows to the LHe bath through high-conductance OFHC copper straps, called the cold straps, connected to the fridge mainplate. In practice, since these cold straps do not have infinite conductance, there is a temperature differential between the LHe bath and the mainplate of at most

(a) Diagram of the He8 fridge.

(b) Image of the He8 fridge.
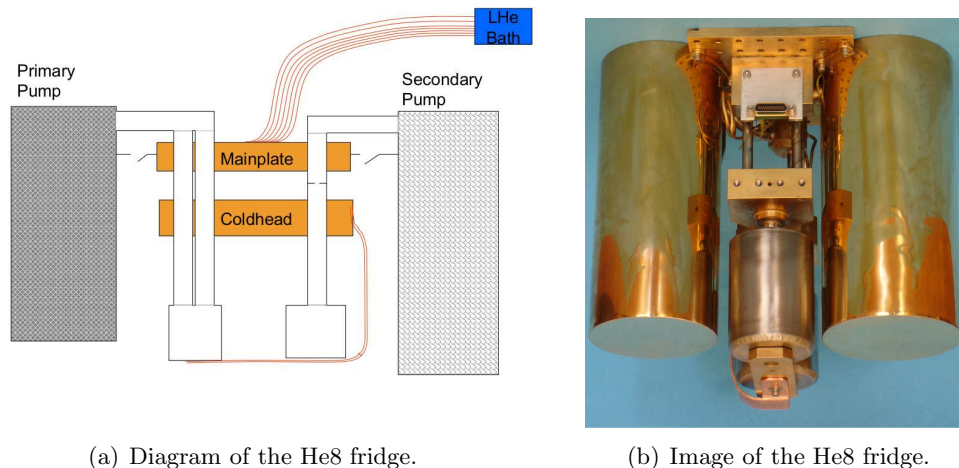
Figure 3.19: Diagram of the components of the He8 fridge and image. Photo from S. Chase.

a few Kelvin. This modifies the operation procedure of the fridges as discussed below. This process evaporates some quantity of LHe, which affects the hold time for the receiver.

The operation of the fridges is monitored by SiD and RuO_2 temperature sensors at several components in the stages, including the heaters for the stage and heatswitch pumps, along with current monitors through the stage and heatswitch heaters.

3.8.1   He8 Fridge

The simpliest adsorption refrigerator used in EBEX consists of two ^{4}He gas adsorption stages that are connected in parallel to cool the same components but are operated sequentially. Since there are two ^{4}He stages, this is referred to as the He8 fridge. A diagram of the He8 fridge is shown in Figure 3.19. Both of the stage reservoirs are thermally connected to the same copper mounting piece, called the He8 coldhead, which then is connected to the optics box and thermal intercepts in the RF towers.

During operation, the first ^{4}He stage, called the Primary stage, is cycled which pre-cools the thermal mass of the He8 coldhead and optics box for the second ^{4}He stage, called the Secondary stage. This pre-cooling of the optics box and coldhead increases the efficiency of the condensation within the Secondary stage and thus allows the Secondary
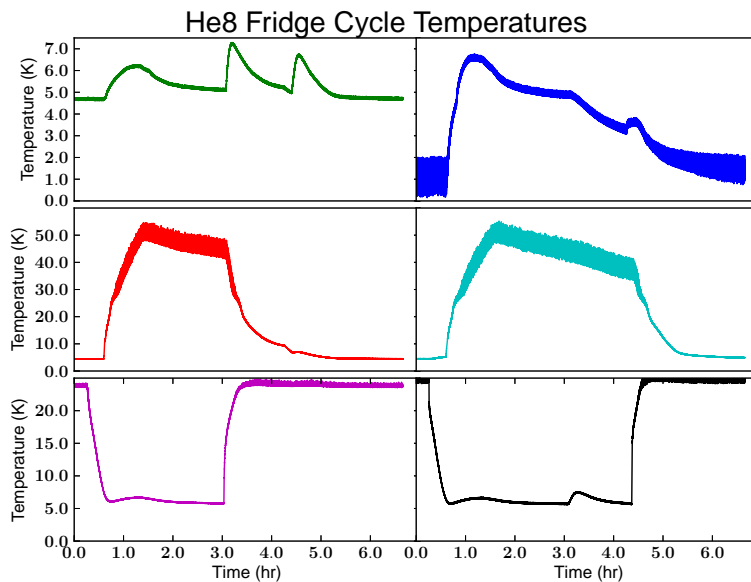
Figure 3.20: Temperature profiles for He8 mainplate (upper-left), reservoir (upper-right), primary pump (middle-left), secondary pump (middle-right), primary heatswitch (lower-left), and secondary heatswitch (lower-right) during He8 fridge cycle.

stage to cool the optics box to a lower temperature and obtain a longer holdtime. The Secondary stage is cycled once the liquid in the Primary reservoir is expended.

The temperature readout for a typical He8 fridge cycle is shown in Figure 3.20. Both the Primary and Secondary pump heaters are heated to approximately 50 K over about 50 minutes, which due to high relative power required to heat the pumps, warms the mainplate of the fridge. The heaters are then turned off, and the fridge is allowed to cool for about 120 minutes. The purpose of this cooling phase is to allow the mainplate of the fridge to cool below 5.2 K, the boiling point for the helium gas in the fridge, and allow for some time to condense the helium gas. The Secondary pump is heated to a higher temperature initially to ensure it remains above 35 K for the entirety of the Primary stage holdtime, since it cools slowly due to small residual conductance to the mainplate.

After the condensation period, the heatswitch connected to the Primary pump, the Primary heatswitch, is closed and cools quickly. This begins the pre-cooling process of the coldhead and optics box. After 80 minutes, and having cooled the coldhead to
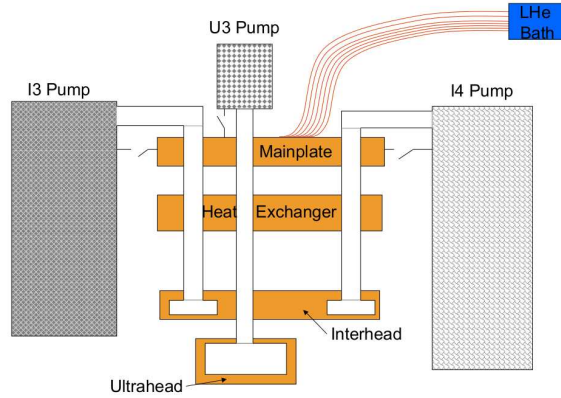
(a) Diagram of the He10 fridge.

(b) Image of the He10 fridge.

Figure 3.21: Diagram of the components of the He10 fridge and image. Photo from S. Chase.

about 3.1 K and the optics box to 3.5 K, the Primary reservoir is expended and the Secondary heatswitch is closed. The Secondary pump then cools quickly and after 7 hrs the coldhead nears its ultimate temperate of 860 mK, and the optics box reachs 900 mK.

Once all the Secondary is expended, all the gas is adsorbed by the Primary and Secondary pumps, and the heatswitches can be opened and the fridge is in a state to be cycled again.

3.8.2 He10 Fridge

The second adsorption refrigerator in EBEX consists of a single ^{4}He stage and two ^{3}He stages, and is called the He10 fridge. A diagram of the He10 fridge is shown in Figure 3.21. The ^{4}He stage, called the I4 stage, is used to cool a thermal mass common to both the I4 reservoir and the reservoir of the first ^{3}He stage, called the I3 stage. This cooling is needed to condense the ^{3}He gas, which has a lower boiling point than ^{4}He, in the I3 stage and the common thermal mass is called the interhead, which has a mounting point for thermally connecting other components. The interhead is then used to condense ^{3}He in the final stage, the U3 stage, into the U3 reservoir, which is connected to mounting
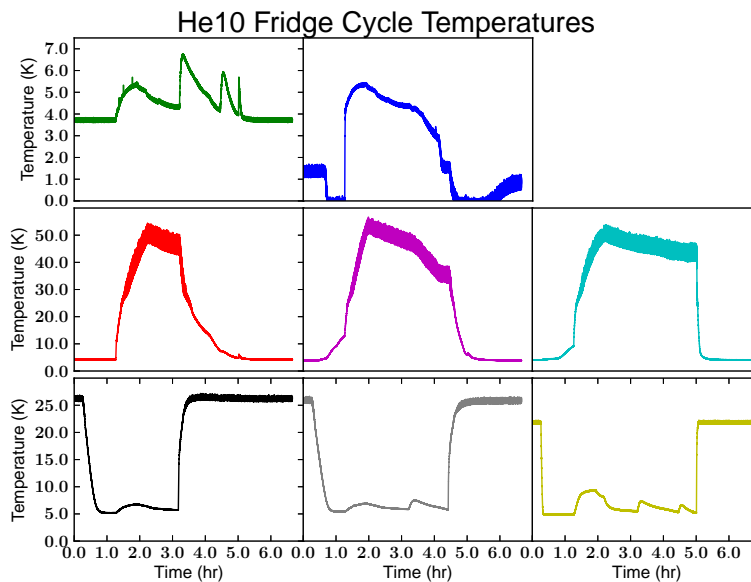
Figure 3.22: Temperature profiles for He10 mainplate (upper-left), heat exchanger (upper-middle), I4 pump (middle-left), I3 pump (center), U3 pump (middle-right), I4 heatswitch (lower-left), I3 heatswitch (lower-middle), and U3 heatswitch (lower-right) during He10 fridge cycle. Heat exchanger temperature drops below the effective range of SiD temperature sensor for negative temperature.

points called the ultrahead. Another thermal connection between the I4, I3, and U3 pipes, called the Heat Exchanger which is cooled with a weak conductive path to the interhead and cools evaporate in the pipes, is largely used to condense the gas in the ^{3}He stages.

The ultrahead is used to cool the focal planes and upper portions of the RF tower assemblies, while the interhead is connected to thermal intercepts in the RF towers and Vespel SP22 legs supporting the focal planes. The thermal intercepts are used to reduce loading on the ultrahead, see Section 4.1.3.

The operation of the He10 fridge begins with the same beginning state as the He8 fridge with all the heatswitches open and the pumps at 4.2 K. A typical He10 cycle is shown in Figure 3.22. The first steps is, again, to warm the pumps above 35 K using the I4, I3, and U3 pump heaters to desorb the gas. This process last for 45 minutes. The I3 and U3 are heated more than necessary so that they remain above 35 K for

the I4 holdtime. While the He8 fridge operation of the Primary and Secondary stages in sequence is a choice to improve the efficiency of the Secondary stage, the I4 stage must expend all liquid before the I3 pump can be cooled. Due to the superfluid state of ^{4}He beneath about 2 K at sufficient pressures, a thermal short is generated between the fridge mainplate and interhead by the capillary action of superfluid ^{4}He if the I3 stage cools the interhead prior to the I4 expenditure.

After 65 minutes, the interhead is cooled to approximately 1.7 K and the I4 is expended. The I3 heatswitch is then closed and the I3 pump cools the interhead further. The cooling of the interhead also pre-cools the ultrahead, and components attached to it, through the weak conductive link between the interhead and ultrahead. This pre-cooling of the focal planes is used to optimize the holdtime of the entire He10 fridge by exchanging holdtime in the interhead for holdtime in the ultrahead. This pre-cooling phase lasts 35 minutes, and then the U3 heatswitch is closed to begin in earnest the cooling of the U3 pump and the ultrahead. The ultrahead, H focal plane, and V focal plane reach their final temperatures of 236, 250, and 270 mK, respectively, after 200 minutes. The interhead reaches its steady-state temperature of 321 mK after 120 minutes.

Once the ultrahead or interhead is expended, the focal planes warm substantially due to lack of cooling power in the expended ultrahead, or through conductive loading of the ultrahead by the warming thermal intercepts attached to the interhead. This signals the end of the He10 cycle, at which point the heatswitch can be opened to the three stages and the He10 fridge can be cycled again. Any remaining liquid in non-expended stages is evaporated quickly as the stage pumps warm during the beginning of the next cycle.

In order to increase the He10 holdtime, the He8 fridge cycle is begun 60 minutes prior to the beginning of the He10 cycle so that the optics box and focal planes, through weak conductive paths, cool prior to the cooling of either the interhead or ultrahead stages. The fridges are cycled through software commanding of the fridge heater board run by the flight control program, FCP, based on known timing of the fridge cycle holdtimes. A full description of the fridge cycling timing is shown in Table 3.9.

3.8.3 Cold Straps

One of the major difficulties in optimization of the fridge cycles is the necessity to over-warm the pumps during the initial step of the cycles and then wait for the mainplate to cool below 5.2 K. This applies excess energy to the pumps which evaporates extra LHe once the pumps are cooled, and increases the cycling time. The mainplates are cooled by OFHC copper cold straps that then connected to copper cold "plugs" that penetrate into the LHe bath in the LHe tank of the receiver. This conductive path is limited by both the thermal resistance of the cold straps themselves, and by the contact thermal resistance between the straps and the mainplates and the straps and the cold plugs.

The cold straps consist of 85 strands of 8 AWG OFHC copper wire (99.99%, 4N, copper) and 15 strands of 8 AWG high-purity copper wire (99.99999%, 7N, copper) that are 430 mm long that are welded to OFHC copper mounting flanges at either end. The 4N purity copper is has a residual resistivity ratio, RRR, value of near 50, [43] and the 7N purity copper has an RRR of > 5000, [42]. Since,

$$RRR = \frac{\rho_{300\text{K}}}{\rho_{0\text{K}}} \tag{3.10}$$

and the cold straps operate near 0 K, by Weidemann-Franz law, Equation 4.6, $k \propto$ RRR. Using OFHC copper thermal conductivity values from [39] and Equation 3.2, we expect a conductance of 11.5 $\frac{\text{W}}{\text{K}}$ for the cold straps. Measurements of the conductance of the cold straps were performed during September 2011. The experiment consisted of applying known power to a single stage of each fridge with the heatswitches closed and measuring temperatures of various points in the path from the mainplates to the cold plugs. A temperature sensor was placed on the mainplate, on the copper mounting flange attached to the mainplate (Cold Strap 1), on the copper flange attached to the cold plug (Cold Strap 2), and the cold plug for each fridge. A diagram of the setup is shown in Figure 3.23 and the change in temperature between power on and off is shown in Table 3.7. Calculated conductance values are shown in Table 3.8.

The measurements showed a factor of two lower conductance in the cold straps themselves compared to predictions. The RRR values of the copper strands are ideal, annealled copper residual resistivities, and any deformation of the material will affect the crystalline structure in the copper and decrease the RRR values. Since the cold straps consist of multiple strands that are continually deformed during installation and
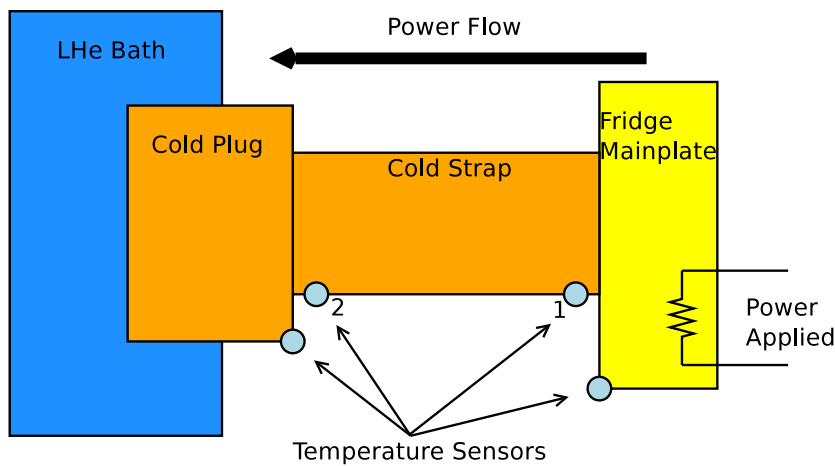
Figure 3.23: Diagram of the cold strap thermal conductance experimental setup.

Fridge	Power	Mainplate	Cold Strap 1	Cold Strap 2	Cold Plug
He8	0.2 W	0.44	0.38	0.34	0.08
He10	0.12 W	0.46	0.31	0.29	0.08

Table 3.7: Measurement of the cold strap conductance experimental data for both adsorption fridges. Temperature data shows the change in temperature between power on and off and are in Kelvin.

removal from the instrument, a factor of two decrease in thermal conductance is not unexpected.

The limiting conductances in the total conductance path are the two contact resistances where the cold straps are mounted to the mainplates and cold plugs. However, the difference between $G_{\mathrm{Strap-Plug}}$ for the two fridges show a large variability in this conductance that stems from differences in surface finish, mounting pressure, and thickness and distribution of any surface treatment, such as thermal grease.

To improve the conductance of the cold strap assembly, low thermal contraction steel spacers underneath high strength steel bolts were used to mount the strap flanges to the mainplates and cold plugs. The contraction of the copper flanges, mainplate/plug, and bolt with very little contraction in the spacer causes an increase in contact pressure between the two copper surface at cryogenic temperatures. Also, a thin layer of

Apiezon low-temperature grease is applied between on the copper contact surfaces prior to mounting to ensure even contact area.

Previous iterations of the cold strap design included a similar design as mentioned above used only the 99.99% copper strands, and solid 99.999% purity copper bars with Indium soldered copper foil mounting flanges. These designs had smaller design conductances, 0.6 and 1.4 $\frac{W}{K}$, but comparable measured conductances, 0.25 to 0.3 $\frac{W}{K}$, to the final cold strap design but were not used due to misunderstanding of the interface thermal resistance dominance of the overall conductance.

The final cold strap design provided conductances of approximately $0.3\frac{W}{K}$ during fridge cycling, consistent with measurements, and kept the maximum temperature of the He8 and He10 mainplate to 7 K, during the fridge cycles.

A discussion of the total LHe evaporation from the fridge cycles is discussed in Section 4.1.

Fridge	$\mathbf{G}_{\text{MP}-\text{Strap}}$	$\mathbf{G}_{\text{Strap}}$	$\mathbf{G}_{\text{Strap}-\text{Plug}}$	$\mathbf{G}_{\text{Plug}}$	$\mathbf{G}_{\text{Total}}$
He8	3.3	5.0	0.8	2.5	0.46
He10	0.8	6.0	0.6	1.5	0.27

Table 3.8: Calculated conductance values of the cold strap chain. The chain includes the conductance between mainplate and cold strap, $G_{\text{MP}-\text{Strap}}$, along the cold strap, G_{Strap}, between the cold strap and cold plug, $G_{\text{Strap}-\text{Plug}}$, and along the cold plug to the LHe bath, G_{Plug}. All conductances are in $\frac{W}{K}$.

He8 Time (s)	He8 Step	He10 Time (s)	He10 Step
0	Sec HSW open	0	I4 HSW open
5	Pri HSW open	5	I3 HSW open
10	I4 HSW open	10	U3 HSW open
15	I3 HSW open	15	I4 HTR high
20	U3 HSW open	20	I3 HTR high
920	Pri HTR high	25	U3 HTR high
921	Sec HTR high	2425	I3 HTR off
3626	Pri HTR off	2725	U3 HTR low
4291	Sec HTR off	2730	I4 HTR off
9691	Pri HSW close	6315	I4 HSW close
14491	Sec HSW close	10195	I3 HSW close
		12300	U3 HTR off
		12305	U3 HSW close

Table 3.9: Timing of the steps of the He8 and He10 fridge cycles. Changes of heater (HTR) current and heatswitch (HSW) state are shown. The change of the I4, I3, and U3 heatswitch state in the He8 cycle is in anticipation of the beginning of the He10 cycle as the 3600 s delay between the beginning of the He8 and He10 cycles is not shown in the timing described.

Chapter 4

The EBEX Receiver: Operation

The operation of the EBEX receiver as well as the overall cryogenic, RF, optical, and spectral performance encompass multiple subsystems within the receiver. A discussion of the predicted performance in each of these categories follows.

4.1 Cryogenic Loading

To obtain an accurate model of the actual holdtime of the EBEX receiver, all the possible sources of loading on the thermal stages and cryogens must be accounted for. In order for EBEX to obtain its specified flight duration of > 10 days, the total loading needs to be below 24 W and 0.390 W for the LN and LHe stages, respectively, based on the roughly 130 L capacity of the LN and LHe receiver tanks. The three main sources of loads on the thermal stages are conducted, radiated, and generated power. Conductive loads come from wiring and other structures spanning between two or more different thermal stages. Radiated loads originate from warmer thermal stages or objects exterior to the receiver itself which radiate on the colder thermal stages. The two generated loads in the EBEX receiver are the SMB mechanism which through the dynamics of the system generates an additional load on the cryogenic stages, and the adsorption refrigerators which in their operation generate excess heat in order to obtain sub-Kelvin temperatures. The sub-Kelvin thermal stages require their own loading consideration and are discussed in Section 4.1.3.

4.1.1 Conductive Loading

Much of the conducted loads on the thermal stages originate from the structural design of the receiver, such as the G-10 structural supports of the thermal shells and the stainless steel tubing that passes through the warmer thermal stages to allow transferring of liquid cryogens into their respective tanks. Other conductive loads come from wiring for detector readout and other support electronics that pass between different thermal stages.

The detector wiring consists of 28 sets of 37 0.102 mm diameter Manganin wires that run from the receiver vacuum shell to the LHe stage. These wires are coupled to 14 pairs of 37-pin feedthrough connectors to connect to the remainder of the readout system at the vacuum interface. At the LHe stages, these wires are coupled to a female edge connector in which the SQUID amplifiers mount. Due to a maximum inductance contraint placed the detector readout wiring between the SQUID amplifiers in the LHe shell and the SQUID controller boards on the outside of the 300K shell, this wiring is only 150 mm long. The length of the wiring is 40, 35, 34, and 41 mm long from the VCS2, LN, VCS1, and LHe stages to the next warmest thermal stage, respectively. The detector wiring is embedded in a weave of Nomex [8] fiber which act as strain-relief for the thin wiring. The thermal characteristics of Manganin are well known [25] and some data on the thermal conductivity of Nomex can be found, however, the complex geometry of the weave and unknown fill factor makes calculations difficult and so measurements were made by collaborators at the University of California at Berkeley. The measurement found $A \int_{T_{4.2}}^{T_{30}} k(T) \, dT = 5.88 \times 10^{-3} \frac{\text{Wm}}{\text{K}}$, and assuming a roughly constant thermal conductivity supported by [8], the loading on the warmer stages can be calculated. Since the thermal conductivity is not constant and does increase slowly with temperature, this calculation will be an underestimate for higher temperatures. However, since these weave loading values are subdominant to the other wire loads at those temperatures, the final total wiring loading will not be greatly affected by this assumption.

Besides detector wiring, the EBEX receiver also has various support electronics, temperature monitors, and diagnostic sensors that require wiring between the thermal stages. This wiring consists of 196 0.127 mm diameter Manganin wires and 52 0.254 mm diameter Manganin wires with lengths of 50 mm between the VCS1, LN, VCS2,

and 300K stages and 100 mm between the LHe and VCS1 stages. The larger diameter wiring is used for high-current applications such as the operation of certain stages of the adsorption refrigerators and a mechanical heatswitch used during initial cooldown and final warmup of the receiver. The 248 non-detector wires are divided into 8 wiring assemblies with each assembly enveloped between two layers of Kapton HN tape that is 0.13 mm thick and 50 mm wide for wire organization and strain relief.

The SMB rotation system also has wiring mentioned in Section 3.4. A summary of the conductive loads from each of these wiring components and total wiring loading on each thermal stage is shown in Table 4.1.

Besides conductive power from wiring between the different thermal stages, the G-10 cylindrical supports for the receiver thermal shells and the stainless steel cryogen fill tubing that penetrate the thermal layers to the cryogen tanks also conduct power between the shells. These conductive loads were modeled by Brown University, and the values obtained from the modeling is shown in Table 4.2 along with the conductive load from the stainless steel foil used for RF shielding in the optics stack.

The SMB G-10 drive shaft extends from the 300 K vacuum shell to VCS1, where it is thermally sunk, and then with another G-10 shaft to the LHe shell. The first shaft is a rod of diameter 2.4 mm and length 113 mm and the second shaft is a tube of outer diameter 8.9 mm, inner diameter 8.0 mm, and length 23 mm. Using conductivity values from [39], this gives the HWP shaft load values in Table 4.2.

Stage	Detector Wire	Detector Weave	Other Wire	Wire Support	HWP	Total
VCS2	399	45	174	234	130	984
LN	386	53	184	158	100	881
VCS1	101	23	43	23	22	212
LHe	16	10	4	2	1	33

Table 4.1: Conductive loads from receiver wiring to various thermal stages. All loads are in mW.

Stage	G-10	LN$_2$ Fill	LHe Fill	SS Foil	Wiring	SMB Shaft	Total
VCS2	503	180	180	164	984	0	2011
LN	563	358	298	164	881	0	2264
VCS1	51	0	59	30	212	6	365
LHe	11	0	6	4	33	2	56

Table 4.2: Conductive loads sources in the receiver and total conductive load on the thermal shells. All loads are in mW.

4.1.2 Generative Loading

There are two sources of load on the LHe stage that depend on the operational mode of the receiver itself. These consists of the load from a rotating SMB system and the effective load from the cycling of the two adsorption fridges. These will be called the generative loads.

As mentioned in Section 3.4, the superconducting magnetic bearing has no conventional frictional dissipation, however, due to inhomogeneities in the azimuthal magnetic field of the permanent magnet in the rotor, hysteresis and eddy currents in metal components cause dissipative losses in the rotational motion that culminates in loads on the LHe stage. The physics of these losses is discussed further in [23], but they are predicted to be quadratically dependent on the rotational velocity of the SMB and have complex dependencies on the geometries of the magnetic field and surrounding metal objects.

While the SMB has no conventional frictional dissipation, the small ball-bearings used to support the drive and tensioner pulleys in the SMB system do dissipate frictionally. The small size of these bearings makes the frictional dissipation small, however, either through the friction in these bearings or through energy dissipated to deform the Kevlar belt used in the system, the rotor and AHWP warm above the 4.2 K bath temperature of the LHe stage. Since the belt is a poor thermal conductor and no other mechanical connection to the LHe bath exists, the rotor can only dissipate heat through radiative coupling to the LHe stage. This has been shown to raise the temperature of the rotor above 30 K which causes excess loading on the sub-Kelvin stages of the EBEX instrument as discussed below. The steady-state temperature of the rotor assembly also

is dependent on the speed of rotation of the SMB.

To determine the dissipative loads on the LHe stage from the SMB rotation, extensive testing was performed and measures were taken to reduce loading. This testing is discussed further in [23]. During the North American flight of EBEX and preceeding testing campaign, the SMB dissipated 39 mW of power with a 2.0 Hz rotation speed. During the testing phase after the flight, improvements in the implementation of the SMB resulted in a reduction in this dissipated loading by 46%, to 21 mW. This was reduced to 15 mW by slowing the rotation of the SMB to 1.5 Hz during the LDB flight. It should be noted that this dependence on the rotation speed is not quadratic, as predicted by either a hysteresis or eddy current model of power dissipation. This suggests a different mode of power dissipation, possibly through the small ball-bearings, vibrational motion in the tensioner pulley, or another unknown method.

The second generative loading method on the LHe stage comes from the cycling of the two adsorption fridges. The warming of the fridge pumps by applying currents to the pump heaters stores energy in the pumps, which is then deposited in the LHe bath when the heatswitches are closed and the pumps are again cooled to 4.2 K. The amount of energy energy applied to the pumps is well known since the resistance of the pump heaters is constant, the currents applied to the heaters are monitored during the cycling of the fridges, and the amount of time the currents are applied is governed by software running the fridge cycling process. A summary of these quantities are shown in Table 4.3.

The timing of the fridge cycles was optimized by minimizing the amount of time the pump heaters draw current while still keeping the pumps above 35 K when trying to condense liquid He.

The power dissipated by the heatswitch heaters is negligible due to their high resistance, 10 kΩ, and low current draw, 0.25 mA, despite drawing current for 10+ days. The total LHe evaporated due to the external application of power to the LHe stage is 7.578 L for both fridge cycles. The fridges are cycled every two days during ground testing and flight operations due to the 3.62, >3.82, and 3.56 day holdtimes of the He8 coldhead, interhead, and ultrahead stages, respectively, with no SMB rotation, and 2.0, >2.5, and 2.5 day holdtimes with SMB rotation. The true holdtime of the interhead stage was never determined since the expenditure of the ultrahead and He8 coldhead

Stage	R (Ω)	Time (s)	High I (mA)	Energy (J)	LHe used (L)
Pri	200	2706	97	5092	1.932
Sec	200	3370	87	5102	1.936
I4	200	2715	88.5	4253	1.614
I3	200	2405	90	3896	1.478
U3	400	2700	22	1630*	0.618*

Table 4.3: Duration of applied current, energy usage, and amount of LHe evaporate for each stage of the He8 and He10 fridge cycles. Note that the energy used in the U3 stage includes 9575 s with its low current setting of 17 mA. No other stages use the low current setting.

renders the cooling ability of the interhead inconsequential. Cycling both fridge every 2 days gives an effective load on the LHe stage of $\frac{19973 \text{ J}}{172800 \text{ s}} = 116$ mW.

4.1.3 Sub-Kelvin Loading

A major factor is the LHe stage holdtime is the LHe evaporated during fridge cycling and their holdtimes. The LHe evaporated is shown in Table 4.3, however the holdtime of the adsorption fridges and the ultimate temperatures of the He8 coldhead, interhead, and the ultrahead depend on the conductive and radiative loading on those sub-Kelvin thermal stages. The only generative loads on the sub-Kelvin stages are from temperature sensors such as RuO_2 which dissipate of order pW, and the relative-response stimular which dissipates of order 10 μW of power, but is operated for 30 s every 30 minutes, effectively making its loading 167 nW on the He8 coldhead.

As discussed in Section 3.8, the ultimate temperature of the sub-Kelvin stages depends on the loading on the stage. Measured load curves describing this dependence are shown in Figure 4.1.

The conductive loads on the three sub-Kelvin stages can be categorized into support structure, detector wiring, and RF tower conductances. The wiring to temperature sensors on the sub-Kelvin stages have estimated conductive loads of order 10 nW, and are considered negligible. The geometries of the optics box and focal plane supports
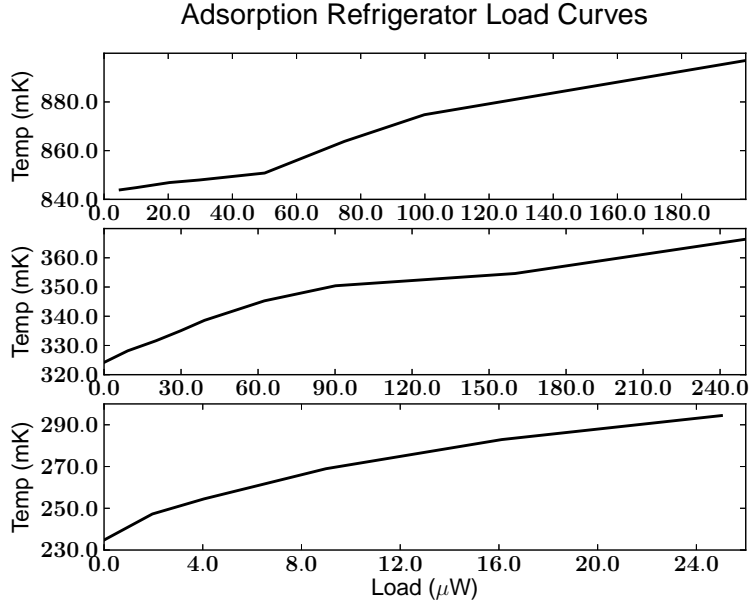
Figure 4.1: Stage temperature versus applied load, or load curve, for the three EBEX adsorption refrigerator stages, He8 coldhead (upper), He10 interheat (middle), and He10 ultrahead (lower). Data from S. Chase.

are discussed in Section 3.5,and of the RF tower and microstrips in Section 3.7. Using Vespel thermal conductivity values from Runyan et al.[40], Niobium thermal conductivity values values measured in 3.7, Kapton thermal conductivity values measured in [3], NbTi thermal conductivity values from Olson [31] and geometries listed in Table 4.4 conductance values can be calculated. Conductance for the support structures, RF tower, and microstrips are first calculated using a priori estimates of the sub-Kelvin stage temperatures of 1.5 K, 400 mK, and 300 mK for the He8 coldhead, interhead, and ultrahead, respectively.

These intial estimates show themselves to be inconsistent with the fridge load curves as the loads predicted, 191.8, 49.1, and 1.14 μW, put the He8, interhead, and ultrahead stages at 895, 320, and 235 mK. Using these new temperature estimates, we can recalculate the loads on the stages, Table 4.6, and find self-consistency between the load on the He8, interhead, and ultrahead stage. The predicted sub-Kelvin conductive loads and temperatures are 203.3, 15.9, and 0.65 μW, and 897, 330, and 240 mK for the He8 coldhead, interhead, and ultrahead stages. These agree closely with the

Element	#	Thickness	Size	Length CP→He8	Length He8→I	Length I→U
OB Sup.	4	3.59	38.1	299	-	-
FP Sup.	6	0.635	31.8	-	72	35.5
RF Tower Sup. H	2	1.27	31.8	101.6	17.1	16.1
RF Tower Sup. V	2	1.27	31.8	181.4	17.1	16.1
Nb Foil H	2	0.005	34.3	101.6	17.1	16.1
Nb Foil V	2	0.005	34.3	181.4	17.1	16.1
NbTi Wire H	112	0.033	0.762	144.5	27.8	17.1
NbTi Wire V	112	0.033	0.762	224.3	27.8	17.1
Kapton Tape H	28	0.064	15.2	144.0	27.8	17.1
Kapton Tape V	28	0.064	15.2	224.3	27.8	17.1

Table 4.4: Sub-Kelvin conductive load elements and geometries. Supports (sup) between the cold plate (CP) and He8 thermal stage are made of Vespel SP1; supports betwen all other stages, interheat (I) and ultrahead (U), are made of Vespel SP22. The size column shows either outer diameter of cylindrical elements, legs and foil, or width of flat elements, wire and tape. All distances are in millimeters.

observed steady-state temperatures of the interhead and ultrahead, 321 and 236 mK, however, the He8 coldhead stead-state temperature of 861 mK disagrees by 37 mK, which corresponds to load of 70 μW on the cold head. This difference of 133.3 μW in He8 loading could be explained by large contact thermal resistances of the Vespel SP1 support members to their mounts and between the different isolating segments of the RF tower assemblies since the supports and Niobium foil attached to the RF tower supports are the dominant loads on the stage.

Due to the finite thermal conductivity of the copper that thermally couples the fridge cold heads to optics box, focal planes, and thermal intercepts, temperature gradients are seen particulaly in the temperature of the focal planes. The steady-state ultrahead temperature is 236 mK, while the same temperature for focal plane H is 250 mK, and is 270 mK for focal plane V. For both focal planes, the copper straps have approximate

Element	He8 Load 1.5 K	I Load 400 mK	U Load 300 mK
OB/FP Sup.	94.0	8.05	0.32
RF Tower Sup.	17.2	11.25	0.23
Nb Foil	63.5	20.32	0.215
NbTi Wire	10.8	3.84	0.070
Kapton	6.4	5.66	0.30
Total	191.8	49.1	1.14

Table 4.5: Initial temperature estimates and the corresponding calculated conductive loads on the sub-Kelvin thermal stages. All loads are in μW.

$\frac{A}{l} = 1.8 \times 10^{-7}$ m, and using conductivities from [39] for OFHC copper, the temperatures of the focal planes are expected to be within 1 mK of the ultrahead temperature. The difference between these predicted and measured temperatures come from the contact resistances between the ultrahead, focal plane copper flange, and the copper straps that substantially reduce the effective conductance of the straps, similar to the conductances of the cold straps discussed in 3.8.

As indicated by the accuracy of the conductance-only estimates of the fridge stages temperatures, radiative loads on the interhead and ultrahead are negligible due to those stages seeing mainly the black interior of the optics box, which emits of order 40 nW. The interior surface of the LHe stage, also coated in Bock black, emits around 40 μW of power, which would be a notable load on the He8 coldhead, however, the optics box is covered in gold-plated aluminum shielding which reduces the emissivity of those surfaces below a couple percent and makes their contribution to fridge loading sub-dominant to conductive loads.

The one exterior surface of the optics box without gold plating is the top surface of the first pupil lens. Due to baffling immediate above the pupil lens, it is predominately radiatively loaded by the emission from the AHWP, which if settled at the 4.2 K bath temperature, would emit 2 nW onto the optics box. However, during SMB operation, the AHWP warms due to dissipative losses discussed in Section 3.4, obtaining a rotating

Element	He8 Load 895 mK	I Load 320 mK	U Load 235 mK
OB/FP Sup.	101.4	2.78	0.17
RF Tower Sup.	18.6	3.88	0.13
Nb Foil	65.4	5.71	0.11
NbTi Wire	11.1	1.12	0.036
Kapton	6.9	2.41	0.200
Total	203.3	15.9	0.65

Table 4.6: Final temperature estimates and the corresponding calculated conductive loads on the sub-Kelvin thermal stages. All loads are in μW.

steady-state temperature of 35 K, which would emit 500 μW of power onto the optics box and raise the He8 coldhead to 1.01 K. In order to reduce this load on the He8 stage, a duplicate LPE2b filter is installed immediately beneath the SMB before the optics box, which using the transmission values of LPE2b shown in 4.4, predicts a load of 3 μW on the optics box from the AHWP emission. In operation, the He8 coldhead reaches a steady-state temperature of 1.16 K during SMB operation. This temperature corresponds to a load of roughly 1400 μW from a linear extrapolation of the He8 load curve well beyond its measured loads, which gives little confidence in the value.

Since LPE2b has non-negligible absorptivity, the difference between the predicted and measured warm AHWP emissive loads is likely due to the filter itself warming and emitting power. Alternatively, the SMB mechanism could be causing dissipative loads in the optics box shielding similar to those noted in Section 3.4. The rotation of the SMB does not substantially affect the interhead, and ultrahead temperatures.

The sub-Kelvin stage holdtimes without SMB operation are measured to be 3.62, >3.82, and 3.56 days for the He8 coldhead, interhead, and ultrahead, respectively. The manufacturer of the He8 fridge reported a holdtime of 6 days, and a holdtime of 10 days for both the He10 stages, with no applied loads to the fridges, combining this

Stage	$L_{\mathrm{app},1}$	$t_{\mathrm{holdtime},1}$	$L_{\mathrm{app},2}$	$t_{\mathrm{holdtime},2}$	L_{para}
He8	70	3.62	0	6	106
Interhead	15.9	3.82	0	10	9.83
Ultrahead	0.29	3.56	0	10	0.16

Table 4.7: Applied loads, holdtimes, and calculated parasitic loads for the three fridge stages. All loads are in μW and holdtimes are in days.

information with our measured loads gives the constant parasitic load on the fridges,

$$Q = (L_{\mathrm{para}} + L_{\mathrm{app},1})t_{\mathrm{holdtime},1} \tag{4.1a}$$

$$Q = (L_{\mathrm{para}} + L_{\mathrm{app},2})t_{\mathrm{holdtime},2} \tag{4.1b}$$

$$L_{\mathrm{para}} = \frac{\frac{t_{\mathrm{holdtime},1}}{t_{\mathrm{holdtime},2}}L_{\mathrm{app},1} - L_{\mathrm{app},2}}{1 - \frac{t_{\mathrm{holdtime},1}}{t_{\mathrm{holdtime},2}}} \tag{4.1c}$$

Using the values from Table 4.7, yields parasitic loads of 106, 9.83, and 0.16 μW on the He8 coldhead, interhead, and ultrahead, respectively. The value for the interhead is a lower limit due to the incomplete holdtime measurement.

From these numbers and the fridge holdtime, we can calculate the total cooling energy that is contained in the He8 fridge, 55 J, and can predict the holdtime of the He8 fridge with SMB rotation, 0.4 days. The holdtime of the He8 fridge with SMB operation has been observed to be 2.0 days, which gives a method to better estimate the loading from the SMB using Equation 4.1 and yields a load of 142 μW. During flight operations, both fridges are cycled every two days to ensure proper stage temperatures for all components and thus minimize loading on the detectors.

4.1.4   Radiative Loading

The most difficult portion of the load on the thermal stages to predict is the radiative loading. Initial modeling of the EBEX receiver by Brown University predicted radiative loads of 15800, 8071, 63, and 0.8 mW on VCS2, LN, VCS1, and LHe stages. However, this model was performed without complete knowledge of the effect of the warm filters caused by non-zero absorptivity, and without knowledge of the final filter scheme used.

Further modeling of the filter power transmission was attempted, however, the finite absorptivity values of the filters and the effect of multiple reflections among the filters caused these models to greatly underestimate loading on the thermal stages. Thus an empirical approach to measuring and reducing the radiative loading on the stages was taken.

One method employed to reduce radiation loading of the thermal stages was to use multi-layer insulation on all shell surface area exposed to higher temperatures. Mulit-layer insulation, MLI, is alternating layers of thin conductive film with thin insulating film that is attached to a cold surface to reduce the effective absorptivity of the surface. The upper layers of the MLI thermalize to the temperature of the environment the MLI is exposed to, the warmer thermal shell in EBEX receiver, while the lower layers thermalize to the cold surface temperature. This forms a gradient of temperature through the layers of the MLI which reduces the radiative load on the colder surface by roughly Load $\propto N^{-1}$, where N is the number of layers.

For the receiver, 6 micron thick Mylar aluminized with 500 Å aluminum on both sides is used for the conductive film and 170 micron thick polyester netting is used for the insulating layers. MLI is installed around the top plate, bottom ring, bottom plate, side, optics stack side, LN fill port shell, and LHe fill port shell of all the cold thermal shells with 30 conductive/insulating layers on the VCS2 and LN shells, and only 20 layers on VCS1 and LHe due to the strong temperature dependence of radiative loading.

With this MLI scheme, the total load on the liquid cryogens with the window, LN optics stack, and LHe optics stack blanked off to reflect radiation was 15600 and 113 mW on the LN and LHe stages, respectively. This implies a radiative load from receiver internal components of 13300 and 57 mW on the LN and LHe stages, of which, the LHe radiative load is in great excess of initial modeling predictions. The loading on the vapor-cooled shields is difficult to measure due to the complex negative temperature feedback between the liquid cryogen stages. As liquid cryogen load increases, boiloff increases which increases cooling on the vapor-cooled shields, lowering its temperature and reducing loading on the liquid cryogen stage.

With the window and optics stack open to external radiation, the radiative loading situation depends on the filtering scheme used in the optics stack. Several iterations of
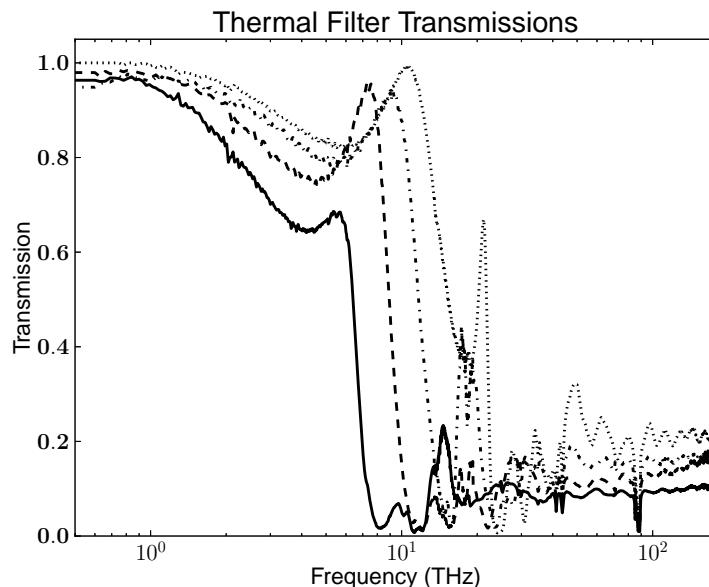
Figure 4.2: Measured thermal filter transmission curves for Thermal1 (dotted), Thermal2 (dash-dot), Thermal3 (dashed), and Thermal4 (solid) as provided from Cardiff University.

the number of and type of thermal filters used in the optics stack were tested. Four thermal filters types, labelled Thermal1 through Thermal4 with different high-frequency cutoffs, were used during this testing. The measured transmission curves for these filters are shown in Figure 4.2, and were measured by Cardiff University. The first thermal filter is mounted immediately beneath the window on the 300 K shell, the second filter is mounted in a filter mount at the top of the LN optics stack while another thermal filter is mounted below it in the later tests. The LN optics stack filter mount also contains a 12.7 mm thick Teflon absorptive filter that is thermal connected to the LN optics stack with copper straps at the edge of the filter, another thermal filter, and finally the first LPE (LPE1) filter. The LHe optics stack has a filter mount with first another thermal filter and then the second LPE (LPE2) filter. Inside the LHe optics stack is then the field lens, and NDF in ground operations, and then at the bottom of the LHe optics stack is the last LPE (LPE2b) filter. The filter and optical element ordering and mounting stages are also shown in Table 4.8. In order to accommodate the addition of a fifth thermal filter and absorptive filter to the optics stack, a 25 mm thick spacer ring

is installed between the optics stack top plate and 300 K optics stack cylinder to ensure elements mounted to the different thermal stages do not mechanically conflict or touch upon thermal contraction.

Filter Position	Stage	Filter Label	Cutoff (GHz)
Thermal I	300 K	Thermal1	60000
Thermal II	LN	Thermal2	30000
(Thermal III)	(LN)	Teflon	2000
Teflon	LN	Thermal3	15000
Thermal IV	LN	LPE1	750
LPE1	LN	Thermal4	12000
Thermal V	LHe	LPE2	600
LPE2	LHe	LPE2b	540
Field len	LHe		
(NDF)	(LHe)		
LPE2b	LHe		

Table 4.8: (Left) Position of filters and optical elements in the optics stack and mounting stages. Thermal filters in position I, II, III, IV, and V can be Thermal1 through Thermal4. Objects in parenthesis are present in some tests. (Right) Filter high-frequency cutoff values.

During several ground tests, the temperature of several optics stack objects was measured using SiD temperature sensors attached with rubber cement to the objects. Temperature sensors were never placed on thermal filters due to the risk of damage to the thin polypropylene. In particular, the Teflon filter temperature is a good indictor of LHe load performance. Teflon temperature and LHe loading of several receiver cold runs with different thermal filtering schemes are shown in Table 4.9.

The 4—4/3/3—4 thermal filter arrangement was used for all subsequent testing and for the LDB flight due to its minimum LHe load, see Figure 3.7 for a diagram of the final filter arrangement. The radiative load inferred from this configuration in Run 11 is 179 mW, with 122 mW of the load coming from the window of the receiver. This portion of

Run Number	Thermal Scheme (300 K)—(LN)—(LHe)	Teflon Temp. (K)	LHe Load (mW)
4	1—2/3—4	200	350
5	3—2/3—4	184	320
8	4—4/3/3—4	173	230*
9	4—3/2/3—4	190	270
11	4—4/3/3—4	140	235

Table 4.9: Thermal filtering scheme for several receiver runs with Teflon temperatures and LHe loads. The horizontal lines indicate the different stages that the thermal filters are mounted to. Run 8 was performed with a cold emissive load above the window with temperature during this measurement of 290 K and window temperature of 250 K.

the radiative load will be called the light load as it is the load present when the receiver is accepting light from the external environment. The other 113 mW load will be called the baseline load. Run 4 also measured the temperature of various other components in the optics stack, these values are shown in Table 4.10. Inferred temperatures for Run 11 with the optimal LHe load performance is shown as well.

The load on the LN stage remained relatively constant for this testing period with LN loads of approximately 15600 mW, giving a LN holdtime of 15 days.

Object	Run 4 Temperature (K)	Run 11 Temperature (K)
Teflon	200	140
LPE1	160	111
LPE2	100	69
Field Lens	20	14
LPE2b	15	10

Table 4.10: Measured Run 4 optics stack temperatures and Run 11 inferred temperatures. Run 11 temperatures calculated from measured Teflon temperature and assuming constant fractional power tranmittance to the next optical element, as $P \propto T^4$.

These measurements were performed during ground testing of the experiment and

include the emission from a thick, 12.7 mm, UHMWPE window, necessary for ground vacuum integrity. However, the DWM thin window was used during LDB flight operations in place of the 12.7 mm window. In order to estimate the reduction in load on the LHe stage from a thin window, the exterior environment of the receiver needs to be considered. The inner frame structure outside the receiver window is covered in a black, millimeter-wave absorptive material, Eccosorb HR, that is still largely absorptive at thermal frequencies [10]. The absorptive material reduces reflections to improve optical performance of the telescope. This material lines the area around the secondary mirror, receiver top, and aperture between the primary and secondary mirrors. This material is assumed to be perfectly emissive in the thermal regime and fills a solid angle not occupied by the secondary mirror as viewed by the receiver window, 2.44 sr, and is assumed to be thermalized to the gondola temperature, which we will take to be 300 K. The solid angle of the secondary mirror is presumed to reflect to the sky, and provide negligible LHe loading, the temperature is effectively 0 K. The actual inner frame and cryostat temperatures during flight drifted between 283 and 313 K as shown in Figure 6.3. The black environmental radiation will be partially absorbed by the UHMWPE thin window and then enter the filter chain.

In order to predict the LHe load with a thin window, a test that cannot be performed on the ground due to the pressure differential across the window, data from previous receiver runs, Table 4.9, was taken and analyzed. In particular, the light load from Run 5 is the measured LHe load less the baseline load, 207 mW, and the light load from Run 11, as mentioned, is 122 mW. The difference between the filter schemes in these two runs is the substitution of the initial Thermal3 and Thermal2 filters in Run 5 for two Thermal4 filters and a Thermal3 filter in Run 11. The light load from the black external environment and thick window emission that transmits to the Teflon filter between these two runs can be approximated given the filter transmission curves in Figure 4.2 and the absorption profile of UHMWPE, as provided from Cardiff University. This calculation yields 2671 mW of load incident on the Teflon filter in Run 5, and 745 mW in Run 11. Assuming a linear relationship between light load incident on the Teflon filter and measured LHe load, yields the relationship,

$$\text{LHe load} = 0.0441X + 89.1 \text{ mW} \qquad (4.2)$$

where X is the light load incident on the Teflon filter, in mW. It should be noted that even if the load on the Teflon filter goes to zero in this model, the LHe light load does follow. This stems from emission from the Teflon and other colder filters incident on the LHe stage. Improvements on the filtering of this emission would greatly affect the overall LHe light load, as this is the dominant portion of the light load.

The same calculation can then be performed for the thin window during flight, with thickness 1.0 mm. This thickness for the thin window was chosen to minimize the light load on LHe, and the emissive load on the detectors while remaining robust in the presence of flight-like pressure differentials. The flight filter configuration remained the same as in Run 11, so the only difference is the black environment radiation transmitted through the thin window and the window emission. This calculation yields a Teflon filter light load of 560 mW, which results in a predicted LHe light load of 114 mW for flight with the thin window.

The total expected flight LHe load is shown in Table 4.11. The effective load from the fridge cycling is complicated by the fact that in order to maximize LHe holdtime, both fridges were cycled prior to filling the liquid cryogenics prior to launch. Thus the first 2.0 days of flight would have no generative load from the fridges. This yields the relation between LHe holdtime, H, LHe load without fridge cycling, $L = 242$ mW, and LHe load from fridge cycling, $F = 116$ mW, and evaporative energy the 130 L of LHe, $V = 3950$ mW·days,

Load	Value (mW)
Baseline	113
SMB	15
Light	114
Total	242

Table 4.11: Predicted LDB flight LHe loads.

$$H = \frac{V + 2.0 \text{ days } F}{L + F} - 1 \text{ day} = 10.68 \text{ days} \tag{4.3}$$

where the day subtracted at the end is to account for the fact that the fridge cycle

loading occurs at the very beginning of the 2 day holdtime, rather than continuously over the entire duration.

4.2   RF Design
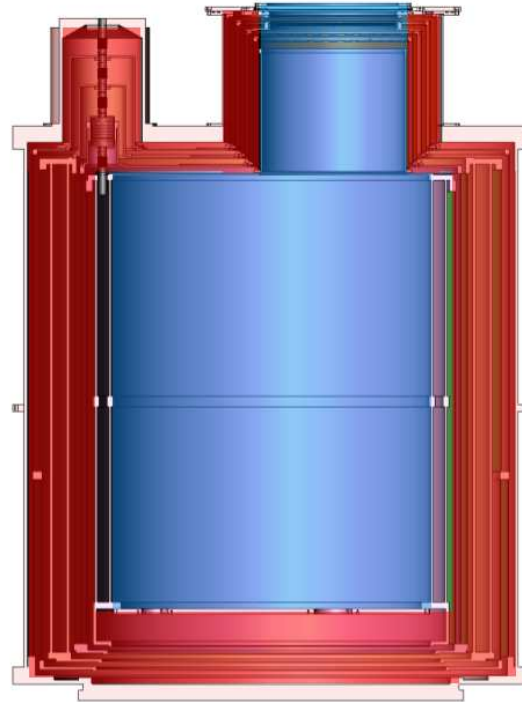
Figure 4.3: Separate RF cavity design for noise minimization. The RF "dirty" cavity is comprised of the interior optics stack and LHe instrument cavities, tinted blue, and the RF "clean" cavity is comprised of the inter-shell cavities and the LHe shell beneath the cold plate, tinted red.

The SQUID amplifiers used in the detector readout system require superconducting components and must operate are cryogenic temperatures, however, these amplifiers are very sensitive to both magnetic fields and radio-frequency (RF) noise. In order to minimize noise on the SQUIDs, a two-cavity system was designed with most components inside the receiver existing within the RF "dirty" environment that is open to the exterior electromagnetic environment through the window. The second cavity, the RF "clean" environment, is isolated within the receiver from the "dirty" environment

through use of the metal of receiver shells and RF shielding and filters at various location within the receiver. A diagram of the two-cavity RF scheme is shown in Figure 4.2. The RF "clean" environment is located between the exterior vacuum shell of the receiver and the 4K shell with the only exception being immediately beneath the window.

4.2.1 Optics Stack Shielding

The first RF shielding occurs at the optics stack, forming the RF-clean environment at the sides of the optics stack while leaving the light from the window to propogate further into the receiver. Stainless steel is used as a conductive barrier for the low-frequency radiation. Since attenuation through a conductive layer depends on the skin depth,

$$\delta_s = \sqrt{\frac{4\pi}{\mu\sigma\nu}} \tag{4.4}$$

where μ is the permability and σ is the electrical conductivity of the layer, and ν is the frequency of the incident radiation. The attenuation is then,

$$A(\text{dB}) = \frac{20}{\ln 10}\sqrt{\frac{\mu\sigma\nu}{4\pi}}t \tag{4.5}$$

which depends on the squareroot of the conductivity and linearly with the thickness of the layer, t. Since the shielding will have to extend between different thermal stages, thermal conduction would increase the loading on the colder stages, as described in Equation 3.2. For low temperatures, Wiedemann-Franz Law states,

$$\frac{k}{\sigma} = LT \tag{4.6}$$

with the constant Lorentz number, $L = 2.44 \times 10^{-8} \frac{\text{W}\Omega}{\text{K}^2}$. Assuming roughly constant thermal conductivity over temperature gives a linear relationship between conducted power and electrical conductivity. Also assuming a thin cylindrical layer with power conducting from the top to the bottom of the cylinder gives $A \approx 2\pi rt$. Thus conducted power over attenuation gives,

$$\frac{P}{A} \propto \sqrt{\sigma} \tag{4.7}$$

thus to minimize this quantity, a small electrical conductivity should be chosen.

The main concern for RF shielding the instrument inside the receiver is the NASA Scientific Instrumentation Package (SIP) attached to the bottom of the EBEX payload

used to communicate telemetry and scientific data to facilities on the ground. The SIP mainly communicates between 500 MHz and 4 GHz and so these frequencies were the main concern when designing the RF shielding for the receiver. A thickness of 0.0254 mm was chosen for the stainless steel foil due to the ease of shaping and handling of the material of this thickness, the sub-dominant loading caused by the thermal conduction along the foil compared to other loading sources, see Section 4.1.1, and the satisfactory rejection of the SIP communication frequencies. The geometry of the foil is shown in Table 3.3 and the thermal conduction values are shown in Table 4.2.

The foil is attached with silver-filled conductive epoxy to aluminum mounting rings at the top and bottom of the foil which are attached to the top-surface of the bottom of the colder-stage stack. The top mounting ring is attached to the bottom-surface of the top of the warmer-stage stack. This is done to maximize vertical length of the foil to minimize thermal conduction. This complicated the assembly procedure however, requiring the LHe stack installation and then the LHe-to-VCS1 foil assembly installation and then the VCS1 stack installation, and so forth. All metal-to-metal joints include rings of indium wire compressed between the two metal surfaces to ensure the RF integrity of the RF-clean environment.

The attenuation of the foil between 500 MHz and 4 GHz varies from -11.4 to -32.3 dB, respectively. The low-attenuation at low frequencies is compensated for by the rejection of large wavelengths by the entrance aperture of the window and overall geometry of the optics stack itself.

4.2.2   RF Towers

The focal plane waveguide arrays reject low frequency radiation by use of the circular waveguides that define the low-frequency edge of the EBEX frequency bands, see Section 4.4. The waveguides strongly reject low frequency radiation from entering the focal planes and establish an RF free environment inside the focal planes that is then enclosed by a metal shell with indium wire compressed between metal-to-metal joints to ensure a continuous conductive layer.

The RF towers ensure RF integrity in both the focal planes and SQUID cavity by mounting to both with indium wire at the joints and with a continuous conductive layer around the outside of the RF towers. This is accomplished with 5 micron thick

niobium foil that superconducts beneath 9.2 K that is formed into cylinders around the Vespel tubes of the RF tower. The ends of the Nb foil are electrically connected to the aluminum flanges at the ends of each isolated segment by silver-filled conductive epoxy.

4.2.3 Cold Plate Interface

In order to attach the fridge cold straps to the cold plugs during the instrument assembly, two 64 mm diameter through holes, called "manholes," in the cold plate allow manipulation of the ends of the cold straps and the bolting of their copper flanges to the plugs. These manholes are then covered by 6.4 mm thick aluminum plates, but to facilitate the removal of air from the SQUID cavity beneath the cold plate during evacuation stage of receiver operation, the plates have 25 1.6 mm diameter holes through them. These holes act as waveguides with $\nu_C = 231$ GHz and have 267 dB rejection of 2 GHz radiation.

4.3 Optics

The EBEX telescope is a Gregorian-type telescope designed to produce a 8 arcminute Gaussian beam full-width half-max, FWHM, per detector with a 6° total field of view for the focal planes that is diffraction limited in its resolution. A design requirement was the inclusion of a cold Lyot stop for placement of the AHWP to ensure full illumination of the AHWP for each detector to avoid AHWP surface irregularities from causing systematic effects across the focal plane. The optics is also designed to be fast, $f/1.9$, in order to reduce the physical size of the telescope and minimize weight.

4.3.1 Optical Design

The EBEX telescope consists of warm optical and cold optical elements. The warm optical elements are comprised of a parabolic primary mirror and an ellipsoidal secondary mirror both consisting of an aluminum optical surface accurate to 0.05 mm, which translates to $\frac{\lambda}{14}$ for the 410 GHz band, and a ribbed aluminum backing structure to provide rigidity and minimize overall weight of the mirrors. The primary mirror has a footprint diameter of about 1.5 m and the secondary has a diameter of 1.2 m, and both

are mounted to the EBEX inner frame via adjustable hexapod tables to allow optical alignment.
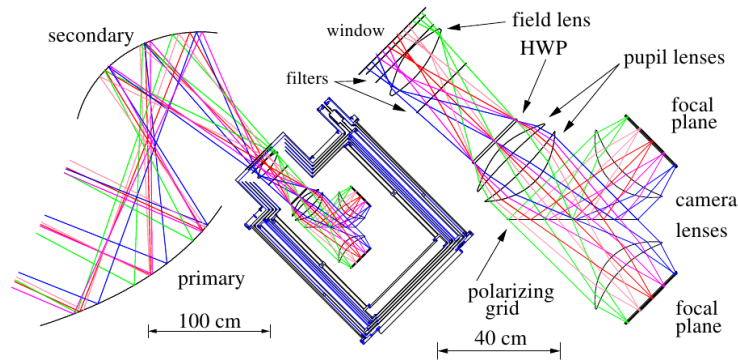
(a) EBEX telescope design.
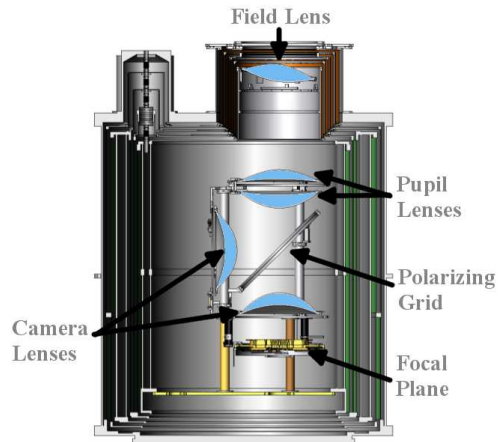
(b) Receiver cold optics and positions.

Figure 4.4: EBEX optical design, and cold optics system.

The cold optical system consists of an absorptive aperture stop, polarizing grid, conical horn couplers, and five UHMWPE lenses mounted within the receiver, see Figure 4.4(b). UHMWPE was chosen as the material for the lenses due to its optical properties (index of refraction and absorptivity in the EBEX bands), machinability, and the availability of broadband anti-reflective coating technology from Cardiff University for this material. All the lenses are coated with porous Teflon sheets, refractive index of 1.3, 0.2 mm on the sky-side and 0.4mm on the detector-side of the lenses in order to reduce

reflections. See [30] for a further discussion of the optical parameters and optimization of the EBEX telescope.

The field lens is mounted via an adjustable stage to in the middle of the LHe optics stack, at the focus of the warm mirror system, and operates at about 9 K. The field lens axis is tilted at an angle of 8.11° relative to the cylindrical axis of the receiver, and also the telescope optical axis both before and after the lens, in order to correct for the angled focal plane from the mirror system. The field lens is of critical importance to the polarization properties of the EBEX receiver due to its placement prior to the rotating AHWP, thus any linear polarization signal induced by the field lens will be modulated similarly to that of signals from the sky.

The next cold optical element is the absorptive aperture stop which defines the extent of the optical system and the area on the primary mirror that focal planes can view. The stop is formed by annular plate of Eccosorb with a sharp circular inner edge mounted at the top of the optics box and has a temperature of about 1.2 K during SMB operation. The AHWP lies just above the aperture stop so that each detector views the entirety of the AHWP surface to mitigate any effects from inhomogeneities in the sapphire or anti-reflective coating.

The two pupil lenses are mounted together to an adjustable stage beneath the aperture stop. The lenses are accurately aligned to each other through tight machine tolerances of the relative mounting structure between them. The polarizing grid is mounted at an angle of 45° beneath the pupil lenses and the two camera lenses are mounted along the transmission and reflection directions of the grid. The camera lens for the H focal plane is mounted via adjustable stage to the base plate of the optics box and the camera lens for the V focal plane is mounted via adjustable stage to a vertical mounting ring. The H focal plane is mounted rigidly to the optics box base plate in a horizontal position and the V focal plane is mounted to the mounting ring in a vertical position.

The 410 GHz detectors are mounted in the central portions of the focal planes due to its maximal Strehl ratio and the relatively quick falloff of the Strehl ratio further from the center of the focal plane at 410 GHz. Strehl ratios above 0.85 extend to the edge of the focal planes for 150 and 250 GHz. The 250 GHz are mounted furthest from the receiver plane of symmetry due to deformation in the lenses discussed below.

The horn arrays couple the Gaussian optical beam formed from the rest of the optical
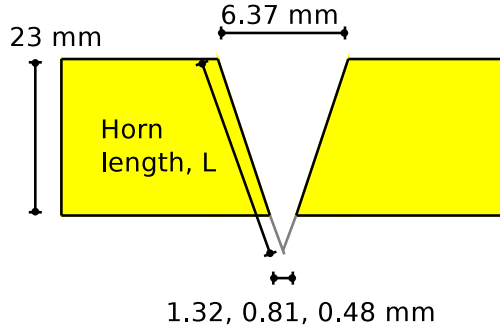
(a) Generalized horn geometry.
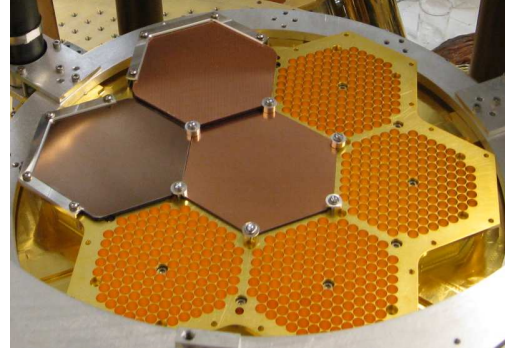
(b) Partially-filtered horn array.

Figure 4.5: Diagram of feedhorn geometry and image of a horn array. The small diameter opening of the horn arrays is determined by the frequency band, 1.32, 0.81, and 0.48 mm for the 150, 250, 410 GHz bands, respectively.

system to the waveguides and detectors beneath the arrays. Horns have generalized geometry as shown in Figure 4.5. The small diameter of the horn is set by the low-frequency cutoff of the waveguides beneath, and the large diameter has a maximum value given a close-packed spacing of the circular opening of the horns and spacing of the detectors on the silicon wafers. The size of the primary mirror's optical surface, $D = 1.05$ m, sets the diffraction limited angular size,

$$\Theta = \frac{1.22\lambda}{D} \tag{4.8}$$

which is 8 arcmin. Spacing the detectors closer than this would oversample the sky and so detectors are spaced 11.5 arcminutes apart, 6.626 mm, which sets the large diameter of the horns to be 6.37 mm to allow for fabrication. The only free parameter in the horn design is the length of the horn, L. From King [22], a large dropoff in absolute gain occurs for horns shorter than the optimal length/wavelength, but a far shallower dropoff occurs for longer horns. To ease fabrication, the horn array is the same thickness for each frequency band, thus the horn length was set by the 410 GHz band to be 25.1 mm, giving this band maximal absolute gain, and the 150 and 250 GHz bands acceptable gains, and setting the horn array thickness to be 23 mm.

4.3.2 Deformations

The EBEX optical system calls for the use of a system of five large-diameter (350 mm) lenses to be used at cryogenic temperatures. These lenses are made from a single slab of UHMWPE to ensure a homogeneous index of refraction of 1.5182 among all the lenses. The deviation of the lens surfaces from the ideal surfaces can affect the optical performance of the telescope. In addition, the process used to adhere AR-coats to the lens surfaces involve applying a pressure differential across the lens that could further deform the shape of the lens.

The lenses were fabricated using a lathe to ensure symmetry and measured using a coordinate-measuring machine (CMM) along each surface of each lens. This was performed several times between various numbers of cryogenic cycles and pre and post anti-reflective coating. Lens characterization was performed by offsetting the CMM data to account for the CMM ball radius and AR-coat thickness, when applicable, and adjusting the data to account for any inherent offset or angle in the measuring process. These numbers were then compared to the analytical prediction and deviations from ideal were calculated. Initially, the deviations were small, and RMS values were generated to characterize the overall distortion of the lenses.

The different measurements of RMS deviations from ideal are listed in Table 4.12. Measurement 1 was made January 2008 after initial fabrication of the first four lenses (without the camera lens for focal plane V); measurement 2 was made October 2008 after the first thermal cycling of the lenses in the receiver; measurement 3 was made September 2009 after about 10 thermal cycles in the receiver; and measurement 4 was made February 2010 after the lenses were AR-coated.

After the AR-coating process lenses showed RMS deviation several times larger than the pre-AR-coating lens measurements. Mapping the deviations, Figure 4.6 as an example, shows a large increase in magnitude of deviation with increasing radius for each of the lenses. When compared to the deviation prior to the AR-coating, the AR-coating process becomes the main candidate for producing these large deviations.

To characterize these deviations, an even-polynomial fit was performed on the deviation data with $r \to |r|$, in order to ensure even-ness of fit. This polynomial fit was chosen in order to be easily implemented in the program CodeV for analysis.

Lens	Surface	RMS deviation from ideal (mm)			
		Measure 1	Measure 2	Measure 3	Measure 4
Field	Top	0.043	0.018		0.147
	Bottom	0.020			0.053
Pupil1	Top	0.076	0.025	0.122	0.605
	Bottom	0.056			0.513
Pupil2	Top	0.069	0.076	0.097	0.605
	Bottom	0.119			0.368
Camera H	Top	0.043	0.046	0.102	0.465
	Bottom	0.020			0.424
Camera V	Top			0.178	0.193
	Bottom			0.127	0.178

Table 4.12: UHMWPE Lens deviations from ideal surfaces.

The effects of these deformations were then analyzed using the Strehl ratio formalism, as computed by the CodeV wavefront error analysis tool. Nominally EBEX is designed to provide all bolometers with imaging performance above 0.85 Strehl, where 1.0 Strehl corresponds to the performance of an ideal diffraction-limited system. Some bolometers near the edge of the focal planes see worse performance in the designed system, but they are not intended to be used for map making. The deviated lens systems showed minor improvement of Strehl ratios for the 410 GHz band near the focal plane center, and position and radius dependent Strehl reduction for the all three bands away from the center. In general, Strehl ratios decreased away from the focal plane center, with very little decrease perpendicular to the symmetry plane of the receiver, and a large decrease along the plane, with a larger effect with higher frequency, see Figure 4.7. The change in Strehl is of order 0.07. To minimize the reduction in Strehl ratio for the 250 GHz band, the 250 GHz wafers are located in the position furtherest from the symmetry plane.
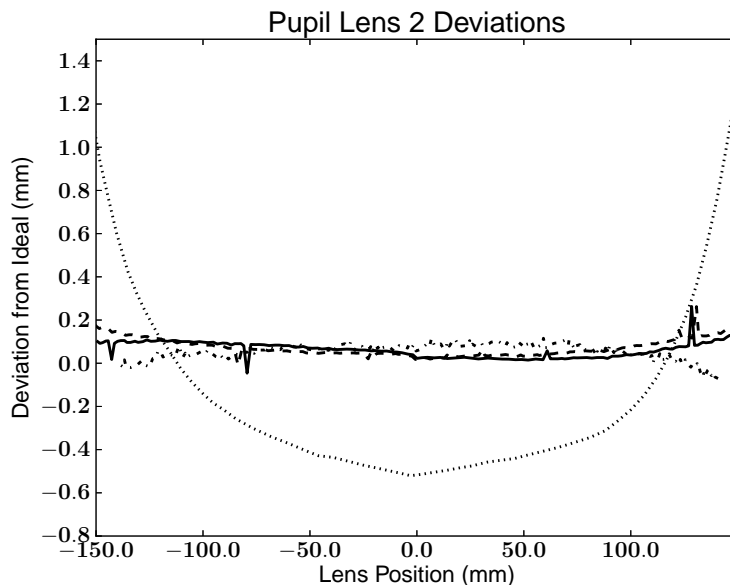
Figure 4.6: Pupil lens 2 deformation from ideal surface along a single linear profile as measured after fabrication (solid), after a single thermal cycle (dashed), after 10+ thermal cycles (dot-dash), and after AR-coating process (dotted).

4.3.3 Alignment

The multiple optical elements of the EBEX telescope require precise alignment to be diffraction limited. Using the tolerancing function in Zemax with the EBEX optics, it was determined that the system will remain diffraction limited with 90% probability with the alignment tolerances listed in Table 4.13.

	Position (mm)	Angle (°)	Thickness (mm)
Cold Optics	±0.13	±0.1	±0.13
Warm Optics	±0.25	±0.1	

Table 4.13: EBEX optical system alignment tolerances.

The mirrors, lenses, and polarizing grid are mounted on adjustable position hardware that allow a dynamic range of movement of 25 mm and 3° for the warm elements and 3 mm and 1° for the cold elements in lateral and rotational position. Due to the constraints
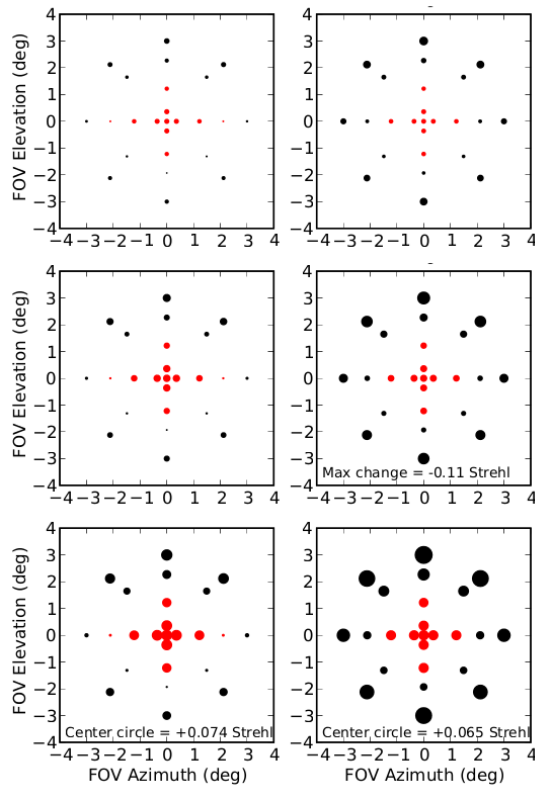
Figure 4.7: A simulation of the change in optical performance between deformed and non-deformed cold optics for 150 (top), 250 (middle) and 410 (bottom) GHz bands. Black (red) circle size indicates size of reduction (increase) in Strehl ratio at that focal plane position. Left graphs are for focal plane H and right graphs are for focal plane V. Figure from M. Milligan.

of the RF towers and thermal isolation, the focal planes are the fixed elements that set the alignment for the rest of the optical system. The optical elements are aligned through the use of an approximately 1 m dynamic range CMM and adjustable length inside micrometers with ranges up to 2500 mm. These devices measure the distance between high-precision tooling balls mounted to the optical elements at known positions. For the cold optics, the 3-D modeling program Rhino is used to take the CMM data of the tooling ball positions and then model the cold element position relative to the other elements. The elements can then be adjusted until the relative position matches the target values within the tolerances listed in Table 4.13. For the warm elements and

warm to cold alignment, the target relative distances betwen tooling balls is known and the mirror hexapod mounts are adjusted until the measurements are within tolerance of the targets.

The thermal contraction of the receiver and interior elements must be considered when setting alignment target values. In particular, the focal plane to camera lens top distance is affected by the contraction of aluminum, Vespel SP22, and UHMWPE, which changes the relative distance between them by 2.3 mm. To calculate the target values between the tooling balls, the ideal cold optics separations at 4.2 K, given from the optical design, is reduced by the 4.2 K contracted lengths of the non-aluminum components such as UHMWPE and Vespel in the path between the elements. The remaining length is 4.2 K aluminum, and then this aluminum length and the non-aluminum component lengths can be de-contracted back to 300 K to find the target numbers. Additional length is added to the target numbers for tooling ball shoulder distances and any other measurement-only distances. This procedure is repeated for each relative distance for the cold optical system. The 45° angle of the polarizing grid is similarly adjusted with the angle aligned with the fixed position of the V focal plane.

Due to their fixed positions, the central normal axes of the focal planes do not intersect within alignment tolerances. This is considered acceptable because lateral shifts of the physical focal plane center relative to the ideal center defined by the chief ray of the optical system merely changes the angular pointing of the detectors without diminishing optical performance, given the scale of shifts observed.

The field lens requires a non-concentric alignment to the rest of the cold optics due to the 8.11° tilt of the lens. A vertical and lateral target is calculated given this tilt. The field lens position is then measured relative to tooling ball at the top of the receiver optics stack, and these allow alignment of the cold field lens to the telescope mirrors after the receiver has been closed and cooled.

Target distances between the optics stack tooling balls and secondary mirror hexapod tooling ball are generated, given the known geometry of the hexapod tooling ball relative to the mirror surface and the known transfer between optics stack tooling balls and cold field lens position. The secondary mirror hexapod is aligned using inside micrometer measurements between optics stack and hexapod tooling ball combinations and adjustment of the six hexapod legs. Then the primary mirror hexapod is aligned to the

new position of the secondary mirror hexapod in a similar method. Once the alignment is completed, mirrors are mounted on the hexapod supports and tooling ball location on the edges of the mirrors are measured relative to each other to verify alignment.

4.4 Relative Spectral Response

The EBEX instrument defines the measurement frequency bands by use of several low-frequency pass edge (LPE) filters and the use of circular waveguides that act as high-frequency pass filters. The combination of these elements roughly set the spectral response of the EBEX receiver, however, other elements in the optical path of light from the sky also influence the response. The elements that affect the spectral response of the EBEX instrument, are from warmest to coldest element, the thick/thin UHMWPE window, thermal filters, Teflon filter, LPE filters, UHMWPE lenses, NDF, AHWP, and waveguides. Reflection from mismatched indeces of reflections are ignored as this would cause a broadband reduction in transmittance rather than a relative change in response across the bands, assuming small in-band index of refraction changes. Warm optics spectral response is predicted to be flat due to the pure reflective nature of the mirrors and is ignored.

The thermal and LPE filter transmission curves are shown in Figure 4.2 and Figure 4.8, respectively, and were measured by Cardiff University. To determine the transmission curve through the lenses, an effective UHMWPE thickness was determined by finding the effective thickness for each lens. This was determined by weighting the thickness at some radius from the central axis of the lens by the surface area at that particular radius and averaging over the lens. This lead to effective thicknesses of 32.4, 17.3, 27.9, and 23.4 mm for the field, pupil 1, pupil 2, and camera lenses. Using the absorption coefficient curve of UHMWPE provided by Cardiff University, the transmission of the lenses and window can be determined.

Using optical constants for Teflon from [26] and measured AHWP data from Cardiff, the transmission curves for the thick window, lenses, Teflon filter, and AHWP are shown in Figure 4.9. The transmission curves from Figures 4.2, 4.8, and 4.9 comprise the common elements to the three frequency bands in EBEX and the common transmission curve is shown in Figure 4.10. To find individual band spectral responses, the common
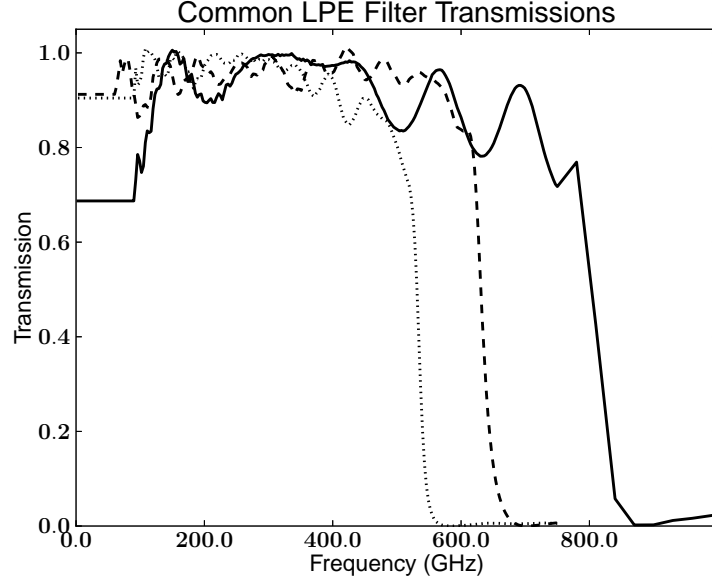
Figure 4.8: Transmission profiles for LPE1 (solid), LPE2 (dashed), and LPE2b (dotted) as provided from Cardiff University.

transmission data needs to combined with the band specific elements.

The first band specific element is the NDF as the thickness is tailored for each frequency band. To determine the transmission through the NDF, first a measured value of the complex index of refraction of $n = 1.93 + 0.037i$ at 1.2 K from Peterson [34] was used to calculate $\tan \delta = 0.038$ using,

$$\tilde{n} = n + i\kappa \tag{4.9a}$$

$$\tilde{\epsilon} = \epsilon' + i\epsilon'' = \tilde{n}^2 \tag{4.9b}$$

$$\epsilon' = n^2 - \kappa^2 \tag{4.9c}$$

$$\epsilon'' = 2n\kappa \tag{4.9d}$$

$$\tan \delta = \frac{\epsilon'' + \frac{\sigma}{\omega\epsilon_0}}{\epsilon'} \tag{4.10a}$$

$$\tan \delta \approx \frac{2n\kappa}{n^2 - \kappa^2} \tag{4.10b}$$
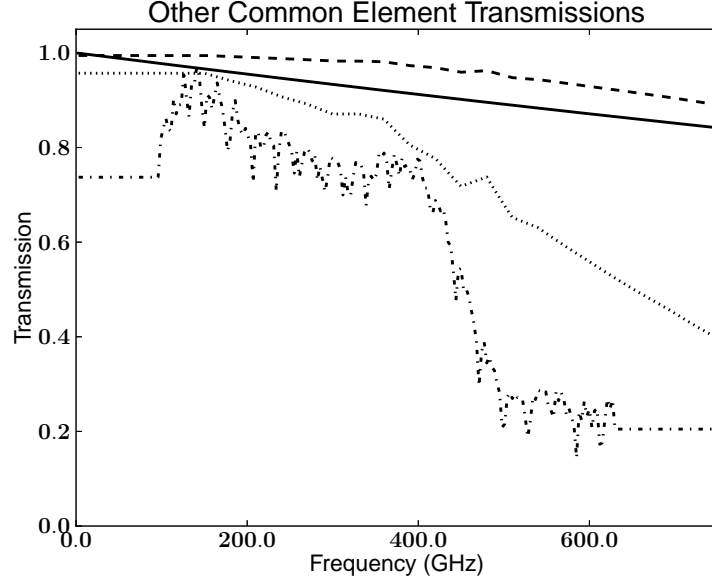
Figure 4.9: Transmission profiles for the Teflon filter (solid), thick UHMWPE window (dashed), AHWP (dash-dot), and thickness-averaged UHMWPE lenses (dotted). AHWP transmission curve provided from Cardiff University.

in the small conductivity, σ, limit for complex relative permittivity, $\tilde{\epsilon}$. Using,

$$P_{out} = P_{in}e^{-\frac{2\pi}{c}n\nu\tan\delta z} \tag{4.11}$$

for the transmitted power through a lossy material of thickness z and index n at frequency ν. The measured thicknesses of the 150, 250, and 410 GHz portions of the NDF and corresponding average transmissions are listed in Table 4.14. The predicted NDF spectral responses for frequency band f will be denoted $p_{\mathrm{NDF},f}(\nu_i)$.

Above each wafer on the either focal plane is a set of two LPE filters that finalize the low-pass edge of the frequency band. Two different LPE filters, a "blocker" and an "edge," are used to minimize power leakage through overlapping high-frequency features in the transmission curves. The total transmission curves for these sets of filters for each band are shown in Figure 4.11. Circular waveguides are used to define the low-frequency
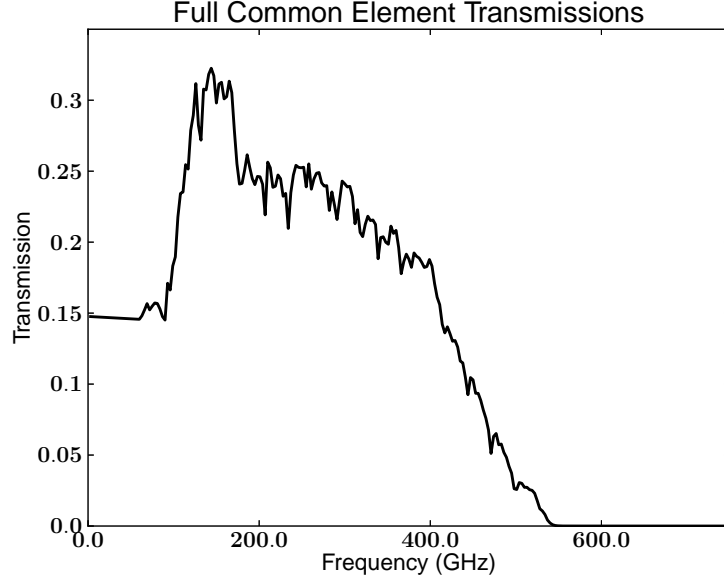
Figure 4.10: Transmission profile for all band-common elements.

edge of the bands since attenuation through a waveguide is,

$$\nu_c = \frac{1.841c}{2\pi r} \tag{4.12a}$$

$$P_{\text{trans}} = P_I e^{-\frac{4\pi}{c}\sqrt{\nu_c^2 - \nu^2}z} \tag{4.12b}$$

for waveguide of radius r and length z. Above the critical frequency ν_c, waveguides allow propogation of the wave, but below the critical frequency large fractions of the power are reflected. The waveguides in the waveguide array have radii of 0.660, 0.407, and 0.242 mm to define the critical frequencies to be 133, 216, and 364 GHz for the 150, 250, and 410 GHz bands, respectively. The total predicted spectral responses of the three frequency bands are shown in Figure 4.11, and will be referred to as $p_{\text{Ground},f}(\nu_i)$, for frequency band f, and the predicted spectral responses without the NDF response included will be referred to as $p_{\text{Flight},f}(\nu_i) = \frac{p_{\text{Ground},f}(\nu_i)}{p_{\text{NDF},f}(\nu_i)}$.

Band	Thickness	Transmission
150	18.3	0.014
250	10.8	0.015
410	6.6	0.015

Table 4.14: NDF thicknesses, in millimeters, for each of the EBEX frequency bands, in GHz, and corresponding transmissions.

Figure 4.11: (Upper) Transmission profiles for "blocker" (dashed) and "edge" (solid) LPE band-defining filters as provided from Cardiff University, with waveguide response (dotted) for the three frequency bands, 150 (left), 250 (middle), and 410 GHz (right). (Middle) NDF transmission profiles for the three frequency bands. (Lower) Total predicted transmission for the three frequency bands.
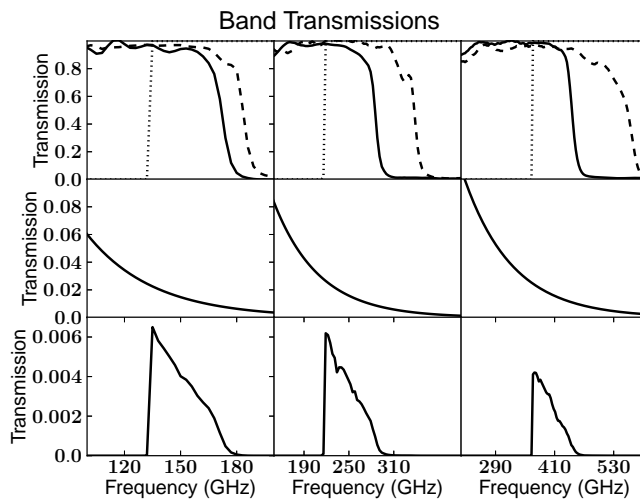
Chapter 5

Calibration

5.1 Relative Spectral Response

The EBEX receiver relative spectral response was first measured prior to the North American flight in New Mexico during April 2009 [36]. Further testing was performed in June 2011, however, changes in the band defining filters in the receiver and the need for more accurate response data led to further testing in June and July 2012 in Palestine, TX, prior to EBEX compatibility testing with NASA flight hardware.

Accurate relative spectral response measurements of the EBEX receiver are required to specify the effective band centers and band widths of the three EBEX frequency bands. When combined with the absolute band optical efficiency measurements, the spectral response determines how much power from the sky is detected and at what frequency, on average. This is necessary to accurately model the galactic foreground signals, primarily composed of polarized dust emission, predicted to dominate in the 250 and 410 GHz bands. These foreground signals can then be extrapolated to the 150 GHz band and removed to leave the sub-dominant cosmological signals in the 150 GHz band, see Figure 2.1.

Also of importance to the ultimate science goals of EBEX is the frequency-dependent polarization rotation stemming from the AHWP. Due to the broadband application of the AHWP, the polarization rotation of the output polarization angle is not constant with frequency and must be accounted for to obtain accurate Q/U Stokes parameters

and thus E/B for any signals measured by the instrument. The average frequency-dependent polarization rotation across each of the three frequency bands then needs to incorporate the relative spectral response of the receiver itself. The frequency-dependent polarization rotation calibration is discussed in [23].

The effective band center and band width accuracies needed for measurement of the tensor-to-scale ratio $r = 0.01$ are listed in Table 5.1.

Band (GHz)	Required ν_{center} error (GHz)	Required $\Delta\nu$ error (GHz)
150	1	0.8
250	9	2.0
410	20	14

Table 5.1: Spectral response band measurement requirements from [2].

5.1.1   Measurement

The primary spectral response measurements were carried out in June and July 2012 in the Columbia Scientific Balloon Facility (CSBF) in Palestine, TX. In order to measure the spectral response, monochromatic light of known wavelength must be measured by the EBEX detector arrays and the frequency of the light must be controllably varied to scan across the three EBEX frequency bands. This was accomplished by the construction of an Ebert-Fastie monochrometer designed to work in the millimeter-wave regime and couple to the receiver cold optical system.

The Ebert-Fastie (EF) design was first developed for infrared spectroscopy in 1952 [12][13], and benefits from the use of a single reflector for both collimation and focusing of the monochromatic beam. The monochrometer uses a diffraction grating, governed by the grating equation,

$$m\lambda = d(\sin\alpha + \sin\beta) \tag{5.1}$$

where α and β are the incident and reflected angles off the grating relative to the grating normal, m is the diffraction order, and d is the grating groove spacing. The EBEX EF design is shown in Figure 5.1 and operates using $m = 2$ and three diffraction gratings of spacing 4.0, 2.4, and 1.5 mm for the 150, 250, and 410 GHz bands. In order for light to
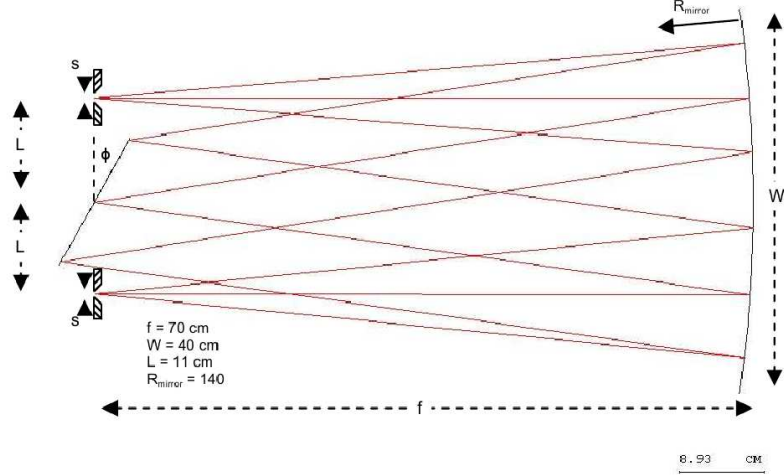
Figure 5.1: Ebert-Fastie optical design for EBEX operation, see [36].

pass through the exit and entrance apertures of the EF, $\beta - \alpha = 2\theta = 17.861°$ for the EBEX design, and by geometry, $\beta - \phi = \theta$, where ϕ is the angle of the grating relative to the aperture plate. This leads to the relation between the grating angle, ϕ, and the output frequency,

$$\nu = \frac{mc}{2d\cos\theta\sin\phi} \tag{5.2}$$

By knowing the angle of the diffraction grating, the wavelength of the light exiting the EF is known and spectral analysis of the light source can be made. The dispersion of the light within the EF is set by the entrance and exit apertures of the light entering and exiting the device and, in practice, produces a range of wavelengths at the output of the EF. In theory, monochromatic light can be output with aperture sizes approaching zero, however, this is at the expense of output power from the device. The width of the frequency output comes from differentiation of Equation 5.2 with respect to β, the angle from the diffraction grating to the exit aperture, and is described by,

$$\Delta\nu = \frac{mc\cos(\phi + \theta)}{(2\sin\phi\cos\theta)^2}\frac{\Delta x}{L_B d} \tag{5.3}$$

where $\Delta x = 12$ mm is the exit aperture width and $L_B = 700$ mm is the mirror focal length. Although not truly monochromatic, the light exiting the EF is sufficiently narrow-band that it will still be reference to as monochromatic, and the EF as
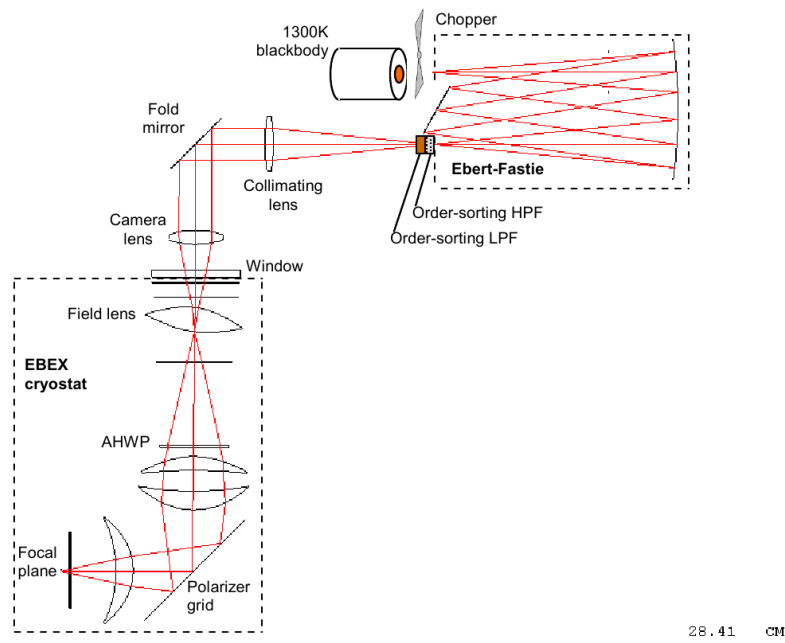
Figure 5.2: Full optical design of the EF device coupling to the EBEX receiver.

a monochrometer. Equation 5.2 describes the central frequency of the EF output.

Alternatively, a known input light source can be used with the EF to produce monochromatic light of known wavelength for measuring spectral response. The EF was operated in this manner for the EBEX spectral response measurement with a 1400 K laboratory blackbody source producing the input light. The temperature of the blackbody source is measured to be stable to a few K in several hours. The relative response measurement is independent of the precise blackbody temperature since the response will be normalize to maximum signal in the analysis process and the measured frequencies are in the Rayleigh-Jeans limit of the blackbody spectrum for the temperatures used. The Ebert-Fastie design was chosen for EBEX for its relatively simple design, which facilitates the setup procedure, ability to rapidly assess spectral characteristics during measurements, and relatively small size and mass which allows for easier manipulation and placement of the monochrometer.

The output beam from the EF is coupled to the acceptance beam of the receiver cold optics by use of two UHMWPE biconvex lenses and a 90° fold mirror, Figure 5.2. These

Figure 5.3: EF device with X/Y-translation stage used for receiver-only calibration measurements.

lens were designed using Code V to match the $A\Omega$ of the cold optics and maximize signal couping to a single detector. This requires alignment of the EF and lens system to the receiver cold optics in order to measure spectral response in a given detector. See [36] for a further discussion of the Ebert-Fastie design and motivations. Alignment of the EF internal and external optics was performed similarly as the cold optics alignment for the receiver, see 4.3.3.

The initial design of the EF device consisted of mounting the mirror, diffraction grating, and apertures on an optical bench and enclosing the structure within Eccosorb-lined metal shielding. However, due to the necessary coupling of the EF optics with the receiver, this design proved difficult to align due to its weight and rigidity. A new design emphasizing low-weight and translational alignment capability was constructed that consists of aluminum box-beam framing attached to an aperture base plate. Also mounted to the base plate is the diffraction grating rotation mechanism with attached stepper motor, with 40:1 gearbox reducer to increase angular control, and a $0.011°$ absoluted rotary encoder attached directly to the grating rotating shaft.

The blackbody is mounted on the side of the EF enclosure and the output light is channeled with a polished brass lightpipe to an optical chopper rotating at either 3.0 or 13.0 Hz before encountering the entrance aperture of the EF. The blackbody was placed at this location rather than direction in front of the entrance aperture to facilitate

possible mounting of the EF to a Cassegrain telescope to simulate far-field incident light. Order-sorting filters, consisting of LPE filters similar to those used inside the receiver and a waveguide plate, are mounted to the exterior side of the exit aperture of the EF to eliminate non-2nd-order light. The two EF lenses and fold mirror are then mounted with aluminum box-beam to the base plate aligned with the exit aperture.

The entire EF device is then mounted on a 300 mm throw X/Y translation stage with variable resistor position encoding. The translation stage is driven by two stepper motors and is controlled by software that automatically steps the diffraction grating through angles appropriate to the frequency band being measured and records the diffraction angle using the rotary encoder. This setup is then mounted above the window of the receiver.

The measurement process begins with detectors tuned to measure signals and the SMB not rotating and a searching stage where the absolute position of an operational detector is locate by moving the EF on the translation stage until the chopped measured signal is maximized with the diffraction grating rotated with the grating facing out of the EF, the flat "mirror" side of the grating faces inside the EF. The grating is placed in this configuration to maximum output signal by allowing all frequencies output by the blackbody that lie within the order-sorting filter passband to be incident on the detector. The absolute position of the detector is then recorded using the X/Y translation encoders. These position measurements allow simple future location of other detectors by knowing the relative position of the detectors defined by the focal plane geometry and the cold optics.

The diffraction grating is then rotated $180°$ to define the $0°$ diffraction angle, and a scan through angles is performed over a range sufficient to cover the predicted EBEX frequency bands. Scan parameters for the three frequency bands are shown in Table 5.2. During later scans, it was discovered that spectral response could be measured with the SMB operating and a polarizing grid on the output of the EF with an increase in the noise level, which allowed for taking of spectral response data concurrently with frequency-dependent polarization rotation data [23].

Each scan took approximately an hour to perform and shifting between detectors for scans took approximately one hour to locate and maximize the EF signal. Approximately 120 s was spent on each diffraction grating angle for each scan in order

Band (GHz)	Number of Scans	Initial ϕ	Final ϕ	Initial ν (GHz)	Final ν (GHz)
150	17	21.0°	45.0°	212	107
250	12	24.0°	42.0°	353	189
410	10	23.0°	37.0°	518	336

Table 5.2: Spectral response scan initial and final diffraction grating angles and number of scans for each frequency band.
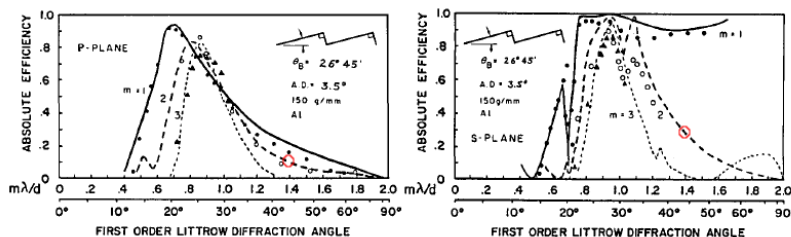
Figure 5.4: Measured diffraction grating efficiency for the two polarization states for a similar design, from [27]. First (solid), second (dashed), and third (dotted) orders and measured data are included. The red circles correspond to the EBEX 150 GHz diffraction grating design.

to integrate signal at that position to reduce the overall noise in the detection. The time-ordered bolometer and diffraction grating angle data with common time basis is then analyzed to determine the spectral response.

Ebert-Fastie Response

After the initial spectral response data for EBEX was taken, the spectral response of the Ebert-Fastie itself was measured in order to remove its effect on the EBEX data. The spectral response of the blackbody source is known and the EF mirror is predicted to have a flat-response, so the expected main contributor of spectral variation is the diffraction grating. Gratings of similar design have been shown to exhibit substantial frequency dependence as seen in Figure 5.4.

Figure 5.5: EF calibration response experimental setup.

Testing was performed at the University of Minnesota/Twin Cities between December 2011 and June 2014, with most of the data acquired after February 2014. The setup consists of a small cryogenic vessel with a single bolometric detector coupled through a small window and lightpipe to the filtered output aperture of the EF device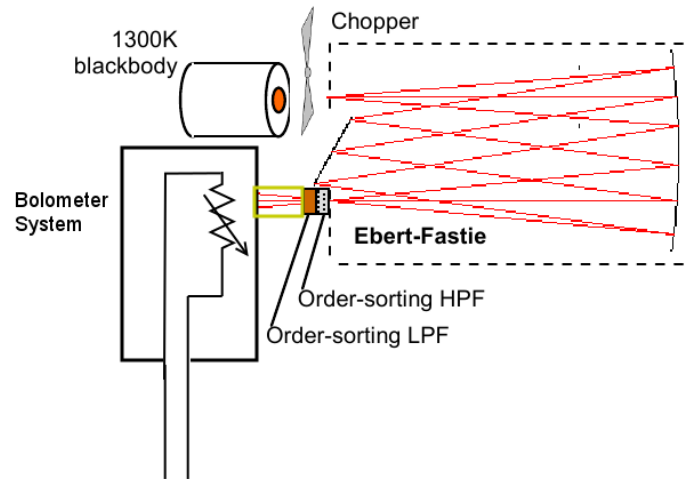. A diagram of the setup is shown in Figure 5.5. The testing procedure was similar to the EBEX testing procedure with diffraction grating angle steps with signal integration between each step. The detector data was readout using a lock-in amplifier reading out at the chop frequency of the EF optical chopper.

Without the internal filtering of the EBEX receiver, the EF-test cryostat required substantially more filtering of the EF output to reduce non-2$^{\mathrm{nd}}$-order contamination of the signal. This was accomplished by including low-frequency passband filters used as the band-defining filters on the focal planes for the frequency band above the band being measured. This removed high-frequency leakage from the original order-sorting LPE filter that would be filtered by low-pass filters present in the optics stack of EBEX during the original data-taking. Other signal leakage was tested for by including the high-pass waveguide filter for the higher frequency band and measuring the response of the bolometer over an grating angle scan. These tests showed either no response, or angle-independent offsets that were corrected for.
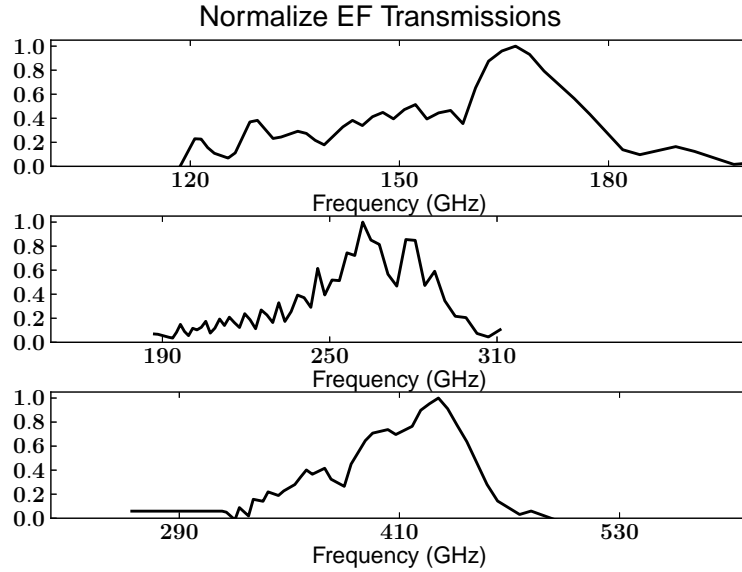
Figure 5.6: Measured EF response calibration, including blackbody source response, for the three frequency bands.

The measured Ebert-Fastie end-to-end measured response for the three frequency bands are shown in Figure 5.6. These response curves include the blackbody and order-sorting filter responses used in the EBEX spectral response measurements, however, they have the extra high-frequency leakage filter responses removed. These data sets will be referred to as $r_{\mathrm{EF,f}}(\phi_i)$ in the measured diffraction grating angle basis and $r_{\mathrm{EF},f}(\nu_i)$ in the frequency basis for frequency band f, with errors $\sigma_{\mathrm{EF,f}}(\phi_i)$ and $\sigma_{\mathrm{EF,f}}(\nu_i)$, respectively.

5.1.2   Analysis

The data measured during spectral response measurements consist of bolometer time stream data recorded in counts proportional to power absorbed by the bolometer, and diffraction grating angle with both sets of data time-ordered by the EBEX timing system [41] that supplies accurate timestamps to the entire EBEX payload. The common time basis allows analysis of the strength of the chopped monochromatic input light as a function of diffraction grating angle, and thus as a function of EF output central frequency. This process is repeated detector by detector for each EF scan performed and
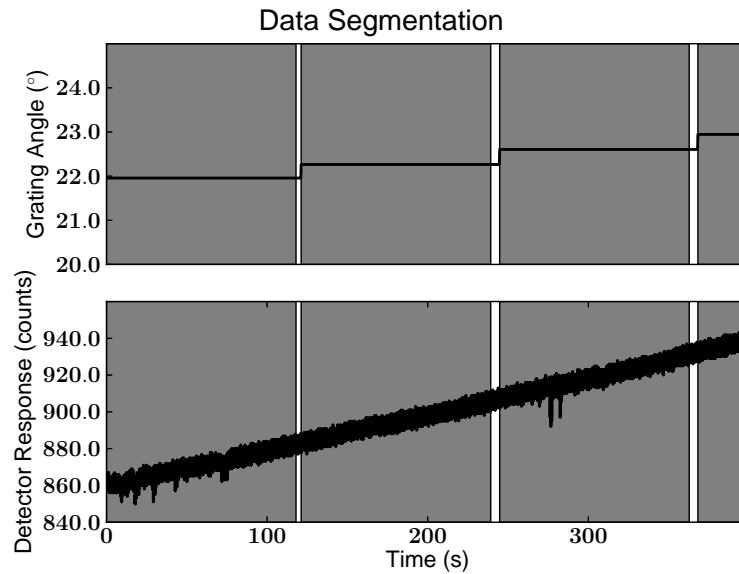
Figure 5.7: Examples of data segmentation for constant diffractin grating angle. The gray regions show data included for analysis.

aggregate spectral response curves for the three EBEX frequency bands are calculated.

The analysis pipeline begins by dividing the diffraction grating angle data into time segments corresponding to the different angle positions. Each segment has constant diffraction grating angle position with the diffraction grating changing position at the end of each segment, prior to the encoded change in angle. The final 2-3 seconds of each time segment is discarded to avoid collecting data while the grating position changes and the bolometer timestream data is divided into the same segments. An example of this segmenting of data is shown in Figure 5.7.

A linear fit to each bolometer data segment in time is found and removed from the data to remove any potential drift in the bolometer counts caused by ultrahead bath temperature changes or non-chopped incident power changes. Due to the large detector arrays constantly taking data, network throughput limitation sometimes cause dropped data packets that result in missing data in the bolometer timestream. To compensate for these rare occurances, missing data segments are filled with white noise at the level determined by the remaining data in the segment. A sample of this data processing is
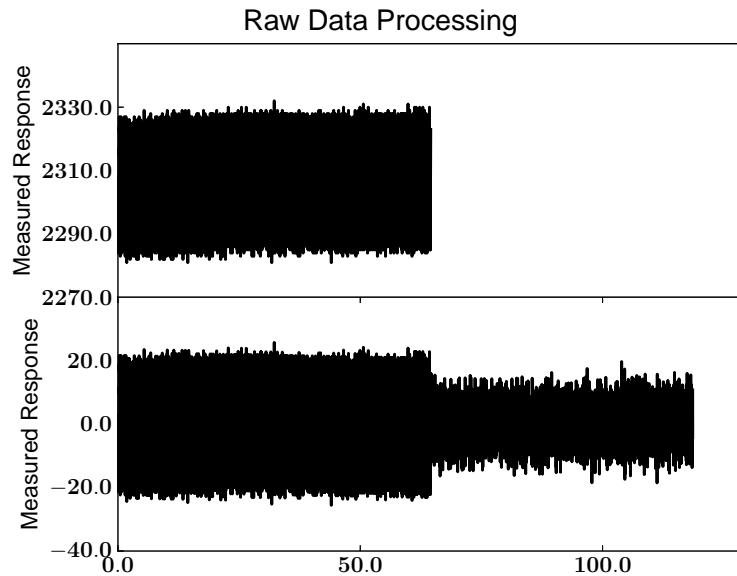
Figure 5.8: Upper figure shows raw detector data with missing data in the latter half. Lower figure shows offset and drift removal and missing data in time-ordered data filled with noise level consistent with data before and after the gap. To avoid skewing results, the chop signal is not reconstructed in the missing data sections, however, the power at the chop frequency is inversely scaled with the percentage of non-missing data.

shown in Figure 5.8.

The power spectral density, PSD, is computed from the fast-fourier transform, FFT, of the Hanning-windowed bolometer data and the power of the signal at the optical chop frequency is found. To obtain the power and an error value for the total power from the chopped signal, a fit of the data to a Fejer kernel,

$$F_N(x) = \frac{1}{N} \left(\frac{\sin \frac{Nx}{2}}{\sin \frac{x}{2}} \right)^2 \tag{5.4}$$

which models the power spectral density of a single input frequency in a finite, discrete data set [37, p. 400]. The Fejer kernel has the property $\int_{-\pi}^{\pi} F_N(x) \, dx = 2\pi$ and the value $\frac{1}{N}$ is the width of the peak. Thus for large N, the integral approaches the same value when only integrating near the central peak. The kernel is parameterized in the
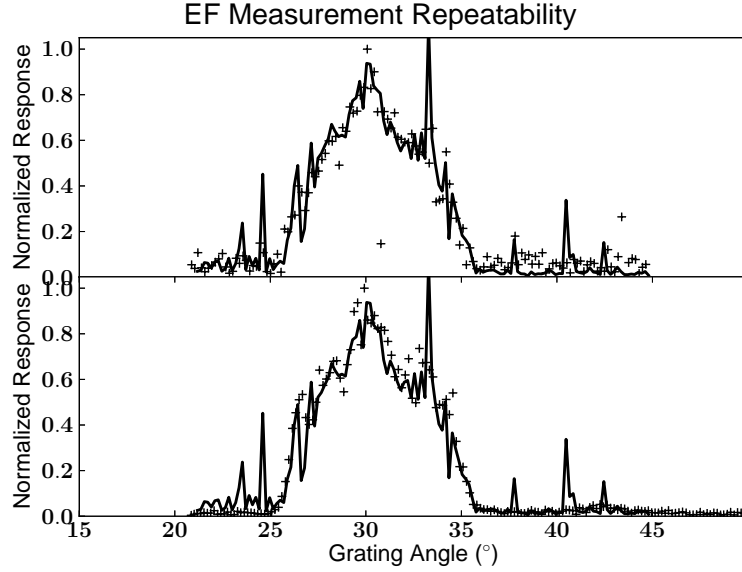
Figure 5.9: EF repeatability scans data for a single detector on the same day (upper) and on different days (lower).

data sets as,

$$F_C(\nu) = \frac{C_1}{2\pi C_2} \left(\frac{\sin \frac{C_2}{2}(2\pi t_s \nu - C_3)}{\sin \frac{1}{2}(2\pi t_s \nu - C_3)} \right)^2 + C_4 \tag{5.5}$$

where $t_s = 5.24$ ms is the time between bolometer samples, and the fit parameters C_1, C_2, C_3, and C_4 are the amplitude, N parameter, central peak frequency, and background noise level, respectively. Therefore, in this parameterization, the area of the fit is C_1 with error determined by the covariance matrix produced from the least-χ^2 fitting routine. This value for C_1 is the total power in the chopped signal peak in the PSD and is recorded for each diffraction grating angle.

The EF output central frequency, Equation 5.2, and dispersion, Equation 5.3, is determined for each diffraction grating angle and a spectral response for the detector scanned is found. An example of such as spectral response curve is shown in Figure 5.9. This process is repeated for every detector scanned for a given frequency band in order to find an average spectral response for each band.

Before forming an average spectral response, it was noticed that the individual response curves for the detectors, noted from here on as $b_i(\nu_{ij})$ in frequency-space,

and $b_i(\phi_{ij})$ in grating angle-space as each measurement has a unique frequency/angle coverage, in a given band do not agree on the low- and high-frequency cutoffs of the band, with variability on the scale of 5 GHz for all three bands. In particular, the low-frequency cutoff governed by the waveguide radius is expected to agree within the machining tolerances used in the fabrication, <0.0013 mm, which corresponds to low-frequency cutoff variations on the scale of $\Delta\nu_c = \frac{1.841c}{2\pi r^2}\Delta r$, which predicts a variability of 0.26, 0.67, 1.9 GHz for the 150, 250, and 410 GHz bands. It was also noted that the high-frequency cutoff variability is larger than the low-frequency variability.

To explain this phenomenon, a model where the initial setting of the 0° diffraction grating angle has an error was proposed. This model would predict an angular offset to the spectral response data, and due to the nonlinear relation between angle and central frequency, it would predict a larger offset at high frequencies, as borne out in the data. The nature of this angular offset was unknown, but could stem from the incomplete or overcomplete rotation of the diffraction grating 180° from the maximum signal to establish the 0° diffraction grating angle, a misalignment of the EF mirror to the diffraction grating, or a error in the fabrication of the gratings themselves. In particular, the EF mirror alignment was confirmed to be correct within 0.1° which would produce an error of 0.2 GHz at the low-frequency cutoff of the 150 GHz band, and both the EF mirror misalignment and fabrication error explanation would cause constant angular offsets.

Duplicate response measurements of detectors on the same day and different days was taken to determine the cause of the variability. Response curves for a detector taken immediately following each other show good agreement of the cutoff frequencies, Figure 5.9, and responses taken on different days show similar agreement. Measurements of detector responses with and without SMB rotation also show no substantial difference in variability outside of increased noise level. Error in calibration of the 0° diffraction grating angle then is the prime candidate this phenomenon.

In order to correct for possible miscalibration of the 0° angle, two methods are used in parallel to align the detector response curves to form a band response curve.

"Average"-Alignment Method

The first method employed, called the "average"-alignment method, assumes that the source for the angle misalignment is symmetric about the correct $0°$ when averaged over all the detector responses. Random misalignment of the diffraction grating would would be averaged out in this method. The "unaligned" detector responses and errors, $b_i(\phi_{ij})$ and $\sigma_i(\phi_{ij})$, are each individually interpolated into a common angular basis, ϕ_k, and then an average response at each angle is found by variance-weighted averaging of all the detector responses at that angle,

$$b_{\text{mis},f}(\phi_k) = \sum_{i \in f} \frac{b_i(\phi_k)}{\sigma_i^2(\phi_k)} \tag{5.6}$$

In this way, an "misaligned average" response, $b_{\text{mis},f}(\phi_k)$, is formed that would eliminate an symmetric misalignment of the $0°$ angle for each frequency band, f. To simplify terminology, f also refers to the set of all detectors in frequency band f. This misaligned average is then used as a model to fit the individual detector responses to by a least-χ^2 fit with a detector-dependent angular shift, α_i. The angle-spaces of each detector response curve are adjusted, $\phi_{ij} \rightarrow \phi_{ij} - \alpha_i$ forming a new response $b_i'(\phi_{ij})$ and error $\sigma_i'(\phi_{ij})$ curves for each detector, are interpolated to the previous common angular basis, ϕ_k, and then a new variance-weighted average curve is found,

$$b_{\text{align},f}(\phi_k) = \sum_{i \in f} \frac{b_i'(\phi_k)}{\sigma_i'^2(\phi_k)} \tag{5.7a}$$

$$\sigma_{\text{align},f}(\phi_k) = \left(\sum_{i \in f} \frac{1}{\sigma_i'^2(\phi_k)} \right)^{-\frac{1}{2}} \tag{5.7b}$$

The frequency basis, ν_k, and dispersion, $\Delta\nu_k$, is found from Equations 5.2 and 5.3, and the "average"-aligned band spectral responses are found. These are shown in Figure 5.10.

"Waveguide"-Alignment Method

The second method for alignment, called the "waveguide"-alignment method, assumes nothing about the source of the angle misalignment, but instead, assumes the physics
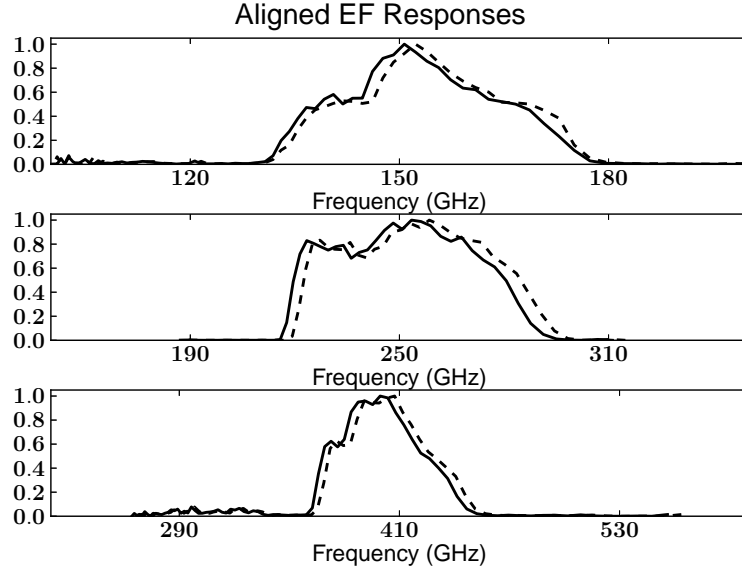
Figure 5.10: Measured spectral response for EF and receiver system for the three frequency bands with "average"-alignment (dashed) and "waveguide"-alignment (solid) schemes.

governing the frequency response of the waveguides is well known and, given the accuracy of fabrication of the waveguides, could be used as the "known" spectrum to align the individual detectors to. For each band, a predicted response curve is formed from the combination of the waveguide response, Equation 4.12, LPE filters, Section 4.4, and the measured intrinsic EF response. The predicted measured response, $p_{\mathrm{EF},f}(\nu_j)$ is found by interpolating the EBEX predicted response with NDF, $p_{\mathrm{Full},f}(\nu_i)$ into a common frequency basis with the measured EF response, $r_{\mathrm{EF},f}(\nu_j)$ and setting $p_{\mathrm{EF},f}(\nu_j) = p_{\mathrm{Full},f}(\nu_j)r_{\mathrm{EF},f}(\nu_j)$. To compensate for the known dispersion of the EF output, the predicted measured response curve is found in the angular domain and convolved,

$$p'_{\mathrm{EF},f}(\phi_i) = (p_{\mathrm{EF},f} * w)(\phi_i) \tag{5.8}$$

with the a half-circle window function, $w(\phi) = \sqrt{\left(\frac{\Delta x}{2L_B}\right)^2 - \phi^2}$ and then converting back to frequency-space to better match the expected spectra. These predicted curves are shown in Figure 5.11.

As in the "average"-alignment method, the predicted response curve is used as a model that the individual detector responses are least-χ^2 fit to with angular offset as the only free parameter. Adjusted angle-space responses are then used in a variance-weighted average, Equation 5.7, and the frequency-basis and dispersion are found to form the "waveguide"-aligned band spectral response.

Comparing the aligned data sets to predicted curves, shows better χ^2_{red} values for the "waveguide"-alignment method indicating that the misalignment mechanism shows bias away from the nominal $0°$ angle of the diffraction grating. The "average"-aligned data sets are neglected henceforth.

5.1.3   Results

The ultimate goal of the spectral response measurements is to determine the frequency response of the EBEX receiver for flight operations. The first step in this process is to first find the response of the receiver alone during the EF measurement process. This is found by dividing the EF spectral response from both sets of the aligned data, including error propagation after interpolation of the EF spectral response to the same frequency basis as the aligned data to find the EBEX measured ground response,

$$r_{\mathrm{Ground},f}(\nu_i) = \frac{b_{\mathrm{align},f}(\nu_i)}{r_{\mathrm{EF},f}(\nu_i)} \tag{5.9a}$$

$$\sigma^2_{\mathrm{Ground},f}(\nu_i) = r^2_{\mathrm{Ground},f}(\nu_i) \left[\left(\frac{\sigma_{\mathrm{align},f}(\nu_i)}{b_{\mathrm{align},f}(\nu_i)} \right)^2 + \left(\frac{\sigma_{\mathrm{EF},f}(\nu_i)}{r_{\mathrm{EF},f}(\nu_i)} \right)^2 \right] \tag{5.9b}$$

This response curves can be compared to $p_{\mathrm{Ground},f}(\nu_i)$ and are shown in Figure 5.11. It should be noted that the real spectral response would deconvolve the window function from the data as well as removing the EF response. However, due to the noisy nature of the measured data, this is infeasible and simulations of several band shapes showed errors in the effective band centers and widths of less than 0.08 GHz between convolved and non-convolved data with the same window function and so the effect is ignored.

The final step for a flight-like spectral response measurement is to remove the predicted NDF and thick window spectra from the EBEX measured ground response,

$$r_{\mathrm{Flight},f}(\nu_i) = \frac{r_{\mathrm{Ground},f}(\nu_i)}{p_{\mathrm{NDF+Wind},f}(\nu_i)} \tag{5.10a}$$

$$\tag{5.10b}$$

Figure 5.11: Receiver-only measured (points) and predicted (solid) spectral response for the three frequency bands with Palestine 2012 configuration.

The error in $r_{\mathrm{Flight},f}(\nu_i)$ is determined from propagation of errors in the NDF optical properties, window thickness, and error in the ground response. The EBEX flight spectral responses can be compared to $p_{\mathrm{Flight},f}(\nu_i)$, and are shown in Figure 5.12. A comparison of the measured responses to the predicted yield χ^2_{red} values of 4.34, 5.72, and 4.72 for the 150, 250, and 410 GHz bands, showing reasonable agreement between the measured responses and predictions. Noticeable differences include a "fringing" effect possibly stemming from filter thicknesses on order of the waveguides being measured and a measured dearth of response on the 150 GHz band at roughly 170 GHz. This lack of response seems to originate from an excess of EF response at the corresponding frequency that is unaccounted for.

To compare the measured responses to design requirements, the equivalent-boxcar parameters, band center and width, are found by calculating the total spectral power
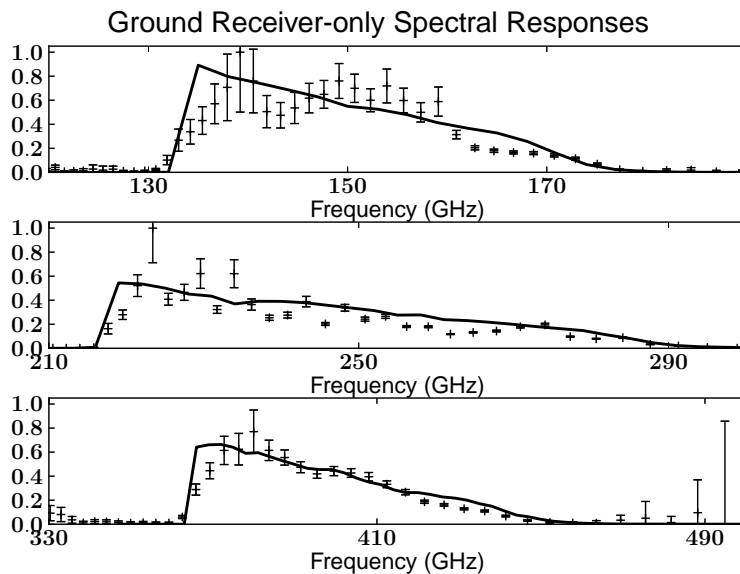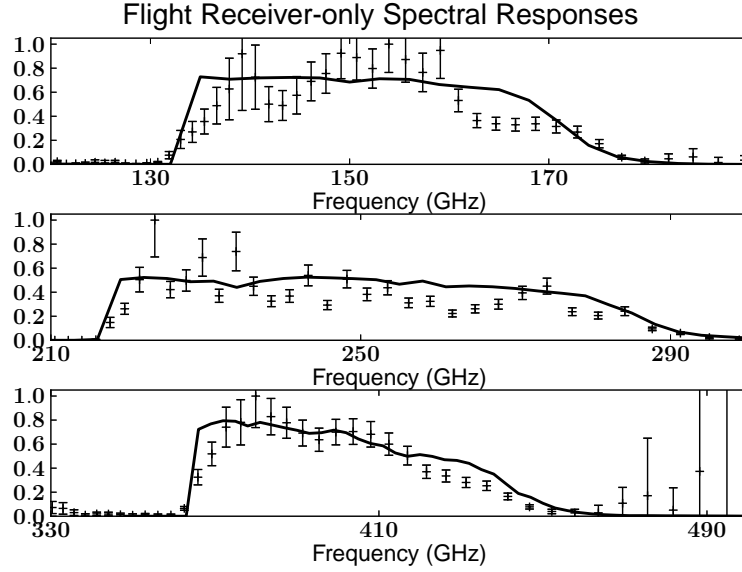
Figure 5.12: Receiver-only measured (points) and predicted (solid) spectral response for the three frequency bands with LDB configuration.

in the response curves and then cumulative power function in a numerical fashion,

$$P(\nu_i) = \frac{r_{\text{Flight},f}(\nu_i)}{\max(r_{\text{Flight},f}(\nu_i))}(\nu_i - \nu_{i-1}) \tag{5.11a}$$

$$C_P(\nu_i) = \sum_{j \leq i} P(\nu_j) \tag{5.11b}$$

The equivalent-boxcar band center, ν_{center}, is defined by $C_P(\nu_{\text{center}}) = 0.5$, the location where half of the spectral power $\int r(\nu)\,\mathrm{d}\nu$, is on either side. The band width, $\Delta\nu = \max(C_P(\nu_i))$ is defined as the total spectral power divided by the amplitude of the equivalent-boxcar function, 1.0. The calculated band centers and widths are shown in Table 5.3. Comparing these values to the requirements in Table 5.1, we see that the 250 and 410 bands statisfy the requirements, while the 150 GHz band center error is 10% larger than the requirement and the width error is a factor of 1.4 larger than the requirement. Improvements in the errors of the EF measured response could potentially reduce the 150 GHz band center and width errors to 0.5 and 0.8 GHz, respectively, within the requirements.

Band (GHz)	Measured ν_{center} (GHz)	Measured $\Delta\nu$ (GHz)
150	152.6±1.1	25.1±1.4
250	244.0±0.9	27.5±1.1
410	393.9±1.7	45.4±2.1

Table 5.3: Equivalent-boxcar band center and widths for EBEX measured flight spectral responses for the three frequency bands.

5.2 Polarization Modulation Efficiency

Polarization modulation efficiency is a measure of the depolarization of the AHWP, $Q, U \rightarrow I, V$, and impacts the overall measured polarization signal magnitude. Simulations of the AHWP predict PME values $> 98\%$ across all three frequency bands and a requirement of $> 90\%$ is placed on the experiment in order measure $r = 0.01$.

5.2.1 Measurement

PME is measured by injecting a entirely linearly polarized signal into a polarimeter and determining the maximum and minimum intensities measured as the polarized signal rotates,

$$\text{PME} \equiv \frac{I_{\max} - I_{\min}}{I_{\max} + I_{\min}} \tag{5.12}$$

with PME= 1.0 indicating no depolarization of the linearly polarized input signal, and PME= 0.0 indicating complete depolarization. See Figure 5.13 for a simple PME measurement setup.

PME testing took place in Palestine, TX, on July 11 and 13, 2012, and the experimental setup for quantifying the PME of the EBEX receiver was similar to the spectral response measurement setup described in Section 5.1.1. The only exceptions are that the EF diffraction grating was placed in the "mirror" position with the flat metal side facing into the EF cavity in order to maximize and remove the spectral dependence of the output signal, the order-sorting filters were removed, and a small polarizing grid was placed at the output of the EF. The SMB was stationary during all testings. In this configuration, the entire blackbody source radiation is reflected to the exit aperture
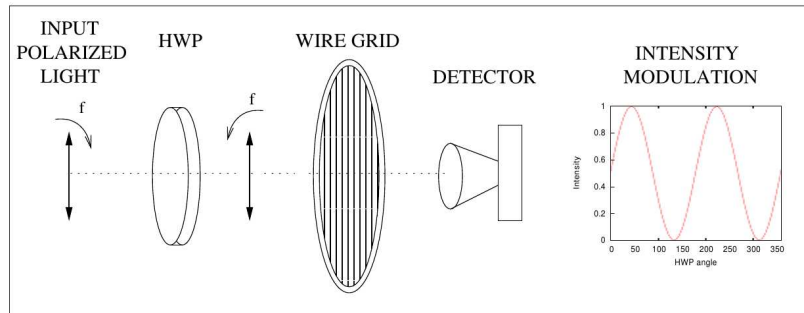
Figure 5.13: Basic PME measurement setup, figure modified from [19].

and linearly polarized by the EF grid prior to coupling to a single detector through the EF and EBEX cold optics. A single detector was scanned at a time in order to maximize signal-to-noise by concentrating all the power onto that detector. This was often performed on detectors of known EF coupling position from the spectral response measurements. PME measurements were performed aligned on 16 separate detectors over the three frequency bands, and due to placement of the second focal plane, 20 detectors has measurable PME response.

The small EF polarizing grid has a circumferential tape measure to indicate angular position and was mounted on on a rotating stage to facilitate the PME measurement. The EF grid consists of a 38 micron thick Mylar film with bonded electroformed 5 micron gold wires with 102 micron spacing made by Buckbee-Mears and was initially used for calibration of the MAXIPOL experiment [21]. A similar grid made of the same material was measured by the MAXIPOL experiment to have a PME of 96.6% at 140 GHz [20]. The circumferential position of the EF grid is measured relative to a horizontal line on the EF device.

The measurement procedure involved placing the EF grid at a known, fixed orientation and integrating detector signal over a period of about 30 seconds with the SMB stationary. The EF grid was then rotated roughly 5° by hand, and the process was repeated over a >180° rotation, with most tests spanning >360° of rotation. The circumferential position and time of rotation of each EF grid step was logged using the common timebase used by the detector system in order to ease data analysis. The output of the EF was once again chopped to eliminate systematic effects.

5.2.2 Analysis

The data measured during PME measurements consist of bolometer time stream data recorded in counts proportional to power absorbed by the bolometer, and EF grid circumferential position with both sets of data time-ordered by the EBEX timing system.

The analysis process begins with the same segmenting of bolometer data and EF grid position data into segments of constant grid position. Once again, the final 5 seconds of data from each segment are discarded to avoid analyzing data during grid rotation. The bolometer data has a linear fit to the data removed to remove any offset or drift in the baseline level of detection and any missing data chunks are filled with noise at levels consistent with the data before and after the missing chunk.

A PSD of the bolometer data is calculated and the power in the chopped signal measured by the bolometer is measured by fitting the data near the chop frequency to a Fejer kernel, see Section 5.1.2. The power and error in the power for each grid position is then logged, and the EF grid angle is calculated at each position with,

$$\theta(x) = \frac{360°}{D_f - D_i}(x - D_i) \tag{5.13}$$

for circumferential position x, with the tape measure spanning from $D_f = 340.3$ mm to $D_i = 320.1$ mm. The $\theta(D_i) = 0$ position of the EF grid roughly corresponds to the transmission axis of the polarizer. With the measured power, $a_i(\theta_{ij})$, and error, $\sigma_{ai}(\theta_{ij})$, logged as a function of EF grid angle for each of the detectors, i, scanned, the intensity versus angle (IVA) curves can then be modeled to quantify the PME for each frequency band.

5.2.3 Results

A basic PME calculation can be performed with the IVA data at this point for all frequency bands with Equation 5.12 where there is adequate data point coverage near maxima and minima, however, to confirm our understanding of the polarization properties of the receiver and better fit the data, a model for the IVA curves is generated. The Stokes vector for the input polarized signal for the receiver is,

$$\boldsymbol{S}_{\text{in}}(\alpha) = \begin{pmatrix} I \\ Q \\ U \\ V \end{pmatrix} = I_0 \begin{pmatrix} 1 \\ \cos 2\alpha \\ \sin 2\alpha \\ 0 \end{pmatrix} \tag{5.14}$$

for completely linearly polarized light at some angle α relative to a fixed coordinate system. This light is incident on the AHWP, which we will treat as a monochromatic HWP with Mueller matrix,

$$\boldsymbol{M}_{\text{HWP}}(\rho, \delta) = \begin{pmatrix} 1 & 0 & 0 & 0 \\ 0 & \sin^2 \frac{\delta}{2} \cos 4\rho + \cos^2 \frac{\delta}{2} & \sin \frac{\delta}{2} \sin 4\rho & -\sin \delta \sin 2\rho \\ 0 & \sin \frac{\delta}{2} \sin 4\rho & -\sin^2 \frac{\delta}{2} \cos 4\rho + \cos^2 \frac{\delta}{2} & \sin \delta \sin 2\rho \\ 0 & \sin \delta \sin 2\rho & -\sin \delta \sin 2\rho & \cos \delta \end{pmatrix}$$
(5.15)

for HWP angle ρ relative to the same fixed coordinate system and HWP retardance δ, Equation 3.4. In an ideal HWP, $\delta = \pi$ and this simplifies to,

$$\boldsymbol{M}_{\text{HWP,ideal}}(\rho) = \begin{pmatrix} 1 & 0 & 0 & 0 \\ 0 & \cos 4\rho & \sin 4\rho & 0 \\ 0 & \sin 4\rho & -\cos 4\rho & 0 \\ 0 & 0 & 0 & -1 \end{pmatrix}$$
(5.16)

A non-ideal polarizing grid has Mueller matrix,

$$\boldsymbol{M}_{\text{Grid}}(g_+, g_-, g_\times) = \frac{1}{2} \begin{pmatrix} g_+ & g_- & 0 & 0 \\ g_- & g_+ & 0 & 0 \\ 0 & 0 & g_\times & 0 \\ 0 & 0 & 0 & g_\times \end{pmatrix}$$
(5.17)

with $g_\pm = T_t^2 \pm T_r^2$ and $g_\times = 2T_t T_r$ with field transmittances T_t, T_r through the grid transmission and reflection axis, respectively. Since we are only concerned with relative amplitude changes in the output signal, the absolute scaling of the signal will disappear in Equation 5.12, this parameterization can be reduced to,

$$\boldsymbol{M}'_{\text{Grid}}(\epsilon) = \begin{pmatrix} 1 & \epsilon & 0 & 0 \\ \epsilon & 1 & 0 & 0 \\ 0 & 0 & \xi & 0 \\ 0 & 0 & 0 & \xi \end{pmatrix}$$
(5.18)

with $\epsilon = \frac{T_t^2 - T_r^2}{T_t^2 + T_r^2}$ defining the grid efficiency and $\xi = \frac{2T_t T_r}{T_t^2 + T_r^2} = \sqrt{1 - \epsilon^2}$, with the leading factors dropped. This is then a single parameter, ϵ, matrix. The internal grid of the receiver is assumed to be ideal with $T_t = 1$ and $T_r = 0$ ($\epsilon = 1$, $\xi = 0$) while any inefficiencies will be grouped with HWP inefficiencies. Using the rotation Mueller matrix,

$$\boldsymbol{R}(\phi) = \begin{pmatrix} 1 & 0 & 0 & 0 \\ 0 & \cos 2\phi & \sin 2\phi & 0 \\ 0 & -\sin 2\phi & \cos 2\phi & 0 \\ 0 & 0 & 0 & 0 \end{pmatrix}$$
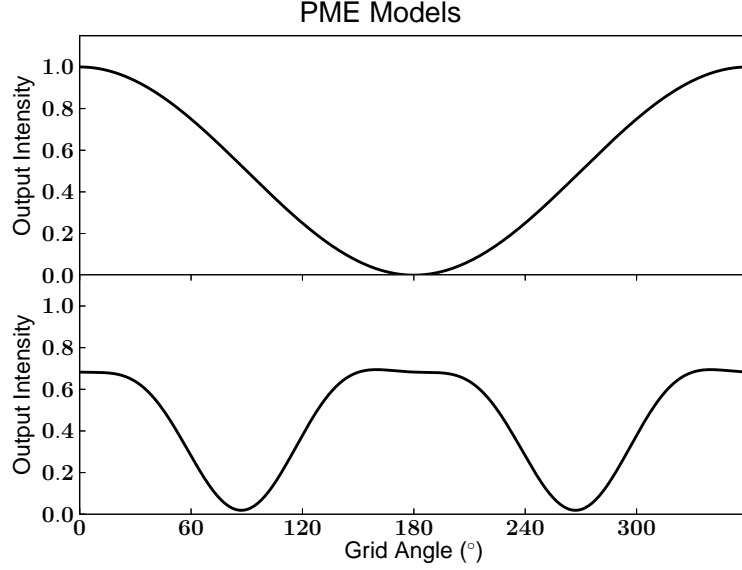(5.19)

Figure 5.14: Simple (upper) and complex (lower) PME measurement models. The complex model uses $\epsilon' = 0.95$, $\alpha = 85°$, $p = 0.3$, $\omega = -8°$.

where a rotation of $+45°$ $+Q \to +U$, the grid matrix is rotated with $\boldsymbol{M}'_{\text{Grid}}(\phi, \epsilon) = \boldsymbol{R}(\phi)\boldsymbol{M}'_{\text{Grid}}(\epsilon)\boldsymbol{R}(-\phi)$ to give the generalized position non-ideal grid Mueller matrix,

$$\boldsymbol{M}'_{\text{Grid}}(\phi, \epsilon) = \frac{1}{2} \begin{pmatrix} 1 & \epsilon\cos 2\phi & \epsilon\sin 2\phi & 0 \\ \epsilon\cos 2\phi & \cos^2 2\phi - \xi\sin^2 2\phi & \frac{1-\xi}{2}\sin 4\phi & 0 \\ \epsilon\sin 2\phi & \frac{1-\xi}{2}\sin 4\phi & \sin^2 2\phi + \xi\cos^2 2\phi & 0 \\ 0 & 0 & 0 & 0 \end{pmatrix} \tag{5.20}$$

For the ideal internal grid,

$$\boldsymbol{M}'_{\text{Int}}(\phi) = \frac{1}{2} \begin{pmatrix} 1 & \cos 2\phi & \sin 2\phi & 0 \\ \cos 2\phi & \cos^2 2\phi & \frac{1}{2}\sin 4\phi & 0 \\ \sin 2\phi & \frac{1}{2}\sin 4\phi & \sin^2 2\phi & 0 \\ 0 & 0 & 0 & 0 \end{pmatrix} \tag{5.21}$$

For the scenario with ideal HWP and grid and 100% polarization fraction input signal, the measured output signal due to the bolometric detectors is the intensity component of $\boldsymbol{S}_{\text{out}}(\theta, \phi, \rho) = \boldsymbol{M}'_{\text{Int}}(\phi)\boldsymbol{M}_{\text{HWP,ideal}}(\rho)\boldsymbol{S}_{\text{in}}(\theta)$ which yields,

$$I_{\text{out}} = I_o(1 + \cos(4\rho - 2\theta - 2\phi)) = I_o(1 + \cos\psi) \tag{5.22}$$

for generalized angle ψ after simplification. This produces an IVA curve seen in Figure 5.14 with PME=1.0. We then introduce the expected inefficiencies in the system by using the non-ideal HWP Mueller matrix. Another complication is that the input polarized signal originates from the EF grid, which may not completely polarize the output light from the EF. This is characterized with Equation 5.20 as $\boldsymbol{M}'_{\mathrm{EF}}(\theta, \epsilon)$ and using an unpolarized Stokes vector as $\boldsymbol{S}_{\mathrm{in}}$ the output becomes $\boldsymbol{S}_{\mathrm{out}}(I_o, \theta, \phi, \rho, \epsilon, \delta) = \boldsymbol{M}_{\mathrm{Grid}}(\phi)\boldsymbol{M}_{\mathrm{HWP}}(\rho, \delta)\boldsymbol{M}'_{\mathrm{EF}}(\theta, \epsilon)\boldsymbol{S}_{\mathrm{input}}(I_o)$ which yields an intensity element,

$$
\begin{aligned}
I_{\mathrm{out}}(I_o, \theta, \phi, \rho, \epsilon, \delta) = {} & I_o + I_o\epsilon\cos(2\theta + 2\phi)\sin^2\frac{\delta}{2}\cos 4\rho \\
& + I_o\epsilon\cos(2\theta - 2\phi)\cos^2\frac{\delta}{2} \\
& + I_o\epsilon\sin(2\theta + 2\phi)\sin\frac{\delta}{2}\sin 4\rho
\end{aligned}
\tag{5.23}
$$

This model is fit to the individual measured IVA curves, $a_i(\theta)$ through a least-χ^2 routine to obtain the values of the 5 free parameters, I_o, ϕ, ρ, ϵ, and δ, which correspond to response amplitude, receiver internal grid angle, AHWP angle, EF grid efficiency, and AHWP retardance. This fitting routine systematically failed to converge to a solution due to the strong degeneracy of ϵ and δ for $\delta \approx \pi$, as is expected for the EBEX AHWP design. The degeneracy was removed by setting $\delta = \pi$ and any deviation from this value would be encoded in the new efficiency value, ϵ'. This new fit model is shown in Figure 5.14, and with simplication the calculation for PME becomes PME= ϵ', the effective efficiency of the EF grid. For two or three of the IVA curves with large deviations from sinusoidal behavior, this models fails to fit accurately. To explain this non-sinusoidal behavior, a model is constructed where the light exiting the EF device *prior* to the EF grid is partially polarized. The source of this polarization is suspected to be the diffraction grating which is likely to exhibit different reflections for the two polarization modes, resulting in a net linear polarization, though this is expected to be small. In this model, the input Stokes vector is,

$$
\boldsymbol{S}_{\mathrm{in,pol}}(I_o, p, \alpha) = I_0\begin{pmatrix} 1 \\ p\cos 2\alpha \\ p\sin 2\alpha \\ 0 \end{pmatrix}
\tag{5.24}
$$

with unknown EF output polarization angle α and polarization fraction p, and finding

the intensity element of the output Stokes vector,

$$\boldsymbol{S}_{\text{out}}(I_o, \theta, \phi, \rho, \epsilon, \delta) = \boldsymbol{M}_{\text{Grid}}(\phi)\boldsymbol{M}_{\text{HWP}}(\rho, \delta)\boldsymbol{M}_{\text{EF}}(\theta, \epsilon)\boldsymbol{S}_{\text{input,pol}}(I_o, p, \alpha) \qquad (5.25)$$

$$\begin{aligned}
I_{\text{out}}(I_o, \theta, \phi, \rho, \epsilon, \delta, p, \alpha) = {}& I_o + I_o \epsilon p \cos(2\theta - 2\alpha) \\
& + I_o \left[\sin 2\phi \sin\frac{\delta}{2}\sin 4\rho + \cos 2\phi(\sin^2\frac{\delta}{2}\cos 4\rho + \cos^2\frac{\delta}{2})\right] \\
& * \left[\epsilon \cos 2\theta + p\cos 2\alpha(\cos^2 2\theta - \xi\sin^2 2\theta) + \frac{1-\xi}{2}p\sin 2\alpha \sin 4\theta\right] \\
& + I_o \left[\cos 2\phi \sin\frac{\delta}{2}\sin 4\rho + \sin 2\phi(-\sin^2\frac{\delta}{2}\cos 4\rho + \cos^2\frac{\delta}{2})\right] \\
& * \left[\epsilon \sin 2\theta + p\sin 2\alpha(\sin^2 2\theta + \xi\cos^2 2\theta) + \frac{1-\xi}{2}p\cos 2\alpha \sin 4\theta\right]
\end{aligned}$$
$$(5.26)$$

Again, with $\delta \approx \pi$, $p \approx 0$, and $\epsilon \approx 1$ leads to degeneracy in the fitting algorithm and so $\delta = \pi$ is set and deviations are absorbed into the ϵ' value and the output intensity becomes,

$$\begin{aligned}
I_{\text{out}}(I_o, \theta, \omega, \epsilon', p, \alpha) = {}& I_o + I_o \epsilon' p \cos(2\theta - 2\alpha) \\
& + I_o \cos\omega \left[\epsilon'\cos 2\theta + p\cos 2\alpha(\cos^2 2\theta - \xi\sin^2 2\theta) + \frac{1-\xi}{2}p\sin 2\alpha \sin 4\theta\right] \\
& + I_o \sin\omega \left[\epsilon'\sin 2\theta + p\sin 2\alpha(\sin^2 2\theta + \xi\cos^2 2\theta) + \frac{1-\xi}{2}p\cos 2\alpha \sin 4\theta\right]
\end{aligned}$$
$$(5.27)$$

where $\omega = 4\rho - 2\phi$ is the effective angle of the AHWP and internal grid system.

Using this new function at a fitting model, the IVA data sets are least-χ^2 fit and the five free parameters and their errors are determined from the covariance matrix produced. Example fits to the data are shown in Figure 5.15. These fits showed marginally better agreement with the sinusoidal data sets, and substantially better agreement with the non-sinusoidal data sets. The agreement with both types of data sets indicates that the model being used is viable. Ranges the fit parameters calculated are shown in Table 5.4.

The values for p and α are expected to remain constant for all IVA measurements for the same frequency band as both stem from the polarized output of the EF. Figure 5.16
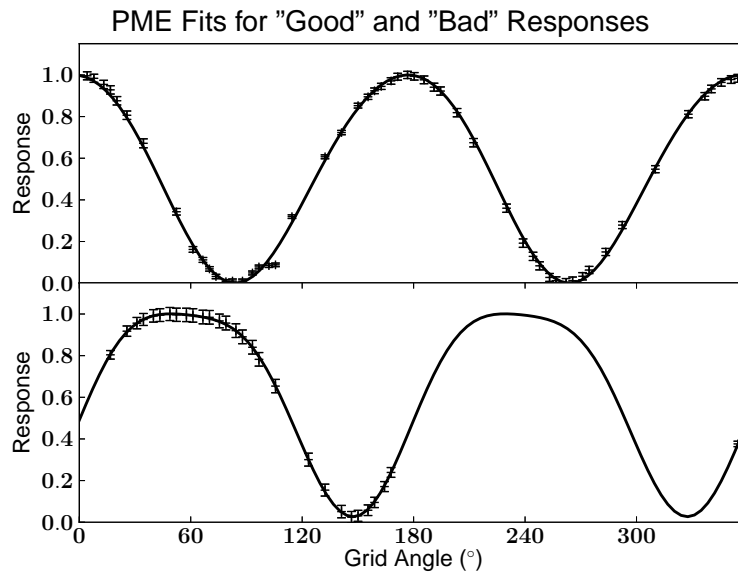
Figure 5.15: Complex PME model fit to sinusoidal (upper) and non-sinusoidal (lower) data sets.

shows the distribution of the α and p parameters for the three frequency bands. The EF polarization angle data sets reside mostly near 90° for all three frequency bands, indicating a linear polarization of the EF output parallel to the diffraction grating axis and perpendicular to the plane of incident of the light reflecting off the mirror face of the grating, as would be expected for reflections off of a metallic surface.

For a majority of the high signal-to-noise IVA curves, the polarized fraction of the EF output is approximately 10%, however, the for three data sets, the polarized fraction

Band (GHz)	ω (°)	ϵ'	p	α (°)
150	-2 − -14	0.8 − 1.0	0.1 − 0.5	40 − 105
250	-17 − 53	0.94 − 1.00	0.11 − 0.44	85 − 91
410	-57 − 62	0.8 − 0.95	0.04 − 0.5	60 − 125

Table 5.4: Ranges of fit parameters for PME measurements for the three EBEX frequency bands.
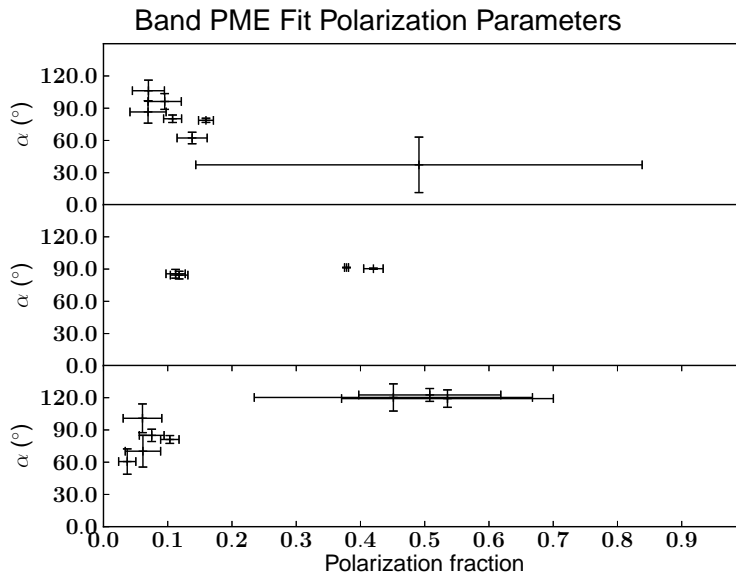
Figure 5.16: PME data set fits for EF polarization angle, α, and fraction, p.

is about 40%. Two of these scans show a flattening of the IVA near the maximum signal response, see Figure 5.15, as would be expected for saturation of the detectors by a large signal, however, the detector count and noise levels for these are consistent with more nominal scan values, making saturation improbable. The possible misplacement of the diffraction grating with the grating side facing towards the EF cavity is also ruled out by the signal strength as the observed dropoff between mirror side and grating side is around a factor of 10. There is no current model for these high polarization fraction scans.

Averaging the PME values determined from each of the data set fits for each frequency bands yields the final measured PME values, shown in Table 5.5. These values include the efficiency of the grid, and as such, reflect an lower bound to the EBEX receiver PME values. An alternative way of determining PME values from telescope scans of a polarized light source using the full EBEX payload [23] found similar, PME= 0.998, values for the total population of detectors. These values exceed the PME values required for the EBEX science detection goals, PME > 0.9.

Band (GHz)	PME	p	α (°)
150	0.977 ± 0.059	0.125 ± 0.007	79.1 ± 1.6
250	0.977 ± 0.019	0.358 ± 0.003	91.33 ± 0.14
410	0.918 ± 0.058	0.023 ± 0.002	108.0 ± 2.1

Table 5.5: Average band values of PME, p, and α.

5.3 Antenna Pattern

The EBEX telescope was designed to produce frequency-independent Gaussian beam patterns with 8' FWHM. Characterization of the actual antenna response of the telescope is required to validate the optical design and ensure optimal performance in during flight data-taking. Asymmetry in the beam shape would produce a smearing effect of observed power on the sky, especially at small scales of order the beam size, and would be aggravated by sky rotation during long observations. With the maximum primordial B-mode expected at a scale of order $\ell = 1000$, or $\theta \approx 11'$, the measurement and correction of beam asymmetries is vital to the science goals of EBEX.

Two stages of beam characterization were performed. The first test was performed with the EBEX receiver only to measure the cold optics antenna response as a first-look characterization of the full beam response and to ensure proper alignment of the receiver optics. The second testing was performed with the entire EBEX telescope to measure the flight-like beam response.

5.3.1 Receiver Characterization

The initial beam response measurements of the receiver-only optics system were performed in April through May 2011 at the CSBF facility in Palestine, TX, with the most complete measurements taking place in June 2011.

Measurement

The experimental procedure consisted of utilizing the EF device used in spectral response, Section 5.1, and polarization modulation efficiency, Section 5.2, with the diffraction grating in the mirror position to maximize measured response on a single detector and optical chopper modulating the output signal. The SMB was kept stationary during the testing process and there was no external polarizing grid at the EF output.

The EF was translated on its X/Y-translation stage in 6 mm increments in the y-direction, perpendicular to the receiver plane of symmetry, over a 230 mm path along the top of the receiver window and detector response measured at each step before incrementing the translation stage by 12 mm in the x-direction, see Figure 5.3. The scan was then reserved along the y-direction and the process was repeated until a 230 mm by 130 mm patch of the window was scanned over. The test was performed on a single 150 GHz detector as a proof of the optical alignment. The EF device position and time at that position were logged in the same time basis as the detector readout to ease analysis.

Analysis

The analysis of the receiver-only beam response measurement followed the pattern of previous measurements with Fejer kernel fitting of the detector response PSD at the EF chop frequency at each position step with final detector response as a function of EF position, $b_{\mathrm{Receiver-only}}(x, y)$.

Results

The measured beam response as a function of EF position are shown in Figure 5.17 with average FWHM curve along with a predicted beam FWHM curve. This testing proved the overall optical alignment of the receiver cold optics with the agreement between measured and predicted curves. The irregualar shape of the beam response pattern is expected due to the larger side-lobe response of the optical system without mirrors.
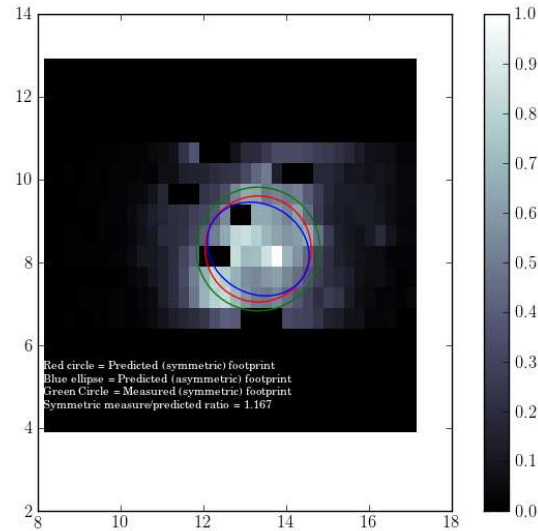
Figure 5.17: Receiver-only beam response pattern as measured by a single detector at the window. The red circle is the predicted FWHM contour, the green circle is the measured FHWM. The ratio of measured to predicted is 1.167.

5.3.2 Telescope Characterization

The second, full-scale tests were perform during July and August 2012 at the CSBF facility in Palestine, TX.

Measurement

The EBEX telescope was fully assembled and aligned prior to the testing and the experimental apparatus consisted of an enclosed millimeter-wave source mounted at the top of a nearby water tower on the premises of the facility, see Figure 5.18. The source was a Gunn oscillator from J. E. Carlstrom, Inc., with precise frequency tuning functionality between 127-150 GHz capable of outputting between 7 and 21 mW. Fixed and adjustable inline attenuators were used to provide appropriate output powers to avoid detector saturation. In order to provide signal in the 250 and 410 GHz bands, a frequency doubler and tripler were utilized at appropriate base frequency to generate
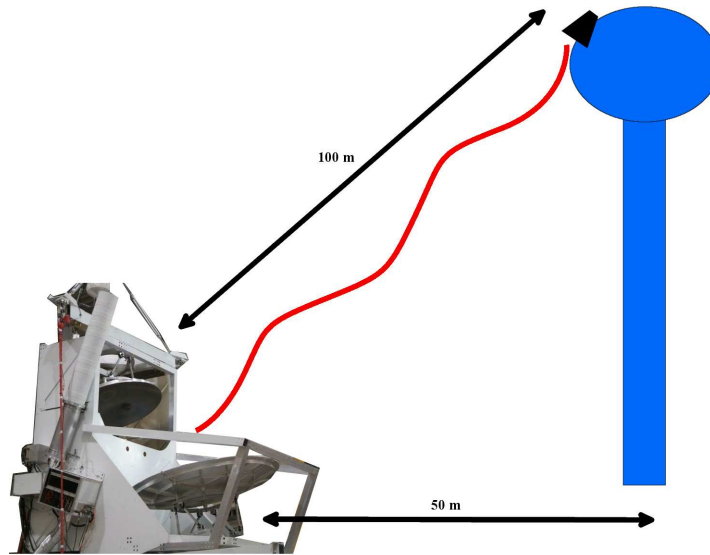
Figure 5.18: Full telescope beam response experimental setup.

signals within the respective band. The source was electrically chopped with a micro-controller board by toggling the input power to the Gunn diode. Measurements of the turn-on, turn-off, and ringing timescales for this modulation scheme were several factors smaller than the EBEX bolometer time constants.

The SMB was initially kept stationary for the first round of testing, and was rotated during latter testing when it was discovered that beam response could be measured at the same time as polarized beam response, which requires SMB rotation. The rotation of the SMB, in general, increased the noise level during the beam response testing about a factor of 2 and required careful placement of the chop frequency relative to SMB rotation speed.

The source and mounting were affixed to the top railing of the 50 m tall water tower visible outside from inside the testing facility. The source was directed at the nominal location of the telescope primary mirror by use of a handheld laser, and was situated approximately 100 m from the telescope during testing. The telescope pointing was controlled by the ACS with the pointing determined by measurements from a pair of redundant star camera of a temporary light structure, called the "lighthouse," mounted on either side of the source enclosure on the water tower. The star camera measurements

were supplimented by pointing reconstructed from integrated gyroscope measurements. This pointing measurement scheme achieved pointing accuracy within 1 arcminute over scales of 20 arcminutes, and within 1.5 arcminutes over scales of $1.2°$ in both azimuthal and elevation pointing.

The beam characterization measurements were carried out at night to avoid excess atmospheric loading of the detectors, day-time operations of the CSBF facility, and accidental cryogenic element damage from near-sun pointing events. In addition, the placement of a cellular transceivers at the top of the water tower required coordination with the cellular network provider for transceiver shutdown during scheduled testing periods.

The testing procedure for the full telescope measurements consisted of first putting the telescope in an operational state by tuning the detector arrays to the loading present from atmosphere by aiming the telescope at high elevation, about $60°$, which reduced the atmospheric loading on the detectors due to the thinner optical depth of atmosphere present at high elevation angles. The detectors were then electrically placed into the TES transition to increase response and held in the transition with the DfMUX biasing system, and then the telescope was aimed roughly at the source on the water tower. Next the source was adjusted to emit the correct output frequency for the band being tested and aligned with the nominal telescope position.

The telescope was then scanned in the azimuth and elevation directions to locate the nominal pointing for a single detector. Once the nominal telescope pointing for maximal signal on a given detector was found, the telescope then underwent raster scans centered on the detector with small scans consisting of coverage over a 30 arcmin by 30 arcmin area and larger scans covering several square degrees. The available scan area was limited to areas that the star cameras could determine pointing using the lighthouse due to quick pointing accuracy degradation outside that area due to the accumulation of pointing error from gyroscope rate integration. Periodic pointing establishment with the star cameras is required to achieve pointing accuracy appropriate for the beam response testing.

The smaller scan strategy was often repeated several times in quick succession for the same area to increase mapping coverage within the area and increase response accuracy for detectors within the coverage. The larger scan strategy was performed to map the

responses of several similar pointing detectors are the same time and possibly map the response of detectors bordering the edges of the star-camera limiting area.

The true azimuth and elevation pointing was reconstructed from the star camera and gyroscope pointing measurements, and recorded in the same time basis as the detector data for analysis purposes.

Analysis

The data analysis process differs from the previously mentioned pipelines due to the continuous nature of the mapping process compared to the stepped data taking procedure of the spectral response and PME measurements. The analysis was carried out with the IDL programming language.

The first step in the beam response analysis pipeline consists of reducing the input data, the individual bolometer measured response $b_i(t_{\mathrm{bolo}})$, the azimuth pointing $\phi(t_{\mathrm{ACS}})$, and the elevation pointing $\theta(t_{\mathrm{ACS}})$, where t_{bolo} and t_{ACS} designate the different timestreams with different sampling rates in the same timing basis, to the relevent data segment where the mapping was performed. This is reduced to a number of samples $N = 2^l 3^m$, where l, m are integers with $m \leq 3$ to decrease computation time.

The strength of the measured detector response at the source chop frequency as a function of time is determined by a series of frequency-domain filters applied to the FFT of the data. To isolate the response at the chop frequency, a band filter centered at the chop frequency is formed from a Butterworth filter of the form,

$$B_{f_c}(f) = \sqrt{\frac{1}{1 + \left(\frac{f - f_c}{\Delta f}\right)^{2n}}} \tag{5.28}$$

where f_c is the chop frequency, n is the order of the filter with $n = 15$ used, and Δf is the width of the filter with $\Delta f = 1.0$ Hz being generally used to enclose the total power in the chop frequency peak and scan sidebands and avoid potential leakage from SMB rotation frequencies, when applicable. The band filter response is shown in Figure 5.19. Since this filter is entirely real-valued, when applied to the FFT of the detector data we get $\tilde{b_i}'(f_{\mathrm{bolo}}) = B_{f_c}(f_{\mathrm{bolo}})\mathcal{F}(b_i(t_{\mathrm{bolo}}))$ with the original phase response of the detector data preserved.
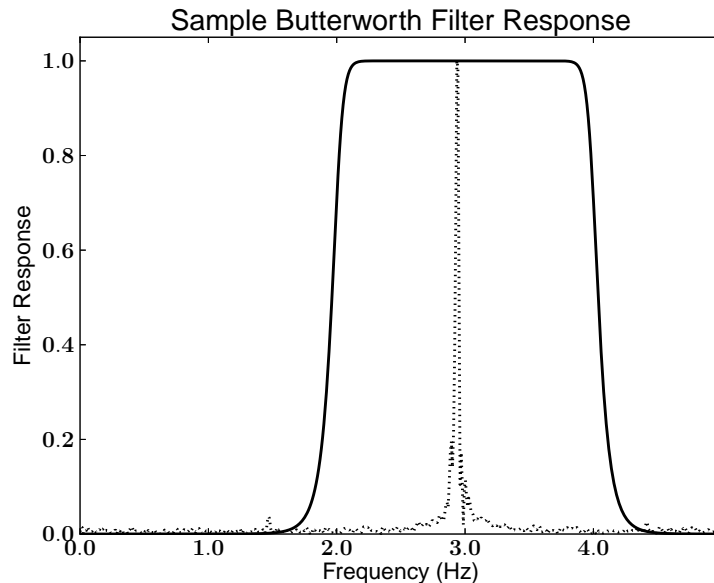
Figure 5.19: Sample Butterworth band filter response and sample detector PSD.

Then the positive-valued, time-domain band-filtered data, $|b_i'(t_{\text{bolo}})| = |\mathcal{F}^{-1}(\tilde{b}_i^{\,\prime}(f_{\text{bolo}}))|$, is found and then transformed back into fourier-space, $\tilde{b}_i^{\,\prime\prime}(f_{\text{bolo}}) = \mathcal{F}(|b_i'(t_{\text{bolo}})|)$. Then a low-pass frequency-domain filter is formed from $B_0(f_{\text{bolo}})$ with $f_c = 0$, also real-valued, and applied. The positive-valued inverse transform of this data,

$$b_i^*(t_{\text{bolo}}) = |\mathcal{F}^{-1}(B_0(f_{\text{bolo}})\tilde{b}_i^{\,\prime\prime}(f_{\text{bolo}}))| \qquad (5.29)$$

is the chop-frequency response as a function of t_{bolo}.

Due to the sampling rate of the detector data being about a factor of two faster than the sampling rate of pointing data, the azimuth and elevation pointing are interpolated to the detector sampling rate and this pointing, $\phi(t_{\text{bolo}})$ and $\theta(t_{\text{bolo}})$ then allows the the determination of chop-frequency response as a function of telescope pointing, $b_i^*(\phi(t_{\text{bolo}}), \theta(t_{\text{bolo}}))$.

At this point a correction was made for the curvilinear azimuth/elevation coordinate system, and azimuth was converted to co-elevation,

$$\phi'(\phi, \theta) = (\phi - \phi_c)\cos\theta + \phi_c \qquad (5.30)$$

where ϕ_c is the average azimuth position during the scan. Without this correction, the

beam response widths in azimuth would increase with elevation due to the convergence of lines of constant azimuth toward the poles.

The $b_i^*(\phi'(t_{\mathrm{bolo}}), \theta(t_{\mathrm{bolo}}))$ data set is then binned into a grid of coordinates (ϕ'_i, θ_j) with grid spacing $\Delta\phi', \Delta\theta = 1$ arcmin, covering the range of scan pointing. This data map of beam response, $M(\phi'_i, \theta_j)$ is then convolved with a symmetric 2-D Gaussian function with FWHM of 1 arcmin to smooth out expected pointing errors and then compared to predictions.

To quantify the beam response, the smoothed data map, $M_{\mathrm{smooth}}(\phi'_i, \theta_j)$, is least-$\chi^2$ fit to the general 2-D offset tilted Gaussian,

$$x' = (\phi' - \phi'_o)\cos\psi + (\theta - \theta_o)\sin\psi \tag{5.31a}$$

$$y' = -(\phi' - \phi'_o)\sin\psi + (\theta - \theta_o)\cos\psi \tag{5.31b}$$

$$G(\phi', \theta) = Ae^{-\frac{1}{2}\left[\left(\frac{x'}{\Delta x'}\right)^2 + \left(\frac{y'}{\Delta y'}\right)^2\right]} + B \tag{5.31c}$$

where A is the response amplitude, B is the baseline noise level, (ϕ'_o, θ_o) are the beam center coordinates, $\Delta x'$ and $\Delta y'$ are the semi-major and semi-minor widths, and ψ is the tilt angle of the semi-major axis relative to (ϕ', θ)-coordinates. The measured noise level is determined from the near chop-frequency PSD level and with the fit parameters and data map is used to calculate the χ^2_{red} goodness of fit.

A known systematic offset between the two timing systems, t_{bolo} and t_{ACS}, exists due to a delay between signal incidence on the detectors and data recording stemming from finite impulse response (FIR) signal processing filters inherent to the readout system. In order to measure and compensate for this, a variable delay is introduced between t_{bolo} and t_{ACS} prior to interpolating $\phi'(t_{\mathrm{ACS}}), \theta(t_{\mathrm{ACS}}) \rightarrow \phi'(t_{\mathrm{bolo}}), \theta(t_{\mathrm{bolo}})$, and the χ^2_{red} is calculated for each delay. The minimum χ^2_{red} delay is used for further processing and is recorded for each detector map.

Results

The χ^2_{red} distribution in each frequency band shows very large spread, with a large fraction of 250 and 410 GHz maps showing $\chi^2_{\mathrm{red}} > 50$ with a correlation between χ^2_{red} and beam widths. To explore this behavior, two beam maps from detector b75w1c10 during different scans on July 23, 2012, and July 25, 2012, are compared, Figure 5.20.
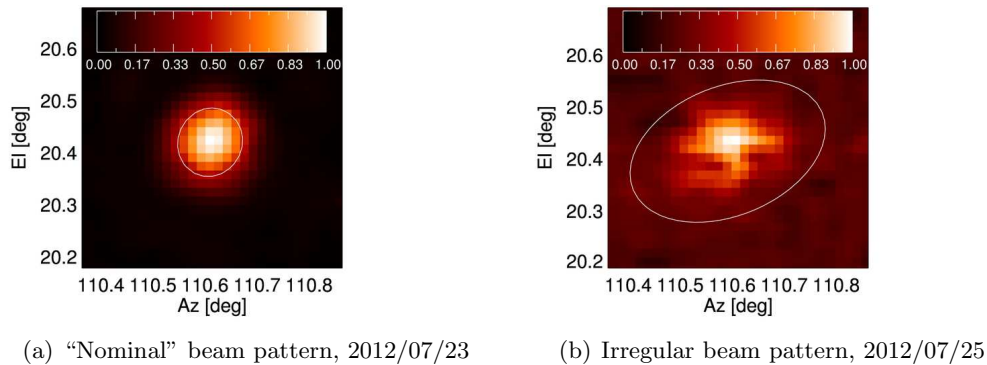
(a) "Nominal" beam pattern, 2012/07/23   (b) Irregular beam pattern, 2012/07/25

Figure 5.20: Single detector normalized beam response patterns on different days with 2-D Gaussian fit FWHM contour displayed.

These maps show a "nominal" Gaussian beam and larger irregular beam with a large discrepancy between noise levels, beam widths, and overall shape of the measured beams that cannot be attributed to changes in the optical system or source configuration. Several other detectors exhibit the same behavior across the three frequency bands.

A potential model for this behavior originates in the design of the detectors and the readout system. Due to the operation of the TES devices on the transition edge between an Ohmic device and superconductor, large fluctuations in incident power on the bolometer could shift the device into a less sensitive regime. A large drop in incident power could lower the TES temperature below T_c and it would exhibit no resistive response to signal, while an increase in incident power could raise the temperature into the Ohmic region where resistive sensitivity to temperature is greatly reduced and noise is increased.

With the TESs tuned to 85% of the normal resistance while looking at a low-emittance portion of the sky, the applied P_{elec} is relatively large and a large increase in P_{light} from lowering the telescope elevation to high-emittance sky combined with the source could saturate the detector, especially near the central portion of the beam with the highest signal. This reduction in sensitivity near the beam center would, in effect, flatten and widen the beam response while increasing the response noise in the central region. This could lead to large measured beam sizes with irregular shapes, as is observed. This effect would be scan-dependent as the detectors were re-tuned every evening prior to data taking and could manifest on otherwise nominal detectors.

Band (GHz)	Number	Large FWHM	Small FWHM	Eccentricity
150	20	8.32±0.40	7.57±0.28	0.40±0.09
250	6	8.29±0.76	6.69±0.55	0.59±0.04
410	10	8.04±0.97	6.78±0.83	0.52±0.10

Table 5.6: "Good" detector beam response statistics for large and small FWHM fits, in arcmin, and eccentricities.

Using atmospheric emission models for the conditions of the night sky in Palestine, TX during appropriate times, the change in atmospheric loading on the detectors can be predicted. These calculation show that between a $60°$ telescope elevation and $20°$, where the beam response measurements happened, the 150 GHz detectors would see a 30% increase in atmospheric loading from 0.95 pW to 1.22 pW, and 250 GHz detectors would see a 8% increase from 2.18 pW to 2.26 pW. The 410 GHz detectors would see 1.98 pW of atmospheric loading with no change in elevation. This combined with a potentially under-attenuated source could result in saturated detectors that produce large irregular beams.

Given this effects, it was determined that the characterization of the optics would be determined by the most Gaussian beam maps in each frequency band. Choosing several representative "good" beam maps gives beam widths and statistics shown in Table 5.6. This data indicates varying levels of eccentricity in the beams, but strong agreement with the predicted 8 arcmin FWHM for the optical system.

Chapter 6

Long Duration Flight

EBEX was launched from Long Duraction Balloon Facility at McMurdo Station in Antarctica at 00:30 GMT December 29, 2012. The payload achieved an altitude of approximately 36 km about 5 hours laters. The payload was science operational until 06:00 GMT January 9, 2013, for a duration of 10.83 days and the flight was terminated on 11:30 GMT January 23, 2013, for a total flight time of 25.49 days.
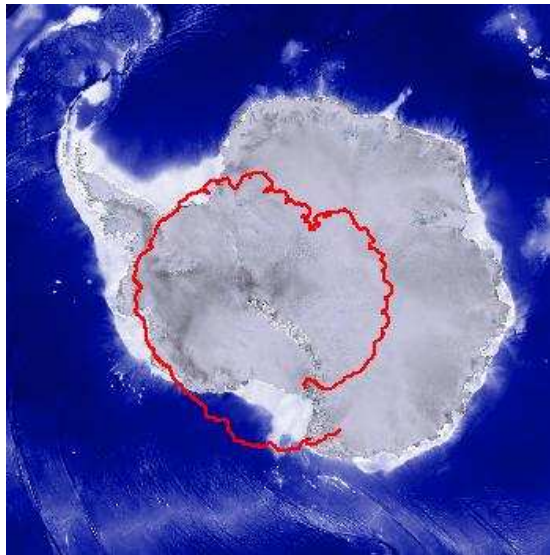

Figure 6.1: Track of the EBEX payload during the LDB flight.

The trajectory of the EBEX payload is shown in Figure 6.1. During flight, the motor
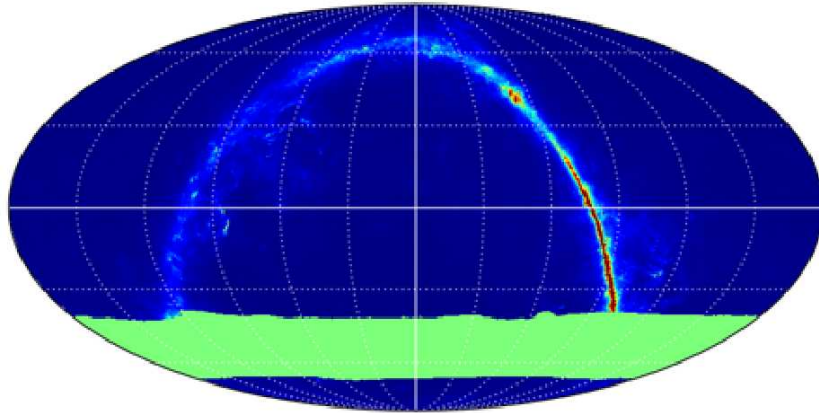
Figure 6.2: Scan area of the EBEX payload during the LDB flight (green area).

controller for the pivot motor controlling the azimuthal pointing of the payload was subject to overheating and thus azimuthal pointing was determined by the rotation of the payload on the tether line to the balloon. This changed and increased the observation area, shown in Figure 6.2.

6.1 LHe Loading

With more specific knowledge of the operations of the receiver during flight, a more accurate model of the LHe loading can be ascertained and checked with the measured value.

The approximation of using 300 K as the outer shell temperature of the receiver was reasonable as the shell varied in temperature between 283 and 313 K, see Figure 6.3. The 300K shell temperature shows a strong correlation with sun elevation, with a lag between maximum sun elevation and maximum shell temperature caused by the time constant of the warming thermal mass. The drift in 300K shell temperature to higher temperatures also is inversely correlated with peak-to-peak sun elevation, with the shell temperature rising with increasing minimum sun angle. This can be explained by the shell being unable to cool due to the higher sun minimum elevation angle.

These 300K shell temperatures are higher than expected and than ground operation temperatures due to regular solar radiation incident on the inner frame and receiver
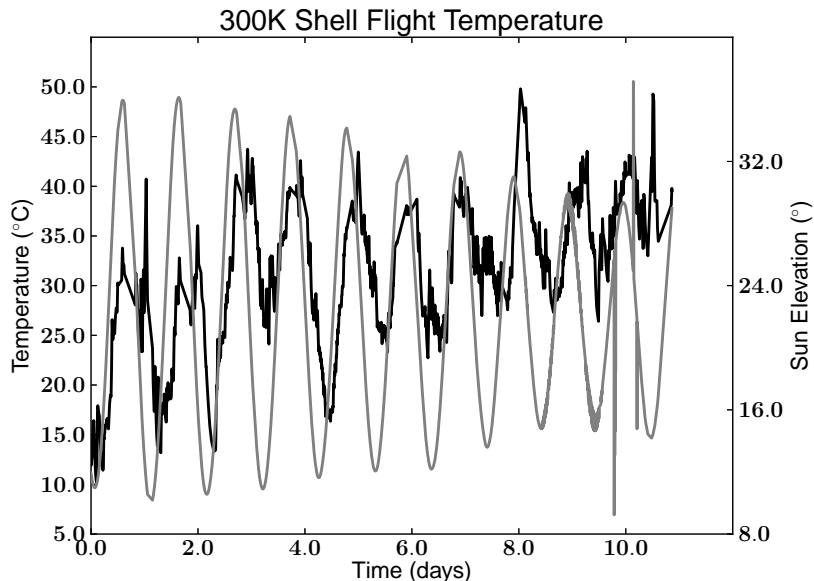
Figure 6.3: Temperature profile of receiver 300K shell (black) and sun elevation (gray) during LDB flight.

outer shell without atmospheric convection to cool.

Another factor in the load calculation is whether the increase in 300K shell temperature affects the Teflon temperature, and thus the loading on the LHe bath. Figure 6.4 shows the temperature of the top of the LN shell during flight and indicates an increase in temperature of roughly 10 K over the flight. This is consistent with the measured temperature drift of roughly 1 K per day that occurs in the LN shell top from the lowering LN bath level as the cryogens evaporate. This change in LN shell top temperature is already factored in the loading calculation from Teflon temperature mentioned in Section 4.1.

A post hoc prediction of the holdtime is modified by two flight specific details. The first modification is that the EBEX payload is on the ground prior to launch and after the last cryogenic fill with the thick window in the optical path for some time even after launch until the atmospheric pressure is reduced sufficiently to operate the DWM and move the thick window from the optical path. Between the last cryogen fill and the opening of the DWM, a period of 1190 minutes or 0.826 days, the receiver was exposed
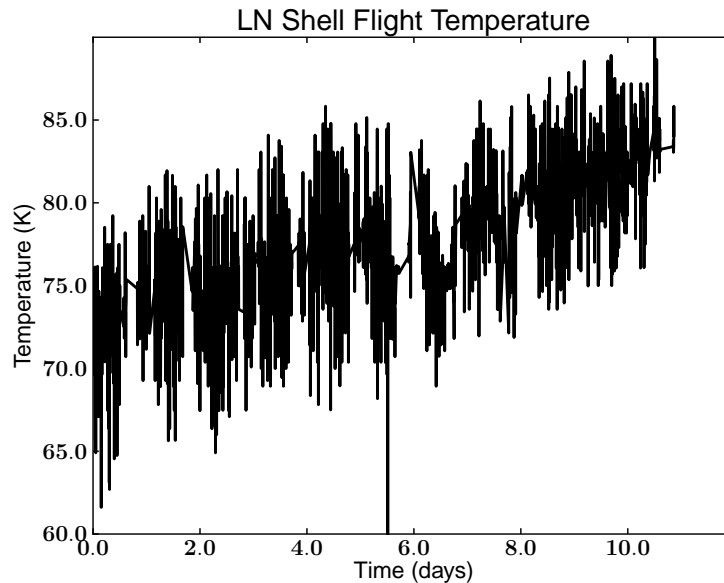
Figure 6.4: Temperature profile of the top of the LN shell during LDB flight. Temperatures below 77K stem from diode-specific voltage offsets on the temperature sensor.

to the emission from the thick window and warm atmospheric environment. Using the filter transmission data from 4.2, this would put a load of 1094 mW on the Teflon filter for this duration, which using Equation 4.2, would predict a light load of 137 mW on the LHe stage. This is an excess light load of 23 mW for the 0.826 days, or 19 mW·days in which the receiver experiences a ground-like light load. This modifies Equation 4.3 to be,

$$H = \frac{V + 2.0 \text{ days } F - 19 \text{ mW} \cdot \text{days}}{L + F} - 1 \text{ day} = 10.62 \text{ days} \qquad (6.1)$$

Finally, the last correction to the holdtime prediction stems from the duty cycle of the SMB operation. The SMB was rotated during approximately 51% of the flight time, rather than continuously, to maximize fridge holdtime, as discussed in 4.1.3, and perform other tests without AHWP rotation. This gives a modified LHe load without fridge cycling, $L_{mod} = 235$ mW. This predicts, from Equation 6.1, a LHe holdtime of $H_{\text{predicted}} = 10.860$ days. This agrees remarkably well with the observed LHe holdtime of $H_{\text{observed}} = 10.833$ days during the LDB flight.
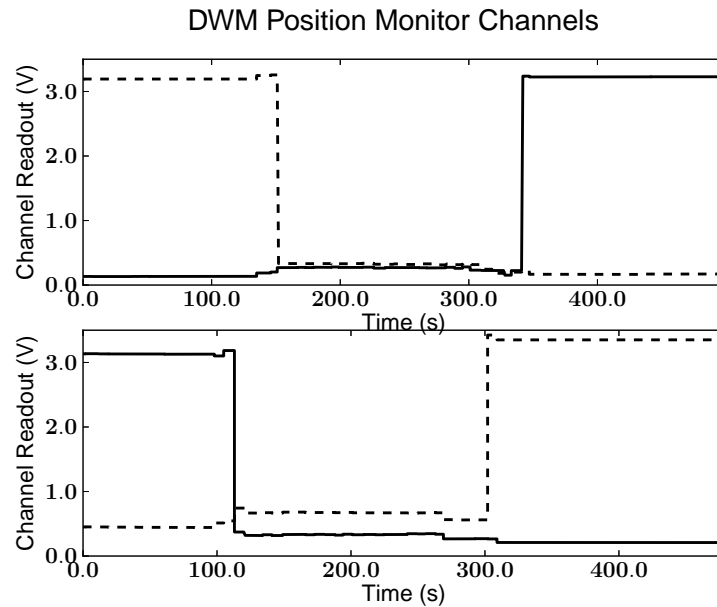
Figure 6.5: DWM position encoders during opening (upper), and closing (lower). The closed indicator (dashed) and open indicator (solid) are shown, with high voltage showing the state as active.

6.2 DWM Operation

The DWM operated twice during the LDB flight, the first time approximately three hours after launch, and the second time approximately two hours after LHe exhaustion. The position encoder channels during these times are shown in Figure 6.5. These monitors indicate successful operation for opening and closing during the LDB flight. The LHe loading calculated during flight also indicates no excess loading from vacuum leakage of the DWM. However, due to a failure of receiver vacuum hardware, presumably during payload landing, the vacuum integrity of the DWM after closing could not be determined from the recovered payload.

With nominal LHe loading performance, DWM execution, successful SMB rotation, nominal instrument temperature profiles, and successful large-array detector operation, the general operation of the EBEX receiver during LDB flight is considered a success.

References

[1] P. A. R. Ade, R. W. Aikin, D. Barkats, S. J. Benton, C. A. Bischoff, J. J. Bock, J. A. Brevik, I. Buder, E. Bullock, C. D. Dowell, L. Duband, J. P. Filippini, S. Fliescher, S. R. Golwala, M. Halpern, M. Hasselfield, S. R. Hildebrandt, G. C. Hilton, V. V. Hristov, K. D. Irwin, K. S. Karkare, J. P. Kaufman, B. G. Keating, S. A. Kernasovskiy, J. M. Kovac, C. L. Kuo, E. M. Leitch, M. Lueker, P. Mason, C. B. Netterfield, H. T. Nguyen, R. O'Brient, R. W. Ogburn, A. Orlando, C. Pryke, C. D. Reintsema, S. Richter, R. Schwarz, C. D. Sheehy, Z. K. Staniszewski, R. V. Sudiwala, G. P. Teply, J. E. Tolan, A. D. Turner, A. G. Vieregg, C. L. Wong, K. W. Yoon, and Bicep2 Collaboration. Detection of B-Mode Polarization at Degree Angular Scales by BICEP2. *Physical Review Letters*, 112(24):241101, June 2014.

[2] C. Bao, B. Gold, C. Baccigalupi, J. Didier, S. Hanany, A. Jaffe, B. R. Johnson, S. Leach, T. Matsumura, A. Miller, and D. O'Dea. The Impact of the Spectral Response of an Achromatic Half-wave Plate on the Measurement of the Cosmic Microwave Background Polarization. ApJ, 747:97, March 2012.

[3] D.J Benford, T.J Powers, and S.H Moseley. Thermal conductivity of kapton tape. *Cryogenics*, 39(1):93 – 95, 1999.

[4] C. L. Bennett, M. Bay, M. Halpern, G. Hinshaw, C. Jackson, N. Jarosik, A. Kogut, M. Limon, S. S. Meyer, L. Page, D. N. Spergel, G. S. Tucker, D. T. Wilkinson, E. Wollack, and E. L. Wright. The Microwave Anisotropy Probe Mission. ApJ, 583:1–23, January 2003.

[5] EBEX Collaboration. NASA 2012 proposal for the EBEX experiment. NASA Proposal, 2012.

[6] DuPont. Properties of DuPont VESPEL Parts. 1993.

[7] Dupont. Kapton Summary of Properties. 2014.

[8] Dupont. Nomex Brand by Dupont. 2014.

[9] Ellsworth Adhesives. Emerson & Cuming STYCAST 2850 FT. 2014.

[10] Emerson & Cuming Microwave Products. Eccosorb HR. 2014.

[11] Emerson & Cuming Microwave Products. Eccosorb MF. 2014.

[12] W. G. Fastie. A small plane grating monochromator. *Journal of the Optical Society of America (1917-1983)*, 42:641, September 1952.

[13] W. G. Fastie. Image forming properties of the Ebert monochromator. *Journal of the Optical Society of America (1917-1983)*, 42:647, September 1952.

[14] D. J. Fixsen, E. S. Cheng, J. M. Gales, J. C. Mather, R. A. Shafer, and E. L. Wright. The Cosmic Microwave Background Spectrum from the Full COBE FIRAS Data Set. ApJ, 473:576–587, December 1996.

[15] A. Gladun, C. Gladun, M. Knorn, and H. Vinzelberg. Investigation of the heat conductivity of niobium in the temperature range 0.0523 k. *Journal of Low Temperature Physics*, 27(5-6):873–886, 1977.

[16] B. Gold, N. Odegard, J. L. Weiland, R. S. Hill, A. Kogut, C. L. Bennett, G. Hinshaw, X. Chen, J. Dunkley, M. Halpern, N. Jarosik, E. Komatsu, D. Larson, M. Limon, S. S. Meyer, M. R. Nolta, L. Page, K. M. Smith, D. N. Spergel, G. S. Tucker, E. Wollack, and E. L. Wright. Seven-year Wilkinson Microwave Anisotropy Probe (WMAP) Observations: Galactic Foreground Emission. ApJS, 192:15, February 2011.

[17] D. Hanson, S. Hoover, A. Crites, P. A. R. Ade, K. A. Aird, J. E. Austermann, J. A. Beall, A. N. Bender, B. A. Benson, L. E. Bleem, J. J. Bock, J. E. Carlstrom,

C. L. Chang, H. C. Chiang, H.-M. Cho, A. Conley, T. M. Crawford, T. de Haan, M. A. Dobbs, W. Everett, J. Gallicchio, J. Gao, E. M. George, N. W. Halverson, N. Harrington, J. W. Henning, G. C. Hilton, G. P. Holder, W. L. Holzapfel, J. D. Hrubes, N. Huang, J. Hubmayr, K. D. Irwin, R. Keisler, L. Knox, A. T. Lee, E. Leitch, D. Li, C. Liang, D. Luong-Van, G. Marsden, J. J. McMahon, J. Mehl, S. S. Meyer, L. Mocanu, T. E. Montroy, T. Natoli, J. P. Nibarger, V. Novosad, S. Padin, C. Pryke, C. L. Reichardt, J. E. Ruhl, B. R. Saliwanchik, J. T. Sayre, K. K. Schaffer, B. Schulz, G. Smecher, A. A. Stark, K. T. Story, C. Tucker, K. Vanderlinde, J. D. Vieira, M. P. Viero, G. Wang, V. Yefremenko, O. Zahn, and M. Zemcov. Detection of B-Mode Polarization in the Cosmic Microwave Background with Data from the South Pole Telescope. *Physical Review Letters*, 111(14):141301, October 2013.

[18] J. R. Hinderks, P. Ade, J. Bock, M. Bowden, M. L. Brown, G. Cahill, J. E. Carlstrom, P. G. Castro, S. Church, T. Culverhouse, R. Friedman, K. Ganga, W. K. Gear, S. Gupta, J. Harris, V. Haynes, B. G. Keating, J. Kovac, E. Kirby, A. E. Lange, E. Leitch, O. E. Mallie, S. Melhuish, Y. Memari, A. Murphy, A. Orlando, R. Schwarz, C. O' Sullivan, L. Piccirillo, C. Pryke, N. Rajguru, B. Rusholme, A. N. Taylor, K. L. Thompson, C. Tucker, A. H. Turner, E. Y. S. Wu, and M. Zemcov. Quad: A high-resolution cosmic microwave background polarimeter. *The Astrophysical Journal*, 692(2):1221, 2009.

[19] J. Hubmayr. *Bolometric detectors for EBEX: a balloon-borne cosmic microwave background polarimeter*. PhD thesis, University of Minnesota/Twin Cities, 2009.

[20] B. R. Johnson. *MAXIPOL: a bolometric, balloon-borne experiment for measuring the polarization anisotropy of the cosmic microwave background radiation*. PhD thesis, University of Minnesota/Twin Cities, 2004.

[21] B. R. Johnson, M. E. Abroe, P. Ade, J. Bock, J. Borrill, J. S. Collins, P. Ferreira, S. Hanany, A. H. Jaffe, T. Jones, A. T. Lee, L. Levinson, T. Matsumura, B. Rabii, T. Renbarger, P. L. Richards, G. F. Smoot, R. Stompor, H. T. Tran, and C. D. Winant. MAXIPOL: a balloon-borne experiment for measuring the

polarization anisotropy of the cosmic microwave background radiation. *New Astronomy Review*, 47:1067–1075, December 2003. astro-ph/0308259.

[22] A.P. King. The radiation characteristics of conical horn antennas. *Proceedings of the IRE*, 38(3):249–251, March 1950.

[23] J. Klein. *Design, Implementation, and Calibration of Half-Wave Plate Polarimetry for the E and B Experiment (EBEX)*. PhD thesis, University of Minnesota/Twin Cities, 2014.

[24] L. Knox and Y. Song. A limit on the detectability of the energy scale of inflation. Phys. Rev. Lett., 89:011303 (4 pages), 2002. astro-ph/0202286.

[25] Lake Shore Cryotronics, Inc. Cryogenic wire specifications. 2014.

[26] J. W. Lamb. Miscellaneous data on materials for millimetre and submillimetre optics. *Int. J. IR and Millimeter Waves*, 17:1997–2034, 1996.

[27] E. G. Loewen, M. Nevière, and D. Maystre. Grating efficiency theory as it applies to blazed and holographic gratings. *Appl. Opt.*, 16(10):2711–2721, Oct 1977.

[28] J. C. Mather, E. S. Cheng, R. E. Eplee, Jr., R. B. Isaacman, S. S. Meyer, R. A. Shafer, R. Weiss, E. L. Wright, C. L. Bennett, N. W. Boggess, E. Dwek, S. Gulkis, M. G. Hauser, M. Janssen, T. Kelsall, P. M. Lubin, S. H. Moseley, Jr., T. L. Murdock, R. F. Silverberg, G. F. Smoot, and D. T. Wilkinson. A preliminary measurement of the cosmic microwave background spectrum by the Cosmic Background Explorer (COBE) satellite. ApJ, 354:L37–L40, May 1990.

[29] T. Matsumura. *A Cosmic Microwave Background Radiation Polarimeter Using Superconducting Magnetic Bearings*. PhD thesis, University of Minnesota/Twin Cities, 2006.

[30] M. B. Milligan. *The E and B EXperiment: Implementation and Analysis of the 2009 Engineering Flight*. PhD thesis, University of Minnesota/Twin Cities, 2011.

[31] J.R. Olson. Thermal conductivity of some common cryostat materials between 0.05 and 2 k. *Cryogenics*, 33(7):729 – 731, 1993.

[32] Parker. Parker O-Ring Handbook. 2007.

[33] A. A. Penzias and R. W. Wilson. A Measurement of Excess Antenna Temperature at 4080 Mc/s. ApJ, 142:419–421, July 1965.

[34] J. B. Peterson and P. L. Richards. A cryogenic blackbody for millimeter wavelengths. *International Journal of Infrared and Millimeter Waves*, 5:1507–1515, December 1984.

[35] Planck Collaboration, P. A. R. Ade, N. Aghanim, C. Armitage-Caplan, M. Arnaud, M. Ashdown, F. Atrio-Barandela, J. Aumont, C. Baccigalupi, A. J. Banday, and et al. Planck 2013 results. XVI. Cosmological parameters. *ArXiv e-prints*, March 2013.

[36] D. E. Polsgrove. *Calibration of the E and B EXperiment (EBEX), A Balloon-Borne Cosmic Microwave Background Polarimeter*. PhD thesis, University of Minnesota/Twin Cities, 2009.

[37] M. .B Priestley. *Spectral Analysis and Time Series*. Academic Press, 1983.

[38] B. Rabii, C. D. Winant, M. E. Abroe, P. Ade, A. Balbi, J. J. Bock, J. Borrill, A. Boscaleri, P. de Bernardis, J. S. Collins, P. G. Ferreira, S. Hanany, V. V. Hristov, A. H. Jaffe, B. R. Johnson, A. E. Lange, A. T. Lee, C. B. Netterfield, E. Pascale, P. L. Richards, G. F. Smoot, R. Stompor, and J. H. P. Wu. MAXIMA: A Balloon-Borne Cosmic Microwave Background Anisotropy Experiment. *ArXiv Astrophysics e-prints*, September 2003. astro-ph/0309414.

[39] R. Radebaugh. NIST Cryogenics Technologies Group. `http://www.cryogenics.nist.gov/index.htm`.

[40] M. C. Runyan and W. C. Jones. Thermal conductivity of thermally-isolating polymeric and composite structural support materials between 0.3 and 4 K. *Cryogenics*, 48:448–454, September 2008.

[41] I. S. Sagiv. *The EBEX Cryostat and Supporting Electronics*. PhD thesis, University of Minnesota/Twin Cities, 2011.

[42] C. Tokoku, N. Kimura, S. Koike, T. Kume, Y. Sakakibara, T. Suzuki, K. Yamamoto, D. Chen, S. Goto, M. Tanaka, S. Ioka, K. Nakamoto, H. Nezuka, T. Uchiyama, M. Ohashi, and K. Kuroda. Cryogenic system for the interferometric cryogenic gravitationalwave telescope, kagra - design, fabrication, and performance test -. *AIP Conference Proceedings*, 1573(1):1254–1261, 2014.

[43] Adam L. Woodcraft. Recommended values for the thermal conductivity of aluminium of different purities in the cryogenic to room temperature range, and a comparison with copper. *Cryogenics*, 45(9):626 – 636, 2005.

Chapter 7

Glossary and Acronyms

Care has been taken in this thesis to minimize the use of jargon and acronyms, but this cannot always be achieved. This appendix contains a table of acronyms and their meaning.

7.1   Acronyms

Table 7.1: Acronyms

Acronym	Meaning
EBEX	E and B EXperiment
CMB	Cosmic microwave background
ACS	Attitude control system
HWP	Half-wave plate
AHWP	Achromatic half-wave plate
VCS2	Vapor-cooled shield 2
	Continued on next page

Table 7.1 – continued from previous page

Acronym	Meaning
LN	Liquid nitrogen
VCS1	Vapor-cooled shield 1
LHe	Liquid helium
UHMWPE	Ultra-high molecular weight polyethylene
DWM	Double window mechanism
RF	Radio-frequency
LPE	Low-pass edge
NDF	Neutral density filter
PME	Polarization modulation efficiency
SMB	Superconducting magnetic bearing
OFHC	Oxygen-free high conductivity
TES	Transistion edge sensor
DfMUX	Digital frequency-domain multiplexing
SQUID	Superconducting quantum interference device
SiD	Silicon diode
PPW	Parallel-plate waveguide
FCP	Flight control program
FWHM	Full width, half maximum

Table 7.1 – continued from previous page

Acronym	Meaning
CMM	Coordinate-measuring machine
EF	Ebert-Fastie
IVA	Intensity versus angle